Structure and reactions of GRNa,SO4 and the occurence of GR in nature

Christiansen, Bo C.

Publication date:
2008

Document version
Publisher's PDF, also known as Version of record

FACULTY OF SCIENCE
UNIVERSITY OF COPENHAGEN

PhD thesis

Bo C. Christiansen

Structure and reactions of $GR_{Na,SO4}$ and the occurrence of GR in nature

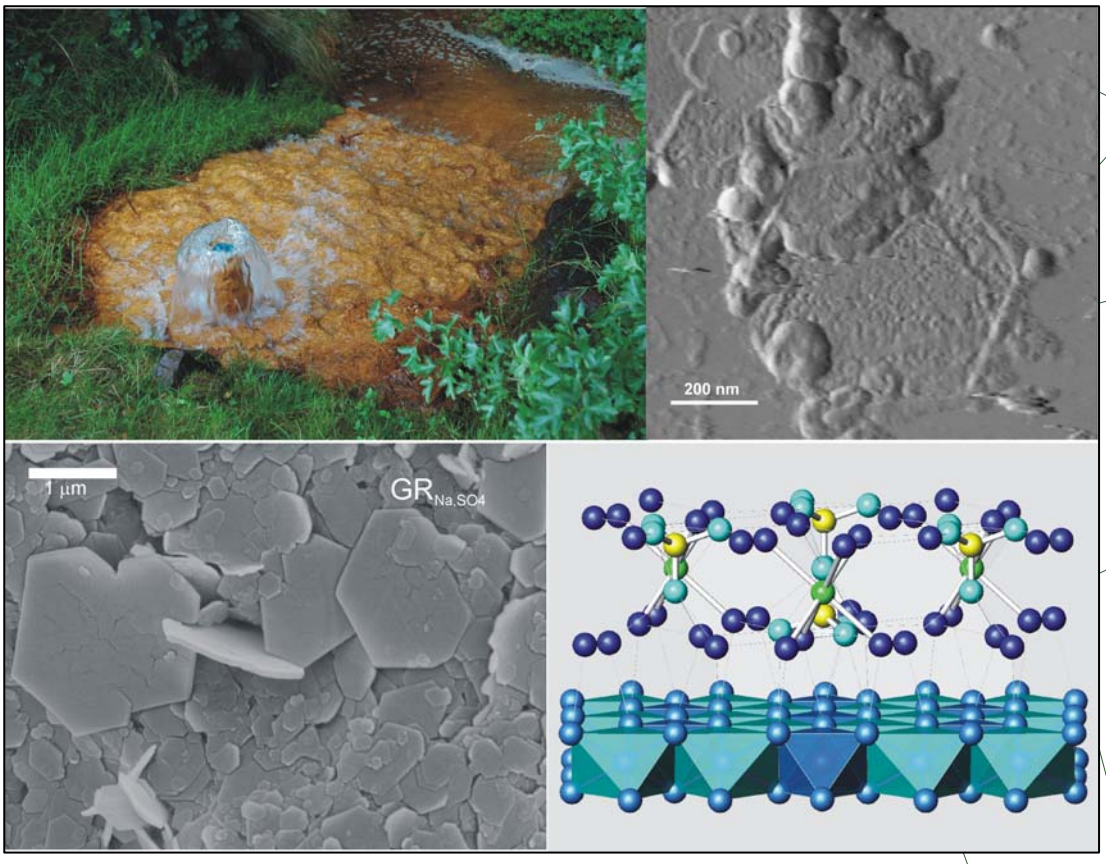

Academic advisor: Susan L. S. Stipp

Submitted: 28/07/08

Index

Dansk Resumé

Formålet med denne ph.d.-afhandling er at beskrive processer, der foregår, hvor jernholdige mineraler er til stede. Arbejdet fokuserede specielt på ferro-ferri hydroxyd-holdige mineraler, grøn rust, og disses mulige rolle i jerns kredsløb. Det første studium havde som formål at beskrive jernholdige mineraler i sprækker i granit ved Äspö, Sverige. Jernoxidernes struktur, kemiske sammensætning og stabile jern-isotopforhold tillod rekonstruktion af de palæo-redoxmæssige-forhold i granittens sprækker. Der blev fundet 3 typer ferri- oxider dannet i forskellige miljøer: 1) grovkornede hydrothermale hematitter, 2) meget finkornede amorfe jernoxider, der var udfældet under boring af kernen, 3) krystalline jernoxider af intermediær størrelse, der blev dannet ved lave temperaturer (<10°C) i en dybde på mindre end ~100 m under overfladen.

Når pH er neutral til let basisk vil oxidation af Fe(II)-holdige opløsninger udfælde grøn rust. I det andet studium benyttede jeg Røntgendiffraktion til, at identificere grøn rust i grundvandsområder med middel til relativt høj jernkoncentration. Metoden, jeg udviklede, er enkel og bygger på, at grøn rust stabiliseres, når det sidder på overflader af f.eks. glas eller glimmermineraler. Prøvetagningen skete i nærheden af Bornholms Lufthavn og i tunnelen til Äspö Hard Rock Laboratorium. Prøverne transporteredes under nitrogen til vores laboratorium, hvor Røntgendiffraktion viste, at prøvematerialet således indeholdt GR_{CO3}. Tilstedeværelsen af GR blev ligeledes bekræftet af et drastisk fald i toppenes intensitet efter et par dages kontakt med den almindelige atmosfære.

Viden om den kemiske sammensætning af mineraler og deres krystalstruktur er essentiel, idet de bestemmer det faste stofs opførsel. En litteraturgennemgang i forbindelse med det tredje studium viste, at tidligere undersøgelser af sulfat-holdige GR typer benyttede strukturelle og sammensætningsmæssige parametre, der var fejlagtige eller mangelfulde. Jeg udførte grundige analyser af sulfat-holdig grøn rust med Røntgendiffraktion, Rietveld-analyse, og Mössbauer-spektroskopi. Sammenholdt med den kemiske sammensætning tillod det mig, at reevaluere strukturen og sammensætningen af stoffet. De nye resultater beviste, at natrium er en essentiel strukturel komponent af sulfat-holdig grøn rust, $GR_{Na,SO4}$. Den kemiske formel for $GR_{Na,SO4}$ er således $NaFe(II)_6Fe(III)_3(SO_4)_2(OH)_{18}\bullet 12H_2O$, dens rum gruppe er P-3, og enhedscelle parametrene er a = 9.528(6) Å, c = 10.968(8) Å og Z = 1.

Den sidste del af denne afhandling beskriver, hvordan $GR_{Na,SO4}$ reagerer med andre redox-sensitive elementer. Selenium og neptunium er typiske henfaldsprodukter fra brugte radioaktive brændselsstænger. Disse og andre radioaktive elementer vil udgøre et alvorligt miljømæssigt problem, hvis der skulle opstå lækage fra fremtidige depoter til radioaktivt affald. For bedre at forstå de radioaktive elementers opførsel i naturen og deres vekselvirkning med depotets jernstrukturer undersøgte jeg, hvordan selenit (SeO_3^{2-}) og neptunyl (NpO_2^{+}) reagerede med $GR_{Na,SO4}$. Selenit reduceredes hurtigt af GR ved at reagere langs kanten af GR partiklerne. Her dannedes trigonalt elementært Se(0), mens den grønne rust omdannedes til goethit. Ved reaktion mellem neptunyl og GR foregik reduktion ligeledes omkring kanterne af den grønne rust. Neptunium reduceredes til tetravalent Np, mens GR omdannedes til goethit. Ved efterfølgende oxidation af reaktionsblandingen i luft forblev omkring 40% af neptunium i dets tetravalente form. Resultaterne indikerer, at Np(IV) enten er inkorporeret i goethitstrukturen eller eksisterer som en selvstændig oxid fase. Det skal dog noteres, at tilstedeværelsen af Np(IV) oxider er mindre sandsynligt, da denne fase let oxideres til pentavalent Np.

I denne afhandling har jeg vist, at jernholdige mineraler kan bruges som indikatorer for redox-forhold, og at sulfat-holdig grøn rust indeholder monovalente kationer i mellemlaget, i dette tilfælde natrium. Grøn rust er således ikke udelukkende anion-substituerende mineraler, men kan ligeledes potentielt udveksle kationer med omkringliggende væsker, som det ses for ler-mineraler. I grundvand-transportmodeller er det nødvendigt at inkludere de parametre, der beskriver grøn rusts opførelse under grundvands-forhold, da faserne gerne reagerer med en række giftige stoffer, hvorved de immobiliseres. Ud fra min forskning er det nu endnu tydeligere, at modeller, der skal simulere eller forudsige grundvandstransport af giftige elementer, skal inkludere de termodynamiske og kinetiske parametre for grøn rust og dets reaktivitet med opløste stoffer.

English Summary

The purpose of this PhD thesis is to describe the processes that take place where iron-containing minerals are present. The work was especially focused on the ferro-ferric hydroxide minerals, the green rust series, and their possible role in the geochemical iron-cycle. The goal of the first study was to describe the iron-containing minerals in the granitic fractures at Äspö, Sweden. The structure, chemical composition and stable iron isotope ratio of the ferric oxides allowed reconstruction of the paleo-redox conditions in the granitic fractures. I found 3 types of formation environments: 1) course-grained hydrothermal hematites, 2) very fine-grained amorphous iron-oxides that had precipitated during drilling and 3) crystalline iron-oxides of intermediate size which we interpreted to form at low temperatures (< 10° C) at a depth of less than ~100 m below surface.

When pH is neutral to slightly basic Fe(II)-containing solutions oxidise, green rust precipitates. In the second study, X-ray diffraction allowed identification of green rust in groundwater from areas with medium to relatively high iron concentration. The method I developed is relatively simple and is based on the observation that green rust is stabilised, when it attaches to substrates such as glass and mica. The sampling was done from the site close to the airport of Bornholm and in the Äspö hard rock laboratory tunnel. The samples were transported to the laboratory under nitrogen where the X-ray diffraction showed that the material contained GR_{CO3}. The presence of green rust was verified by a drastic decrease in the intensity of the GR peaks when the samples had been exposed to air for a couple of days.

Knowledge about the chemical composition of minerals and their crystal structures is essential for use in databases and, because composition determines the behaviour of a solid. A literature review showed that previous reports of sulphate-containing green rust have presented structural and compositional parameters that have been erroneous or lacking. The third study was a detailed examination of sulphate-containing green rust by X-ray diffraction, Rietveld analysis and Mössbauer spectroscopy. Using newly determined data for chemical composition from pure samples, we were able to determine details in the structure and composition of the solid. The new results proved that sodium is essential for sulphate-containing green rust, $GR_{Na,SO4}$. The chemical composition is $NaFe(II)_6Fe(III)_3(SO_4)_2(OH)_{18}\bullet 12H_2O$, its space group is P-3, and its cell parameters are: a = 9.528(6) Å, c = 10.968(8) Å and Z = 1.

The last chapter describes how $GR_{Na,SO4}$ reacts with other redox-sensitive elements. Selenium and neptunium are typical daughter products of spent radioactive fuel rods. These and other radioactive elements pose a serious environmental risk for long term storage, if leaks develop in the waste repository. To better understand the behaviour of these radioactive elements in the natural environment and their reactivity with the repository iron structures, I examined how selenite (SeO_3^{2-}) and neptunyl (NpO_2^{+}) react with $GR_{Na,SO4}$. Selenite was reduced readily by reaction at the edge of the GR particles. It converted to trigonal elemental Se(0), while the GR transformed to goethite. When neptunyl reacted with GR, it was reduced to tetravalent Np, and the GR also oxidised to goethite. Following complete oxidation of the green rust suspension slurry, approximately 40% of the Np remained in the tetravalent redox state. The results indicate that Np(IV) is either incorporated in the goethite structure, or it exists as discrete Np(IV)-oxides. The presence of Np(IV) oxides is less likely, because neptunium dioxide are readily oxidise to pentavalent Np.

In this thesis, I have shown that Fe-containing minerals can be used as indicators of redox conditions and that green rust sulphate contains a monovalent cation in the interlayer, namely sodium. Thus, green rust is not solely an anionic exchanger, but can also exchange cations with the surrounding solutions, similar to what is observed for clays. In groundwater transport modelling, parameters describing the behaviour of green rust under aquifer conditions must be included because the compounds react readily with a number of toxic components. In some cases, they are immobilised whereas in others it is possible that they are mobilised by colloidal transport. From my research, it is now even clearer that models intended to simulate or predict groundwater transport of toxic elements should include thermodynamic and kinetic parameters for green rust and its reactivity with dissolved compounds.

Introduction

One of the major elements on Earth is iron, (lat. ferrum). It makes up approximately 34.1 wt % of bulk Earth (ALLEGRE et al., 1995). Although most of the iron is in the core (79.39 wt %), Fe-rich magma is continuously extruded to the surface through the spreading ridges of the ocean crust. The oxygen-rich environment of our Earth influences the redox chemistry of the oceans, soil and atmosphere and iron is one of the redox sensitive elements that it reacts with. Iron-containing minerals can be found virtually everywhere on Earth. In its normal redox-states, ferrous (Fe^{2+}) and ferric (Fe^{3+}), it participates in many important reactions, in corrosion of steel, in microbial activity and in the blood, to carry oxygen. Ferric iron is insoluble at pH above 5; it quickly precipitates as oxides or oxyhydroxides. Ferrous iron on the other hand is soluble and at pH below about 7, the aqueous concentration of Fe(II) may be considerable. In the Archean oceans, iron was a major constituent (BRATERMAN et al., 1983). Today, remnants of dissolved Fe(II) can be found in the extensive Banded Iron Formations, where it records oxidation events that occurred far in past. As oxygen increased in the atmosphere, the dissolved iron became oxidised and precipitated. Knowledge about the behaviour is thus useful for understanding a range of biochemical and geochemical processes and reconstructing the ancient history of Earth.

Fe often exists as ferric-oxides, -hydroxides or -oxyhydroxides, especially near the surface of the Earth's crust. Slightly below the surface, where the concentration of dissolved oxygen is low, aqueous Fe(II) can react with Fe-oxides and hydroxides to form mixed valence phases. The most commonly known is magnetite ($Fe(II)_1Fe(III)_2O_4$). If the ratio of ferrous to ferric iron is relatively high during Fe precipitation, then another group of phases forms, called green rust.

Green Rust (GR) is the generic name originally given by Bernal et al. (1959) to a family of Fe(II)-Fe(III) hydroxy-compounds. They consist of brucite-like layers of Fe(II)-Fe(III) hydroxide that are interlayered with water and anions. This type of layered structure places GR in the group of layered double hydroxides (LDH). The GR family has historically been divided into two groups based on their X-ray diffraction (XRD) patterns (BERNAL et al., 1959): Green rust 1 (GR-1) with a rhombohedral unit cell and green rust 2 (GR-2) with a hexagonal unit cell. This division has later been simplified, depending directly on the shape of the intercalated anions (e.g. (OLOWE and GÉNIN, 1991; ONA-NGUEMA et al., 2002) planar or simple anions such as CO_3^{2-} and Cl^- are indicative of GR-1 type and tetrahedral anions, such as SO_4^{2-} lead to GR-2. Basal plane peaks for GR-1 are in the range of 8.0-7.5 Å for (*003*) and from 4.0-3.75 Å for (*006*). For GR-2, the basal plane for (*001*) is approximately 11 Å, (*002*), roughly 5.5 Å and (*003)*, about 3.75 Å. As a result of the incorporation of organic molecules, the GR classification has been revised (REFAIT et al., 2006; SABOT et al., 2007), based on the unit-cell classification again, i.e. independent of the anion geometry. This makes the system confusing. As part of this thesis I show that one of the simple GR types must contain cations in the interlayer to be stable. This further undermines the classification system. The versatility of green rust structure to form many compounds can be seen in the past 10-15 years. Considering only those that are strictly in the pure Fe(II)-Fe(III) family, 20 have been described (Table 1). Variations reported in Fe(II):Fe(III) ratio has not been considered.

Green Rust Synthesis

In the laboratory, green rust is easy to prepare. It has been studied for almost a century now, but it was not until Feitknecht and Keller in 1950 started to examine it more closely, that the interest expanded. The first GR type to be synthesised was the chlorinated form, which Feitknecht and Keller (1950) investigated. Currently, researchers use one of the four main synthesis pathways to make green rust. Each has advantages over the other. For all synthesis methods the choice of anion for the interlayer is important. Because some anions form separate phases with ferrous iron, the choice of initial Fe-salt must be considered. For example, green rust carbonate cannot be made from ferrous carbonate (siderite), because its solubility is too low.

1) Titration with oxygen

All the solids needed to form GR are added initially (LIN et al., 1996; REFAIT and GÉNIN, 1993), for example to form $GR_{Na,SO4}$, ferrous sulphate and sodium hydroxide are added to water, most commonly with an Fe/OH ratio around 0.6. After mixing, oxygen is added by bubbling air through the suspension. When pH reaches begins to decrease Eh starts to increase rapidly (Fig 1), the suspension has reached the maximum

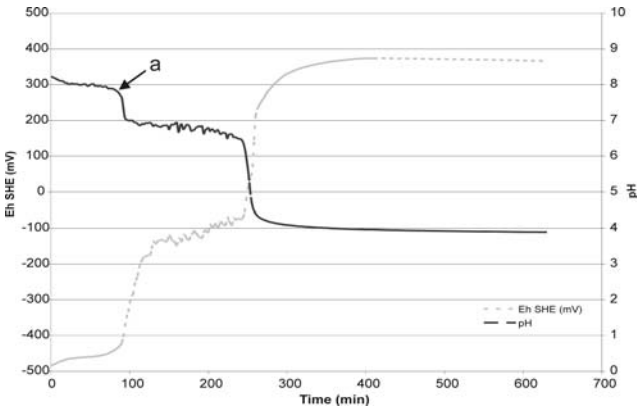

Figure 1. Evolution of pH and Eh during formation and oxidation of $GR_{Na,SO4}$. Point a indicates 100% green rust.

Table 1. Overview of green rust types.

	Anion	*Ideal formula*	*Lattice parameters (Å)*	*Selected references*
GR_{Cl}	Cl^-	$Fe^{2}_{3}Fe^{3}(OH)_8Cl•nH_2O$	a=3.190, c=23.85	(GÉNIN et al., 1998)
GR_{CO3}	CO_3^{2-}	$Fe^{2}_{4}Fe^{3}_{2}(OH)_{12}CO_3•2H_2O$	a=3.18, c=22.45	(DRISSI et al., 1995)
GR_{Br}	Br^-		a=3.18, c=24.2	(VINŠ et al., 1987)
GR_{OH}	OH^-	NB!		(TROLARD and BOURRIÉ, 2006)
GR_F	F^-			(BERNAL et al., 1959)
GR_I	I^-		a=3.19, c=24.8	(VINŠ et al., 1987)
GR_{C2O4}	$C_2O_4^{2-}$	$Fe^{2}_{6}Fe^{3}_{2}(OH)_{16}C_2O_4•3H_2O$	a=3.195, c=23.4	(REFAIT et al., 1998b)
GR_{SO3}	SO_3^{2-}	$Fe^{2}_{6}Fe^{3}_{2}(OH)_{16}SO_3•4H_2O$	a=3.22 c=23.4	(SIMON et al., 1997)
GR_{SO4}	SO_4^{2-}	$Fe^{2}_{4}Fe^{3}_{2}(OH)_{12}SO_4•2H_2O$ $Fe^{2}_{4}Fe^{3}_{2}(OH)_{12}SO_4•8H_2O$	a=3.18 c=10.89 a=5.524 c=11.011	(REFAIT et al., 1998a) (SIMON et al., 2003)
$GR_{Na,SO4}$	Na^+, SO_4^{2-}	$NaFe^{2}_{6}Fe^{3}_{3}(SO_4)_2(OH)_{18}•12H_2O$	a=9.528(6) c=10.968(8)	This work
$GR_{X,SO4}$	X=Ag, Au, or Cu			(O'LOUGHLIN et al., 2003b)
GR_{NO3}	NO_3^-			(GANCEDO et al., 1983) (LEWIS, 1997)
GR_{SeO4}	SeO_4^{2-}	$Fe^{2}_{4}Fe^{3}_{2}(OH)_{12}SeO_4•8H_2O$	a=?, c=10.9	(REFAIT et al., 2000)
GR_{PO4}	PO_4^{2-}		a=?, c=10.4	(HANSEN and POULSEN, 1999; PARMAR, 2001)
GR_{ClO4}	ClO_4^-	$Fe^{2}_{3}Fe^{3}_{2}(OH)_{10}(ClO_4)_2$		(LEWIS, 1997; VINŠ et al., 1987)
GR_{Las}	Linear alkylbenzene sulphonate isomers		a=?, c~28.5	(AYALA-LUIS et al., 2007)
GR_{CHOO}	$CHOO^-$	$Fe(II)_5Fe(III)_2(OH)_{14}(CHOO)_2 •3H_2O$		(GÉNIN and RUBY, 2008; REFAIT et al., 2006)
GR_{C3H5O3}	$C_3H_5O_3^-$		a=3.18, c=44.1	(SABOT et al., 2007)

The existence of a phase with only OH^- in the interlayer, GR_{OH}, which has been named fougerite is doubtful.

formation of GR. With this method it is easy to make larger amounts of GR in a short time. The disadvantages are that if the oxidation rate is too fast, other phases form, such as goethite or magnetite, the pH is not constant during formation, so it does not mimic a natural system and green rust formation depends on initial formation of ferrous hydroxide (white rust, $Fe(OH)_2$); otherwise magnetite or goethite will precipitate.

2) Formation at constant pH

By this method, GR supposedly forms directly and not through a white rust phase ($Fe(OH)_2$) intermediary. The initial ferrous salt is titrated to the desired pH (usually 7.0-7.5) and then maintained constant by adding base while the suspension is oxidised (KOCH and HANSEN, 1997; TAYLOR et al., 1985). pH must be kept below 7.8 to avoid formation of white rust. Oxidation is halted when the amount of base needed to maintain constant pH decreases. Apparently, this method produces particles with a very distinct hexagonal morphology and a high width to thickness ratio (SKOVBJERG et al., 2006).

3) Co-precipitation

This method relies on combining solutions of ferrous and ferric salts in the ratio needed by the stoichiometry of the GR. The suspension is titrated to a pH of between 7 and 7.5 (GÉHIN et al., 2002; REFAIT et al., 2003). The co-precipitation method produces small particles (GÉHIN et al., 2002).

4) Interlayer substitution

This is to some extent a sub-method of the others, because a green rust compound must have already been formed. When a green rust precursor has been precipitated, a solution containing the desired interlayer anion is added. When using this method the relative strength of interlayer binding strength must be considered. For example for LDH compounds the list in increasing strength is: $I^-<NO_3^-<Br^-<Cl^-<F^-<OH^-<SO_4^{2-}<CO_3^{2-}$ (MIYATA, 1983).

In this PhD thesis, I describe the 5 separate studies of iron-mineral/water systems and describe the role of Fe in redox-processes. The main focus in four of the studies is on the mixed Fe(II)-Fe(III) containing mineral group, green rust. The fifth investigates some Fe(III)oxides, which might have originally precipitated as mixed-valent hydroxides.

1 Iron-containing minerals in granitic fractures

In the radioactive waste community, significant effort has gone into understanding the redox-processes that take place, in the near- and far-field environment of a radioactive waste repository. Iron-containing minerals influence the redox potential in the groundwater. In Sweden it is planned to bury the waste in copper clad cast-iron canisters at approximately 500 m depth. The copper is expected to stay chemically stable for the 100.000 years of planned storage, if the groundwater remains reducing. However, if oxidising groundwater reaches the canisters, the copper would eventually corrode and expose the iron and a Galvanic cell would be set up. The last 10,000 years of glacial warming period can be used as a model for what might happen, and the depth to which oxidising water penetrated after the glaciers melted can be used to estimate the depth at which a repository would remain safe.

In the first study (Appendix 1), iron-containing minerals from fractures in the granite of Äspö, Sweden, were examined to establish the paleo-redox boundary. We used Mössbauer spectroscopy in combination with XRD and determinations of the natural stable iron-isotopes to establish the redox state and the formation history of the Fe-oxide minerals. The structure, chemical composition and iron isotope ratio allowed us to reconstruct the paleo-redox conditions in the granitic fractures. We found three types of formation environments: 1) large grained (~100 nm) hydrothermal hematites, 2) very fine-grained (~10 nm) amorphous iron-oxides that had precipitated during drilling and 3) crystalline iron-oxides of intermediate size (10 – 100 nm) which were interpretated to have formed at low temperatures (<10°C) at a depth of less than ~100 m below present ground surface. We found no evidence of oxidising water reaching deeper than 100 m, suggesting that copper-lined canisters buried at ~500 m or deeper is protected against oxidation by atmospheric oxygen. If oxidized water, however, reaches the canisters, GR may form and control the mobility of some of the radioactive compound through redox reactions. This combined with its presence in natural environments makes green rust important to investigate.

2 Natural formation and occurrence of GR

GR is believed to play an important role in the redox-processes that control the composition and structure of Fe-containing compounds (HANSEN et al., 1994; MYNENI et al., 1997; TAYLOR, 1980; TAYLOR, 1984a; TAYLOR, 1984b), whether they result from corrosion of steel or oxidation of dissolved Fe and Fe(II) minerals in soils and groundwater. Stampfl (1969) identified the first occurrence of natural GR on corroded municipal water pipes. GR has since been found in neutral to slightly basic environments where reinforced steel corrodes in medium to high ionic strength brines (KOUNDE et al., 1989; WANG et al., 2001), in soils (TROLARD et al., 1997), in sludge from a water treatment plant (KOCH and MØRUP, 1991), in mine drainage sediments (BEARCOCK et al., 2006) and as I show in this thesis, also in groundwater. Abiotic processes, however, are not the only way GR can form. Several investigations have shown the direct and indirect participation by microorganisms (HANSEL et al., 2003; LACK et al., 2002; ONA-NGUEMA et al., 2002; PARMAR, 2001; ZEGEYE et al., 2005). Because GR is found under both biotic and abiotic conditions, it is believed to exist in the upper groundwater zone, where redox conditions change seasonally.

In the second study (Appendix 2) in this thesis, X-ray diffraction was used to test specially prepared samples for GR in groundwaters. The abundant iron-minerals in the granite and the chlorite in the fractures at Äspö (Fig. 2a) release Fe(II) to the groundwater. In most areas of the Äspö tunnel, the groundwater also contains a relatively high concentration of carbonate, chloride and sulphate (LAAKSOHARJU et al., 1999). When groundwater reaches the atmosphere, Fe(II) quickly forms Fe(III) precipitates (Fig. 2b). However, at less oxidising conditions, GR may very well form. To see if this was the case, groundwaters were tested for the presence of GR.

I also took samples at the island of Bornholm (Fig. 3a). There is an aquifer that has been overexploited. Too much draw-down allowed oxygen entry, so that the iron minerals in the formation have oxidised. When the groundwater level was allowed to move up to its previous level, a substantial amount of pyrite, FeS_2 dissolved, releasing nickel from solid-solution in the pyrite, to the groundwater. The aquifer is now being drained, in hopes of restoring safe drinking water conditions. The water is flowing out into a nearby stream through an artesian well (Fig 3b).

During previous work with synthetic green rust, I observed that when green rust particles were fixed on glass or mica substrates, the rate of oxidation was decreased significantly. Analysis of these plates using X-ray diffraction proved to be an easy way to identify GR from natural samples. This formed the basis for development of a method for the second study (Appendix 2) for natural occurrence of GR. The XRD patterns of samples from the two sites showed clear, though very tiny peaks for GR. Peak spacing indicated green rust chloride or carbonate. In all LDH systems, the most stable form and easiest anion to incorporate is

Figure 2a. Map of sampling site at Äspö, Sweden (Map from Google Maps). b) Sampling at Äspö Tunnel in the SKB Hard Rock Laboratory near Oskarshamn (Borehole SA2273A). Groundwater flows directly out of a sealed pipe set into a fracture system in the granite. Dissolved iron oxidises as it drips from, forming bright red deposits of ferrihydrite ($Fe_{10}O_{14}(OH)_2$). Samples were removed from inside the flowing pipes to insure collection of original reduced groundwater.

Figure 3a) Map of borehole RL 264.761 (GEUS, Denmark) sampling site, indicated by the red arrow (Map from Kort og Matrikelstyrelsen - National Survey and Cadastre). b) Artesian well at the Bornholm site. The well tube is about 0.5 m above water level. The ferrihydrite ($Fe_{10}O_{14}(OH)_2$) red staining on the rocks reveals that dissolved Fe^{2+} in flowing groundwater is high.

carbonate and thus, the most stable form of green rust is GR_{CO3}. Using a commonly used thermodynamic speciation code, PhreeqC, for geochemical modelling, with thermodynamic constants of GR_{Cl} (REFAIT and GÉNIN, 1993), $GR_{Na,SO4}$ (DAVESNE et al., In preparation) and GR_{CO3} (DRISSI et al., 1995), I could show that of the three types of GR (SO_4^{2-}, Cl^- and CO_3^{2-}), the most supersaturated form in the groundwater was GR_{CO3}. Green rust has not been included in previous modelling of groundwater. Our results prove the occurrence of green rust in groundwater from both a granite and a chalk aquifer, indicating that green rust must be included in geochemical modelling if predictions made for toxic component transport are to be valid of groundwater scenarios.

3 Green rust as both anionic and cationic clay

One of the most studied green rust types is that containing sulphate. Its structure has been evaluated a couple of times in the past (BERNAL et al., 1959; HANSEN et al., 1994; SIMON et al., 2003). In the literature, a range of c-axis parameters can be found. I discovered in my synthesis of green rust compounds, the base used to increase pH had a direct result on c-axis length. In 2003, an LDH was described that chemically resembles GR_{SO4} (HUMINICKI and HAWTHORNE, 2003). A cation in the interlayer gave me the idea to examine published GR_{SO4} data more closely. Together with the results from my masters thesis, there was evidence that the published GR_{SO4} structure was incorrect.

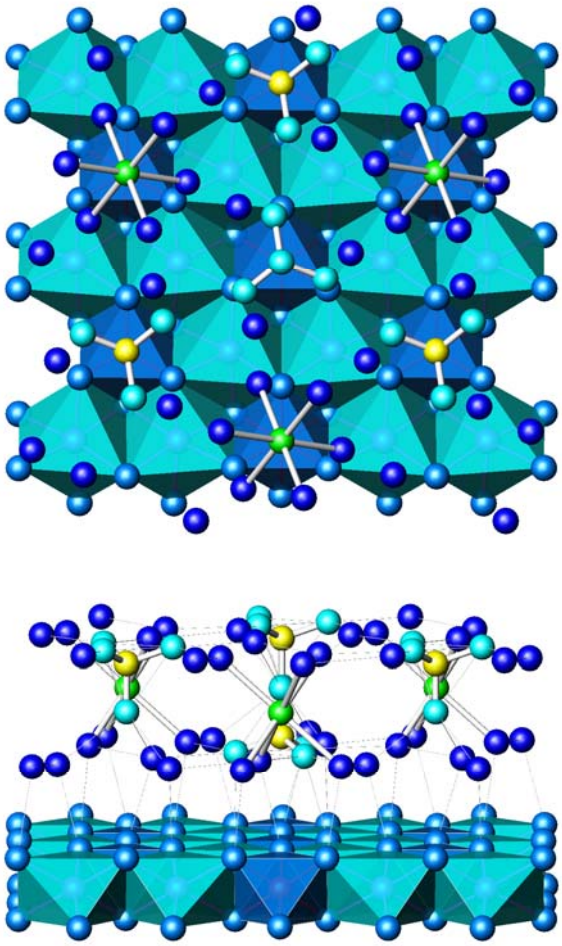

Figure 4a. $GR_{Na,SO4}$ Fe-hydroxide layer and one interlayer, a top view. b) Side view. Probable hydrogen bonds are indicated by thin lines from OH (medium blue) to water molecules (dark blue). View b) is rotated about 75° from a). Light blue coordination octahedra represent Fe(II) and dark blue, Fe(III) coordination sites. The light blue spheres represents oxygen; medium blue, hydroxide; dark blue, oxygen from water; green, Na; yellow, S.

In the third study (Appendix 3) the structure of green rust sulphate was examined in detail. The compound was prepared by the free-drift pH oxidation method (Method 1) and with NaOH as the base. Chemical analysis of the solid showed that sodium was present in larger amounts than could be explained by sorption. X-ray diffraction, Mössbauer spectroscopy and atomic force microscopy, in combination with Rietveld analysis, allowed us to resolve the structure of $GR_{Na,SO4}$. Its composition is $NaFe(II)_6Fe(III)_3(SO_4)_2(OH)_{18}•12H_2O$ and the crystallographic parameters are: space group P-3, with lattice parameters, a = 9.528(6) Å, c = 10.968(8) Å and Z = 1.

The main differences between our model and the ones published previously are that at the centre of the interlayer of our model, there is sodium ion coordinated with water molecules and the sulphate molecules have their three oxygen atoms close to the brucite-like layer (Fig. 4). The incorporation of sodium in the interlayer places this type of GR in the group of both cationic and anionic exchanging clays.

4 Interaction between GR and redox active compounds

A number of inorganic and organic compounds pose a threat to the environment and to human health. For inorganic species it is primarily the valence state that determines toxicity, e.g. chromium(VI), arsenium(V), selenium(VI) and nitrite (NO_2^-) are toxic. The reduced forms, chromium(III), arsenium(III), selenium(0) and N_2O are less so. For organic compounds, it is especially chlorinated solvents that threaten human health. GR is known to react with some of the environmentally problematic or toxic compounds (Table 2). The reaction could involve a change in redox state from a toxic one to one that is less toxic such as Cr(VI) to Cr(III) (SKOVBJERG et al., 2006) and NO_2^- to N_2O (HANSEN et al., 1994), or to an immobile state, such as As(V) to As(III) (LIEN and WILKIN, 2005; RANDALL et al., 2001) or it could involve final transformation into non-toxic compounds such as TCE to CO_2, Cl^- and H_2O (LEE and BATCHELOR, 2002).

Permeable reactive barriers (PRB) use GR to remediate contaminated groundwater (BONIN et al., 1998; HARDY and GILLHAM, 1996; RITTER et al., 2002). One way to make a PRB is to put a mixture of powdered scrap metal iron, about 5% (mm size particles) and sand in a trench (app. 5-20 m deep) in front of the contaminated plume. The iron reacts with the dissolved contaminants as the groundwater passes through the barrier. Sometimes about 5% clay is added to decrease flow rate. The metallic iron reacts with water to form Fe^{2+}. Some ferrous iron adsorbs to the sand, where it react with the redox-sensitive contaminants and form Fe^{3+}. Ferric iron also with Fe^{2+}, forming GR. Ferrous iron in GR is more reactive than sorbed Fe^{2+} (CUI and ERIKSEN, 1996).

In the last studies of research presented in this thesis, I studied how $GR_{Na,SO4}$ reacted with neptunyl (Appendix 4) and selenite (Appendix 5). Both Np(V) and Se(IV) are daughter-products from radioactive spent fuel rods and they can leak into the surrounding environment when a radioactive waste repository decays. Penta-valent neptunium is considered one of the most mobile and least complexing radioactive components of a leaking repository (LUNDÉN et al., 1996). I tested how $GR_{Na,SO4}$ interacts with neptunyl by adding NpO_2^+ a GR suspension (Appendix 4). Using X-ray photon spectroscopy (XPS), atomic force microscopy (AFM), scanning electron microscopy/energy dispersive X-ray spectroscopy (SEM/EDS) and liquid scintillation counting (LSC) I showed that the Np(V) was reduced to Np(IV) at the edges of the GR and in the outermost parts of the

Table 1. Redox sensitive elements that have been investigated for reactivity with green rust. GR serves as an adsorbent or a reducing agent.

Reaction type	Component	Reference
adsorption	As	(LIEN AND WILKIN, 2005; RANDALL ET AL., 2001)
redox reaction	Cr	(LEGRAND et al., 2004; LOYAUX-LAWNICZAK et al., 2000; SKOVBJERG et al., 2006; WILLIAMS and SCHERER, 2001)
	Ag, Au, Cu, Hg	(O'LOUGHLIN ET AL., 2003B)
	NO_2^-	(DHOUIBI ET AL., 2006; HANSEN ET AL., 1994)
	NO_3^-	(BENDER KOCH, 1997; HANSEN et al., 2001; HANSEN and KOCH, 1998; HANSEN et al., 1996)
	Se	(JOHNSON and BULLEN, 2003; MYNENI et al., 1997)
	Sb	(MITSUNOBU et al., 2008)
	Organic compounds	(ELSNER et al., 2004; LEE and BATCHELOR, 2002; LEE and BATCHELOR, 2003; MAITHREEPALA and DOONG, 2004; MAITHREEPALA and DOONG, 2005; O'LOUGHLIN and BURRIS, 2004; ROH et al., 2000a)
	U	(DODGE et al., 2003; O'LOUGHLIN et al., 2003a; ROH et al., 2000b)
	Tc	(PEPPER et al., 2003; ROH et al., 2000b)

interlayer. It was not possible, however, to establish how the Np(IV) was coordinated in the reaction with $GR_{Na,SO4}$. Np(IV) normally oxidises readily when exposed to air, but, when Np-$GR_{Na,SO4}$ was allowed to oxidise completely in air, only 50% of the reduced Np was re-oxidised. Of the Np remaining associated with the solid, 75% was still present as Np(IV). $GR_{Na,SO4}$ is thus able to reduce Np(V) to Np(IV) and possibly immobilise it. In the study of the reaction of selenite with $GR_{Na,SO4}$ (Appendix 5), AFM showed reaction rims at the edges of the of the GR particles (Fig. 5). XRD and solution composition indicated that the reaction had a lag-phase, approximately 10 min. after Se addition, where Se-removal stopped. At the end of the experiment all GR was transformed to goethite and the selenium remained as elemental, trigonal Se(0). $GR_{Na,SO4}$ rapidly reduced and immobilised both selenite and neptunyl.

5 Outlook

My research has uncovered some interesting behaviour of green rust, and has left a number of unanswered questions. My own future work aims at characterising the structure of green rust sulphate where other cations than sodium, are present in the interlayer, e.g. lithium, potassium and rubidium, as well as divalent cations such as calcium. Because it was GR_{CO3} I found in groundwaters, the experiments on neptunium immobilisation should be tested for GR_{CO3} as well. The approximately 4 Å difference in interlayer spacing between GR_{CO3} and $GR_{Na,SO4}$ could lead to a difference in reaction processes and immobilising effects.

My extensive searching of the literature has made it clear that there is need for a critical literature review on green rust literature. A review proposal is accepted by Chemical Reviews. The review will be focusing on GR's chemical composition, structure, thermodynamic

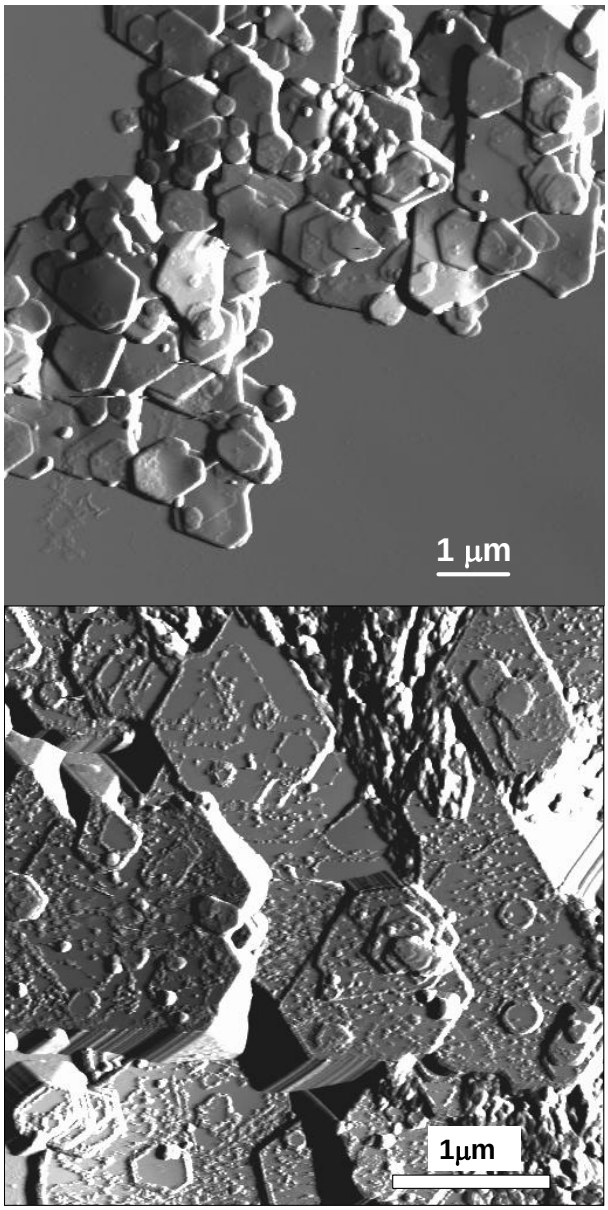

Figure 5. AFM images (deflection mode) of pure, fresh $GR_{Na,SO4}$ (top) and $GR_{Na,SO4}$ after reaction with selenite for 2 hours (bottom). Before reaction, $GR_{Na,SO4}$ has flat surfaces with some terraces that are one or a few unit cells thick. During reaction, terraces disappear and precipitates are left at the edges of where they were. Precipitates also line the edges of the whole crystals. Edges apparently have high reactivity.

and kinetic properties and the processes that affect it,including reaction with redox-sensitive elements and focusing on environmental pollutants.

Many of the studies have treated green rust compounds by washing them. I have found during my work with green rust sulphate that the compound is very reactive. Rinsing destabilises it and leads to dissolution and transformation to other Fe-oxides and hydroxides. This raises the possibility that the results presented from previous studies may be incorrect or at best, modified by sample preparation methods. Some of the parameters have been published by Trolard and colleagues, and expecially the claims of existence of fougerite (TROLARD et al., 2007), a phase that is postulated to contain only OH in the interlayer, should be challenged.

Incorporation of $Fe(CN)_6^{4-}$ and aldehydes in layered double hydroxides and especially in GR is thought to have played an important role in the formation of RNA precursor components in the Archean oceans (ARRHENIUS et al., 1989). With new technical skills and expertise that I have acquired in my study of green rust during my PhD, I think it would be very interesting to make experiments with inorganic ions such as PO_4^{3-}, CO_3^{2-}, CN^- and NH_4^+, that could enter the interlayer of GR. Their incorporation in GR might decrease energy barriers for formation of simple organic molecules.

6 Acknowledgements/Taksigelser

I thank my main advisor, Susan Stipp, for guiding me through the PhD and giving me the opportunity to explore the very interesting topic of green rust; Eva-Lena Tullborg, John Smellie and SKB for making it financially possible; my co-advisor Tonci Balic-Zunic for helping me to understand how crystal structures can be solved; Helene Almind for allowing me to play with different X-ray diffraction preparation techniques and analysis programs to enhance the resolution of the GR data. I am very grateful to Hans Christian Bruun Hansen for bringing the world of green rust to my attention; Birgit Damgaard and Vagn Moser for technical assistance with the AAS in the laboratory at the Geological Institute; the group of Institut für Nukleare Entsorgung,, Forschungszentrum Karlsruhe for being so helpful and open-hearted during my visits, especially Horst Geckeis for arranging and making all the analytical techniques available and Christian Marquardt for helping me in the controlled lab areas; the members of the NanoGeoScience group for discussion and help in the labs and especially Knud Dideriksen, Anna Johnsson, Keld West and Lone L. Skovbjerg for collaboration and constructive critique on papers and my thesis, but also as encouraging sparring partners when things where difficult; all of my friends for getting me out of the lab and office and keeping me socialised; (Danish) og sidst men ikke absolut ikke mindst min familie for, at bære over med de særheder man tilegner sig som PhD studerende, og for at bakke op når jeg syntes det hele var håbløst. Specielt min niece og nevø har ved deres blotte eksistens været et stort mentalt lyspunkt, så tak "Søs" og Svoger for disse to vidunderlige størrelser.

References

Allegre, C. J., Poirier, J.-P., Humler, E., and Hofmann, A. W., 1995. The chemical composition of the Earth. *Earth and Planetary Science Letters* **134**, 515-526.

Arrhenius, G., Bachman, J., Gedulin, B., Hui, S., and Paplawsky, W., 1989. Anion selective minerals as concentrators and catalysts for RNA precursor components. *Origins of Life and Evolution of the Biosphere* **19**, 235-236.

Ayala-Luis, K. B., Kaldor, D. K., Koch, C. B., Strobel, B. W., and Hansen, H. C. B., 2007. Synthesis of linear alkylbenzene sulphonate intercalated iron(II) iron(III) hydroxide sulphate (green rust) and adsorption of carbon tetrachloride. *Clay Minerals* **42**, 307-317.

Bearcock, J. M., Perkins, W. T., Dinelli, E., and Wade, S. C., 2006. Fe(II)/Fe(III) 'green rust' developed within ochreous coal mine drainage sediment in South Wales, UK. *Mineralogical Magazine* **70**, 731-741.

Bernal, J. D., Dasgupta, D. R., and Mackay, A. L., 1959. The oxides and hydroxides of iron and their structural inter-relationships. *Clay mineral bulletin* **4**, 15-30.

Bonin, P. M. L., Odziemkowski, M. S., and Gillham, R. W., 1998. In Situ Identification of Carbonate Green Rust on Iron in Solutions Simulating Groundwater Possible Technological Implications*The 193rd meeting of The Electrochemical Society, Meeting Abstracts*.

Braterman, P. S., Cairns-Smith, A. G., and Sloper, R. W., 1983. Photo-oxidation of hydrated Fe^{2+}-significance for banded iron formations. *Nature* **303**, 163-164.

Cui, D. and Eriksen, T. E., 1996. Reduction of Tc(VII) and Np(V) in solution by ferrous iron*A laboratory study of homogeneous and hetereogeneous redox processes*. Svensk Kärnbränslehantering AB, Stockholm.

Davesne, E., Dideriksen, K., Christiansen, B. C., Ayala-Luis, K. B., Koch, C. B., Hansen, H. C. B., and Stipp, S. L. S., In preparation. Determination of the free energy of formation of sodium- and sulphate-containing green rust (Na-Fe(II)-Fe(III) hydroxide-sulphate). to be submitted to *Geochimica et Cosmochimica Acta*.

Dhouibi, L., Refait, P., Triki, E., and Génin, J.-M. R., 2006. Interactions between nitrites and Fe(II)-containing phases during corrosion of iron in concrete-simulating electrolytes. *Journal of Materials Science* **41**, 4928-4936.

Dodge, C. J., Francis, A. J., Gillow, J. B., Halada, G. P., Eng, C., and Clayton, C. R., 2003. Association of Uranium with Iron Oxides Typically Formed on Corroding Steel Surfaces. *Environmental Science and Technology* **36**, 3504-3511.

Drissi, H., Refait, P., Abdelmoula, M., and Génin, J.-M. R., 1995. The preparation and thermodynamic properties of Fe(II)-Fe(III) hydroxide-carbonate (Green Rust 1); Pourbaix diagram of iron in carbonate-containing aqueous media. *Corrosion Science* **37**, 2025-2041.

Elsner, M., Schwarzenbach, R. P., and Haderlein, S. B., 2004. Reactivity of Fe(II)-Bearing Minerals toward Reductive Transformation of Organic Contaminants. *Environmental Science and Technology* **38**, 799-807.

Feitknecht, W. and Keller, G., 1950. Über die dunkelgrünen Hydroxyverbindungen des Eisens. *Zeitschrift für anorganische Chemie* **262**, 61-68.

Gancedo, J. R., Martinez, M. L., and Oton, J. M., 1983. Formation of Green Rust in NH_4NO_3 solutions. *Anales de Quimica série A* **79**, 470-472.

Géhin, A., Ruby, C., Abdelmoula, M., Benali, O., Ghanbaja, J., Refait, P., and Génin, J.-M. R., 2002. Synthesis of Fe(II-III) hydroxysulphate green rust by coprecipitation. *Solid State Sciences* **4**, 61-66.

Génin, J.-M. R., Refait, P., Simon, L., and Drissi, S. H., 1998. Preparation and E_h-pH diagrams of the Fe(II)-Fe(III) green rust compunds; hyperfine interaction charateristics and stoichiometry of hydroxy-chloride, -sulphate and -carbonate. *Hyperfine Interactions* **111**, 313-318.

Génin, J.-M. R. and Ruby, C., 2008. Composition and anion ordering in some FeII-III hydroxysalt green rusts (carbonate, oxalate, methanoate): The fougerite mineral. *Solid State Sciences* **10**, 244-259.

Hansel, C. M., Benner, S. G., Neiss, J., Dohnalkova, A., Kukkadapu, R. K., and Fendorf, S., 2003. Secondary mineralization pathways induced by dissimilatory iron reduction of ferrihydrite under advective flow. *Geochimica et Cosmochimica Acta* **67**, 2977-2992.

Hansen, H. C. B., Borggaard, O. K., and Sørensen, J., 1994. Evaluation of the free energy of formation of Fe(II)-Fe(III) hydroxide-sulphate (green rust) and its reduction of nitrite. *Geochimica et Cosmochimica Acta* **58**, 2599-2608.

Hansen, H. C. B., Guldberg, S., Erbs, M., and Koch, C. B., 2001. Kinetics of nitrate reduction by green rusts - effects of interlayer anion and Fe(II):Fe(III) ratio. *Applied Clay Science* **18**, 81-91.

Hansen, H. C. B. and Koch, C. B., 1998. Reduction of nitrate to ammonium by sulphate green rust; activation energy and reaction mechanism. *Clay Minerals* **33**, 87-101.

Hansen, H. C. B., Koch, C. B., Nancke-Krogh, H., Borggaard, O. K., and Sørensen, J., 1996. Abiotic nitrate reduction to ammonium: Key role of green rust. *Environmental Science and Technology* **30**, 2053-2056.

Hansen, H. C. B. and Poulsen, I. F., 1999. Interaction of synthetic sulphate "green rust" with phosphate and the crystallization of vivianite. *Clays and Clay Minerals* **47**, 312-318.

Hardy, L. I. and Gillham, R. W., 1996. Formation of Hydrocarbons from the Reduction of Aqueous CO2 by Zero-Valent Iron. *Environmental Science and Technology* **30**, 57-65.

Huminicki, D. M. C. and Hawthorne, F. C., 2003. The crystal structure of nikischerite, Na $Fe^{2+}{}_6Al_3(SO_4)_2(OH)_{18}(H_2O)_{12}$, a mineral of the shigaite group. *The Canadian Mineralogist* **41**, 79-82.

Johnson, T. M. and Bullen, T. D., 2003. Selenium isotope fractionation during reduction by Fe(II)-Fe(III) hydroxide-sulfate (green rust). *Geochimica et Cosmochimica Acta* **67**, 413-419.

Koch, C. B. and Hansen, H. C. B., 1997. Reduction of Nitrate to Ammonium by Sulphated Green Rust. *Advances in GeoEcology* **30**, 373-393.

Koch, C. B. and Mørup, S., 1991. Identification of green rust in an ochre sludge. *Clay Minerals* **26**, 577-582.

Kounde, B., Raharinaivo, A., Olowe, A. A., Rezel, D., Bauer, P., and Génin, J.-M. R., 1989. Mössbauer characterization of the corrosion products of steel in civil works: Suspension bridge and reinforced concrete. *Hyperfine Interactions* **46**, 421-428.

Lack, J. G., Chaudhuri, S. K., Chakraborty, R., Achenbach, L. A., and Coates, J. D., 2002. Anaerobic Biooxidation of Fe(II) by Dechlorosoma suillum. *Microbial Ecology* **43**, 424-431.

Lee, W. and Batchelor, B., 2002. Abiotic Reductive Dechlorination of Chlorinated Ethylenes by Iron-Bearing Soil Minerals. 2. Green Rust. *Environmental Science and Technology* **36**, 5348-5354.

Lee, W. and Batchelor, B., 2003. Reductive Capacity of Natural Reductants. *Environmental Science and Technology* **37**, 535-541.

Legrand, L., Figuigui, A. E., Mercier, F., and Chaussé, A., 2004. Reduction of Aqueous Chromate by Fe(II)/Fe(III) Carbonate Green Rust: Kinetic and Mechanistic Studies. *Environmental Science and Technology* **38**, 4587-4595.

Lewis, D. G., 1997. Factors Influencing the Stability and Properties of Green Rusts. *Advances in GeoEcology* **30**, 345-372.

Lien, H.-L. and Wilkin, R. T., 2005. High-level arsenite removal from groundwater by zero-valent iron. *Chemosphere* **59**, 377-386.

Lin, R., Spicer, R. L., Tungate, F. L., and Davis, B. H., 1996. A study of the oxidation of ferrous hydroxide in sligthly basic solution to produce γ-FeOOH. *Colloids and Surfaces A: Physicochemical and Engineering Aspects* **113**, 79-96.

Loyaux-Lawniczak, S., Refait, P., Ehrhardt, J. J., Lecomte, P., and Génin, J.-M. R., 2000. Trapping of Cr by formation of ferrihydrite during the reduction of chromate ions by Fe(II)-Fe(III) hydroxysalt green rusts. *Environmental Science and Technology* **34**, 438-443.

Lundén, I., Andersson, K., and Skarnemark, G., 1996. Modelling of uranium and neptunium chemistry in a deep rock environment. *Aquatic Geochemistry* **2**, 345-358.

Laaksoharju, M., Tullborg, E.-L., Wikberg, P., Wallin, B., and Smellie, J., 1999. Hydrogeochemical conditions and evolution at the Aspo HRL, Sweden. *Applied Geochemistry* **14**, 835-859.

Maithreepala, R. A. and Doong, R.-A., 2004. Synergistic Effect of Copper Ion on the Reductive Dechlorination of Carbon Tetrachloride by Surface-Bound Fe(II) Associated with Goethite. *Environmental Science & Technology* **38**, 260-268.

Maithreepala, R. A. and Doong, R.-A., 2005. Enhanced Dechlorination of Chlorinated Methanes and Ethenes by Chloride Green Rust in the Presence of Copper(II). *Environmental Science & Technology* **39**, 4082-4090.

Mitsunobu, S., Takahashi, Y., and Sakai, Y., 2008. Abiotic reduction of antimony(V) by green rust ($Fe_4(II)Fe_2(III)(OH)_{12}SO_4{\cdot}3H2O$). *Chemosphere* **70**, 942-947.

Miyata, S., 1983. Anion-exchange properties of hydrotalcite-like compounds. *Clays and Clay Minerals* **31**, 305-311.

Myneni, S. C. B., Tokunaga, T. K., and Brown Jr., G. E., 1997. Abiotic selenium redox transformations in the presence of Fe(II,III) oxides. *Science* **278**, 1106-1109.

O'Loughlin, E. J. and Burris, D. R., 2004. Reduction of halogenated ethanes by green rust. *Environmental Toxicology and Chemistry* **23**, 41-48.

O'Loughlin, E. J., Kelly, S. D., Cook, R. E., Csencsits, R., and Kemner, K. M., 2003a. Reduction of Uranium(VI) by Mixed Iron(II)/Iron(III) Hydroxide (Green Rust): Formation of UO2 Nanoparticles. *Environmental Science and Technology* **37**, 721-727.

O'Loughlin, E. J., Kelly, S. D., Kemner, K. M., Csencsits, R., and Cook, R. E., 2003b. Reduction of Ag^{I}, Au^{III}, Cu^{II} and Hg^{II} by Fe^{II}/Fe^{III} hydroxysulfate green rust. *Chemosphere* **53**, 437-446.

Olowe, A. A. and Génin, J.-M. R., 1991. The mechanism of oxidation of ferrous hydroxide in sulphated aqueous media: importance of the initial ratio of the reactants. *Corrosion science* **32**, 965-984.

Ona-Nguema, G., Abdelmoula, M., Jorand, F., Benali, O., Géhin, A., Block, J.-C., and Génin, J.-M. R., 2002. Microbial Reduction of Lepidocrocite γ-FeOOH by *Shewanella putrefaciens*; The Formation of Green Rust. *Hyperfine Interactions* **139-140**, 231-237.

Parmar, N., Gorby, Y.A., Beveridge, T.J., Ferris, F.G., 2001. Formation of Green Rust and Immobilisation of Nickel in Response to Bacterial Reduction of Hydrous Ferric Oxide. **18**, 375-385.

Pepper, S. A., Bunker, D. J., Bryan, N. D., Livens, F. R., Charnock, J. M., Pattrick, R. A. D., and Collison, D., 2003. Treatment of radioactive wastes: An X-ray absorption spectroscopy study of the reaction of technetium with green rust. *Journal of Colloid and Interface Science* **268**, 408-412.

Randall, S. R., Sherman, D. M., and Ragnarsdottir, K. V., 2001. Sorption of As(V) on green rust ($Fe_4(II)Fe_2(III)(OH)_{12}SO_4{\cdot}3H_2O$) and lepidocrocite (γ-FeOOH): Surface complexes from EXAFS spectroscopy. **65**, 1015-1023.

Refait, P., Abdelmoula, M., and Génin, J.-M. R., 1998a. Mechanisms of formation and structure of green rust one in aqueous corrosion of iron in the presence of chloride ions. *Corrosion Science* **40**, 1547-1560.

Refait, P., Abdelmoula, M., Génin, J.-M. R., and Jeannin, M., 2006. Synthesis and characterisation of the Fe(II-III) hydroxy-formate green rust. *Hyperfine Interactions* **167**, 717-722.

Refait, P., Charton, A., and Génin, J.-M. R., 1998b. Identification, composition, thermodynamic and structural properties of a pyroaurite-like iron(II)-iron(III) hydroxy-oxalate Green Rust. *European Journal of Solid State and Inorganic Chemistry* **35**, 655-666.

Refait, P., Géhin, A., Abdelmoula, M., and Génin, J.-M. R., 2003. Coprecipitation thermodynamics of iron(II-III) hydroxysulphate green rust from Fe(II) and Fe(III) salts. *Corrosion Science* **45**, 659-676.

Refait, P. and Génin, J.-M. R., 1993. The oxidation of ferrous hydroxide in chloride-containing aqueous media and Pourbaix diagrams of green rust one. *Corrosion Science* **34**, 797-819.

Refait, P., Simon, L., and Génin, J.-M. R., 2000. Reduction of SeO_4^{2-} Anions and Anoxic Formation of Iron(II)-Iron(III) Hydroxy-Selenate Green Rust. *Environmental Science and Technology* **34**, 819-825.

Ritter, K., Odziemkowski, M. S., and Gillham, R. W., 2002. An in situ study of the role of surface films on granular iron in the permeable iron wall technology. *Journal of Contaminant Hydrology* **55**, 87-111.

Roh, Y., Lee, S. Y., and Elless, M. P., 2000a. Characterisation of corrosion products in the permeable reactive barriers. *Environmental Geology* **40**, 184-194.

Roh, Y., Lee, S. Y., Elless, M. P., and Foss, J. E., 2000b. Incorporation of radioactive contaminants into pyroaurite-like phases by electrochemical synthesis. *Clays and Clay Minerals* **48**, 266-271.

Sabot, R., Jeannin, M., Gadouleau, M., Guo, Q., Sicre, E., and Refait, P., 2007. Influence of lactate ions on the formation of rust. *Corrosion Science* **49**, 1610-1624.

Simon, L., François, M., Refait, P., Renaudin, G., Lelaurain, M., and Génin, J.-M. R., 2003. Structure of the Fe(II-III) layered double hydroxysulphate green rust two from Rietveld analysis. *Solid State Sciences* **5**, 327-334.

Simon, L., Refait, P., and Génin, J.-M. R., 1997. Transformation of Fe(II)-Fe(III) hydroxysulfite into hydroxysulfate green rusts. *Hyperfine Interactions* **112**, 217-220.

Skovbjerg, L. L., Stipp, S. L. S., Utsunomiya, S., and Ewing, R. C., 2006. The mechanisms of reduction of hexavalent chromium by green rust sodium sulphate: Formation of Cr-goethite. *Geochimica et Cosmochimica Acta* **70**, 3582-3592.

Stampfl, P. P., 1969. Ein Basisches Eisen-II-III-Karbonat in Rost. *Corrosion Science* **9**, 185-187.

Taylor, R. M., 1980. Formation and properties of Fe(II)Fe(III) hydroxy-carbonate and its possible significance in soil formation. *Clay Minerals* **15**, 369-382.

Taylor, R. M., 1984a. Influence of chloride on the formation of iron oxides from Fe(II) chloride; I, Effect of [Cl]/[Fe] on the formation of magnetite. *Clays and Clay Minerals* **32**, 167-174.

Taylor, R. M., 1984b. Influence of chloride on the formation of iron oxides from Fe(II) chloride; II, Effect of [Cl] on the formation of magnetite. *Clays and Clay Minerals* **32**, 175-180.

Taylor, R. M., Schwertmann, U., and Fechter, H., 1985. A rapid method for the formation of Fe(II)Fe(III) hydroxycarbonate. *Clay Minerals* **20**, 147-151.

Trolard, F. and Bourrié, G., 2006. Structure of fougerite and green rusts and a thermodynamic model for their stabilities. *Journal of Geochemical Exploration Extended Abstracts presented at the 7th Symp. on the Geochemistry of the Earth's Surface (GES-7)* **88**, 249-251.

Trolard, F., Bourrie, G., Abdelmoula, M., Refait, P., and Feder, F., 2007. Fougerite, a new mineral of the pyroaurite-iowaite group: description and crystal structure. *Clays and Clay Minerals* **55**, 323-334.

Trolard, F., Génin, J.-M. R., Abdelmoula, M., Bourrié, G., Humbert, B., and Herbillon, A., 1997. Identification of a green rust mineral in a reductomorphic soil by Mössbauer and Raman spectroscopies. *Geochimica et Cosmochimica Acta* **61**, 1107-1111.

Vinš, J., Šubrt, J., Zapletal, V., and Hanousek, F., 1987. Preparation and properties of green rust type substances. *Collection Czechoslovak Chemical communication* **52**, 93-102.

Wang, Z., Moore, R. C., Felmy, A. R., Mason, M. J., and Kukkadapu, R. K., 2001. A study of the corrosion products of mild steel in high ionic strength brines. *Waste Management* **21**, 335-341.

Williams, A. G. B. and Scherer, M. M., 2001. Kinetics of the Cr(VI) reduction by carbonate green rust. *Environmental Science and Technology* **35**, 3488-3494.

Zegeye, A., Ona-Nguema, G., Carteret, C., Huguet, L., Abdelmoula, M., and Jorand, F., 2005. Formation of Hydroxysulphate Green Rust 2 as a Single Iron(II-III) Mineral in Microbial Culture. *Geomicrobiology Journal* **22**, 389-399.

Appendix 1

Fe-oxide fracture fillings as a palaeo-redox indicator: Structure, crystal form and Fe isotope composition

Dideriksen, K; Christiansen, BC; Baker, JA; Frandsen, C; Balic-Zunic, T; Tullborg, E; Morup, S; Stipp, SLS

Chemical Geology

Volume 244, Issues 1-2, 30 Pages 330-343

ELSEVIER

Chemical Geology 244 (2007) 330–343

CHEMICAL GEOLOGY
INCLUDING
ISOTOPE GEOSCIENCE

www.elsevier.com/locate/chemgeo

Fe-oxide fracture fillings as a palæo-redox indicator: Structure, crystal form and Fe isotope composition

K. Dideriksen [a,b,*], B.C. Christiansen [a,b], J.A. Baker [c], C. Frandsen [d], T. Balic-Zunic [b], E. Tullborg [e], S. Mørup [d], S.L.S. Stipp [a,b]

[a] *Nano-science Centre, Chemical Institute, University of Copenhagen, Universitetsparken 5, DK-2100 Copenhagen K, Denmark*
[b] *Geological Institute, University of Copenhagen, Øster Voldgade 10, DK-1350 Copenhagen K, Denmark*
[c] *School of Earth Sciences, Victoria University of Wellington, P.O. Box 600, Wellington, New Zealand*
[d] *Technical University of Denmark, Department of Physics, B. 307, DK-2800 Kgs. Lyngby, Denmark*
[e] *Terralogica AB, Östra Annekärrsvägen 17, SE-443 72 Gråbo, Sweden*

Received 16 January 2007; received in revised form 22 June 2007; accepted 23 June 2007

Editor: D. Rickard

Abstract

Penetration of oxygenated waters to the deeper sub-surface may occur in association with deglaciation events and significantly change the geochemical processes acting at depth. Such a scenario may compromise long-term storage of radioactive waste in underground repositories where copper canisters would corrode in the presence of oxygen. In this study, Fe-oxides from fractures in granite drill-cores and from drilling debris were investigated and a method developed to trace the low-temperature, oxidising conditions which may have been caused by prior deglaciations. X-ray diffraction and Mössbauer spectroscopy showed that all the examined fracture fillings contained Fe-oxides. Based on their structure and form, three genetic types of Fe-oxides were identified: (I) coarse-grained (~ 100 nm) hydrothermal hematite; (II) very fine-grained (~ 10 nm) amorphous Fe-oxides that precipitated during drilling; (III) Intermediate grain-size crystalline Fe-oxides, that are interpreted to have formed naturally at low-temperatures (~ 10 °C).

Fe isotope composition of the Fe-oxides was determined by multiple-collector inductively coupled plasma mass spectrometry using a ^{58}Fe–^{54}Fe double-spike. $\delta^{56}Fe$ of the Fe-oxides ranges from −0.8 to +0.8‰ (relative to the IRMM-14 standard). Hydrothermal samples have intermediate $\delta^{56}Fe$ (−0.3 to 0.0‰), whereas natural low-temperature samples may be isotopically lighter (−0.8 to 0.0‰), and samples precipitated from drilling activity are isotopically heavier (−0.2 to 0.8‰). Within the three genetic suites, $\delta^{56}Fe$ correlates with the relative proportion of Fe(III). For the hydrothermal samples, Fe isotope composition likely reflects input of partially dissolved chlorite. The Fe isotope composition and Fe redox state of the low-temperature and drill-induced samples is consistent with a conceptual model where Fe isotope fractionation occurs during dissolution and oxidation. In our study, the deepest sample showing evidence of natural low-temperature oxidation, putatively as a result of penetration of oxidising surface waters during deglaciation, is from a depth of ~ 100 m.

Keywords: Radioactive waste repository; Oxidation; Fe-oxide; Fractures; Granite; Fe isotope

* Corresponding author. Nano-science Centre, Chemical Institute, University of Copenhagen, Universitetsparken 5, DK-2100 Copenhagen K, Denmark. Tel.: +45 35 32 02 36; fax: +45 35 32 02 14.
E-mail address: knud@nano.ku.dk (K. Dideriksen).

0009-2541/$ - see front matter © 2007 Elsevier B.V. All rights reserved.
doi:10.1016/j.chemgeo.2007.06.027

1. Introduction

A key element in the generation of nuclear energy is responsible storage of waste. In most countries, site selection for underground radioactive waste repositories has been postponed to allow time for collection of data and assessment of a wide range of possible risk scenarios. It is generally agreed that some form of geological disposal is optimum over the long term, provided that stability can be ensured over 10^4 to 10^6 yr. One favourable geological setting for storage of high-level radioactive waste is in granitic rocks, such as those found in the tectonically stable Precambrian shield areas of Sweden, Finland and Canada. In Sweden and Finland, waste is planned to be stored at about 500 m below the surface in copper canisters that will be protected from corrosion as long as a reducing environment prevails in the groundwater, as is likely to be the case under stable climatic and tectonic conditions. However, climatic fluctuations during the Quaternary and current climate change research suggest that future episodes of deglaciation are possible, with timescales of 10^4 to 10^6 yr (e.g., Broecker, 1998). If groundwater flow patterns are dramatically altered by ice advance or retreat in the future, the canisters could be exposed to oxidising waters, thereby compromising repository safety.

Hydrogeological modelling has suggested that groundwater flow conditions could change during glacier melting and subsequent isostatic rebound of the Earth's surface (King-Clayton et al., 1995; Glynn et al., 1999). If oxidising conditions result from future melting events, then one can assume that previous glacier melting associated with the last deglaciation must also have allowed penetration of oxidising waters below current ground level. Thus, it should be possible to test this hypothesis by finding evidence of past, low-temperature, oxidising waters in the sub-surface.

Iron is one of the most abundant elements on Earth. Its redox pair, Fe(II) and Fe(III), has an oxidation potential that conveniently falls within the range of Earth's surface conditions; Fe(II) is soluble and Fe(III) is highly insoluble. Thus, Fe(II)-containing minerals such as hornblende, pyrite, chlorite and biotite can weather, releasing dissolved Fe(II). Interaction of Fe(II) with dissolved oxygen in groundwater produces Fe(III)-oxides, -hydroxides and -oxyhydroxides (grouped and referred to in this paper as Fe-oxides). These minerals are ubiquitous in sediment and soil formed in the presence of oxygen and they often occur in fractures and pore spaces as a result of low-temperature weathering or precipitation from near-surface hydrothermal solutions. Fe(III)-oxides often remain stable even when solutions become reducing again, acting as a historical marker of previous oxidising conditions. However, the presence of an electron donor such as some organic acids or bacteria can, in some cases, redissolve Fe(III)-oxides.

Several properties of Fe-oxides make it possible to distinguish between low-temperature and hydrothermal genesis. In lower temperature (0–120 °C) oxic environments, poorly crystalline ferrihydrite ($Fe_5(OH)_8 \cdot 4H_2O$) quickly precipitates and often ages to crystalline hematite (α-Fe_2O_3) or goethite (α-FeOOH). The favoured secondary phase depends on solution pH and the presence of other elements (Cornell and Schwertmann, 1996). At higher temperatures, ferrihydrite transforms primarily to hematite and, above 250 °C, Fe-oxyhydroxides usually also convert to hematite through thermal dehydration. Similarly, grain size frequently serves as an indicator of formation temperature. During aging, particle size increases to minimize surface free energy (Ostwald ripening). Because this process occurs more rapidly at increased temperature, the particle size of low- and high-temperature Fe-oxides often differs (Cornell and Schwertmann, 1996).

The distribution of stable isotopes of an element between solution and solid phases depends on formation conditions, such as temperature and bonding environment (Urey, 1947). Stable isotopes, especially those of oxygen, have been used as a thermometer for several decades (e.g., Epstein et al., 1953). The bonding environment of an atom is affected by redox conditions, so one would also expect stable isotope fractionation to be influenced by redox reactions. Thus, the Fe isotope composition of Fe-oxide minerals might constrain the temperature and oxidation conditions under which they formed. Several recent studies support this possibility: (i) From theoretical estimates based on spectroscopic data, large isotope fractionation between Fe(II) and Fe(III) is expected (Schauble et al., 2001; Anbar et al., 2005). For example, Schauble et al. (2001) predict a difference in $^{56}Fe/^{54}Fe$ ratios of 5.4‰ between $Fe(II) \cdot 6\,H_2O^{2+}$ and $Fe(III) \cdot 6\,H_2O^{3+}$ at room temperature. (ii) In experimental studies, Fe isotopes show a fractionation between aqueous Fe(II) and Fe(III) of 2.75‰ ($^{56}Fe/^{54}Fe$) at 22 °C and 3.25–3.56‰ at 0 °C (Johnson et al., 2002; Welch et al., 2003). (iii) Studies of natural samples also demonstrate a dependence of Fe isotope fractionation on redox processes. For example, spinels from the upper mantle exhibit variable Fe isotope composition correlated with changes in Fe redox state (Williams et al., 2004) and the Fe isotope composition of HCl leachable minerals in marine sediments is coupled with the relative Fe(II) content of the leachate (Severmann et al., 2006). Particularly important in the context of the objectives of this paper is that isotope fractionation, in general, has

proven to be temperature dependent. Fractionation is thus expected to increase with decreasing temperature, meaning that oxidation under glacial conditions would result in more pronounced Fe isotope fractionation than oxidation in hydrothermal solutions.

Thus, the physical, chemical and Fe isotope characteristics of Fe-oxides offer clues for differentiating between high- and low-temperature formation in the presence or absence of oxygen. The purpose of this study was to characterise Fe-oxides in fractures formed within granitoids of the Oskarshamn region, southeast Sweden, with the aim of determining formation conditions. This area is geologically similar to the sites that are proposed to host radioactive waste repositories in Sweden and has been extensively studied in the last decade. One vertical, triple-tube-drilled borehole (KOV01), located close to the harbour in Oskarshamn, was sampled. Unfortunately, drill-core is only available from depths of 100 to 1000 m so it was not possible to sample the near-surface bedrock from this location. Instead, closer-to-surface samples were taken from the upper part of a core (KAS06) from the island of Äspö. A further sample set was obtained from a very fresh drill-core at Forsmark, with the purpose of examining Fe-oxides that had precipitated as a result of drilling operations. The main focus of this project was to develop a method for identifying if Fe-oxides formed naturally at low-temperature in the presence of oxygen; the method is intended to be applied in a more extensive study to define the depths to which oxidising surface waters have infiltrated in the Äspö/Oskarshamn region.

2. Samples, materials and methods

2.1. Samples

Most of the studied material was sampled from drill-core KOV01 from Oskarshamn (30 km south of Äspö) and KAS06 from Äspö. A detailed description of the geological setting in the Äspö area was published by Kornfält et al. (1997). Briefly, the bedrock consists of granitoids belonging to the ~ 1.8 Ga Transscandiniavian Igneous Belt (TIB). In the Äspö/Oskarshamn area, the TIB ranges from quartz-monzodiorites to granites with lenses and dykes of fine-grained alkali granites. Mylonitisation and brittle deformation of the rocks have produced fractures through which the host rock was altered by a series of hydrothermal events. The secondary hydrothermal minerals that line the fractures include epidote, prehnite, fluorite, quartz, calcite, laumontite, chlorite, pyrite and Fe-oxides. The detailed fracture mineralogy and sequence of paragenetic events are reported in Drake and Tullborg (2004).

Samples of fracture material are designated according to their depth e.g., sample KOV01 146.9 originates from drill-core KOV01, 146.9 m below ground surface. Terrain elevation is a few metres above the level of the Baltic Sea, and the area of study (including both Äspö and the Oskarshamn boreholes) is within a few hundred metres of the coast. Approximately 10% of the fractures in the core contained brownish or reddish precipitate, which were sampled. In addition, a fracture lined with chlorite, but without visible Fe-staining was also sampled. Finally, a sample was taken from the wall of the Äspö Hardrock Laboratory access tunnel at a depth of ~ 180 m.

Although KOV01 was drilled without lubricating mud to minimise fracture contamination, grinding of the drill rods on the rock, and flushing with formation water, may result in iron release from the drilling equipment, inducing precipitation of Fe-oxides in open fractures. On one core sample from KOV01 (112.8), we observed metallic markings indicating drill wear, suggesting that Fe from the drill could contaminate fractures. To study the nature of anthropogenic precipitation, additional material was sampled from borehole KFM02A (Forsmark), 200 km north of Stockholm, where fracture contamination during drilling had been reported. This site is situated on ~ 1.9 Ga Svecofennian meta-igneous rocks of mostly granitic to granodioritic composition (Page et al., 2004). KFM02A was drilled in the same manner as KOV01. The samples were fracture Fe-oxides, pulverised rock material retrieved from the borehole following drilling. We also took samples from the steel drill tube.

2.2. Methods

Samples were characterised with a variety of methods. Except for scanning electron microscopy, where small samples (a few mm or less) were chipped from the cores and examined in situ, the various analyses were performed on the same material, which was scraped from the fracture sides and crushed gently using Fe-free tools.

2.2.1. Characterisation of crystal structure and morphology

X-ray diffraction (XRD) and Mössbauer spectroscopy (MS) were used to identify and characterise the solids. X-ray powder diffraction (PXRD) was performed on a Philips PW 3710 using $Cu_{K\alpha}$ radiation and a graphite monochromator. Based on the Bragg–Brentano principle, the Philips PW 3710 radiation is highly focused, ensuring minimum peak broadening. For samples containing crystalline Fe-oxides, the particle dimensions were estimated

using the Scherrer formula, with reference to XRD patterns of crystalline Fe-oxides, where crystal size is expected to be >1 μm.

Samples with very small quantities of material were analysed on a Bruker AXS Smart 1 K CCD diffractometer using $Mo_{K\alpha}$ radiation, a graphite monochromator, and a collimator 0.5 mm in diameter. Crushed material was inserted into capillary tubes (inside diameter 0.4 mm), which were centred on the four-circle goniometer (capillary tube X-ray diffraction; CT-XRD). The naturally present quartz in the samples was used as an internal standard to calibrate the diffraction angles. CT-XRD could be performed on samples containing as little as ~ 0.5 mg of material. This method, however, considerably broadens the X-ray diffractogram peaks compared to the Philips PW 3710, because focussing is not possible.

Mössbauer spectroscopy probes the energy required for nuclear transition of ^{57}Fe naturally present in the samples. The energy required for nuclear transition reflects the Fe valence state as well as the coordination and magnetic environment of the Fe atoms, thus yielding information about the chemistry, structure and magnetic properties of Fe-bearing material. This means that MS can be used to fingerprint in a fashion similar to XRD for identifying Fe-minerals. One advantage of MS is that poorly crystalline, nanometre-sized material is also identifiable. MS was carried out at the Technical University of Denmark using constant acceleration swingers equipped with ^{57}Co sources in a Rh-matrix. The samples were mounted in plexiglass sample-holders and metallic α-Fe was used for calibration.

Sample morphology was investigated using scanning electron microscopy (SEM) after coating the samples with Pd–Pt. A JEOL JSM-6335F microscope was used to examine crystal morphology and their relationship to other minerals in rock fragments.

2.2.2. Major element concentrations

After dissolution in 6 M HCl, selected supernatants were analysed using atomic absorption spectroscopy (AAS) to determine concentrations of Fe and Al. We used a Perkins Elmer 5100 instrument equipped with a graphite furnace. The method allows Fe and Al concentrations to be established with an accuracy of ~ 5%.

2.2.3. Fe isotope composition

Fe isotope ratios were determined by Multi-collector Inductively-coupled plasma mass spectroscopy (MC-ICP-MS) using a ^{58}Fe–^{54}Fe double-spike to correct for instrumental mass bias (Dideriksen et al., 2006). Analyses were conducted on high concentration Fe solutions (~ 20 ppm), which diminishes the relative contribution of argon-based interferences on the Fe isotope signals. The remaining small interferences were corrected using on-peak-zeroes measured while aspirating blank acid, i.e., the argide signals produced by the blank acid were assumed to be identical to those produced during sample analysis. After dissolution in 6 M HCl and centrifugation, samples were subjected to several steps using concentrated HNO_3 evaporation to oxidise Fe and the remaining solids were redissolved in 6 M HCl. To minimise the influence of matrix elements and isobaric interferences (e.g., ^{54}Cr and ^{58}Ni), the samples were passed once through an anion exchange chromatography column containing Biorad AG-1 X4, 200–400 mesh resin. Further information about the ion exchange procedures can be found in Levasseur et al. (2004), Dideriksen et al. (2006). The collected Fe was then subjected to two evaporative steps using HNO_3 to decrease Cl content, redissolved in 2% HNO_3, and the double-spike added. Before analysis, adequate separation of the analyte from potential interfering matrix elements was tested by verifying that all samples contained only negligible concentrations of Ni, Cr and Ca.

Fe isotopic compositions determined in this work are referenced to standard IRMM-14 (Institute of Reference Material and Measurement, Geel, Belgium) and expressed in the $\delta^{56}Fe$ notation:

$$\delta^{56}\mathrm{Fe} = \left(\frac{\left(^{56}\mathrm{Fe}/^{54}\mathrm{Fe}\right)_{\mathrm{sample}}}{\left(^{56}\mathrm{Fe}/^{54}\mathrm{Fe}\right)_{\mathrm{IRMM-014}}} - 1 \right) * 10^3.$$

Based on replicate analysis of an in-house hematite standard from ETH Zürich, we estimate an external reproducibility for $\delta\ ^{56}Fe$ of ±0.06‰ (2 SD; $n=10$). Uncertainties for the individual analyses presented here are the propagated internal precisions, which for $\delta^{56}Fe$ is ca. ±0.06‰ (2 standard errors, 2 SE = 2 SD/$\sqrt{n}$).

3. Results and discussion

3.1. Characterisation of crystal structure and morphology

Initial examination of all samples with an optical microscope allowed identification of three types:

I. Abundant fracture-fillings consisting of a red, fine-grained material.
II. Brownish and very sparse, fine-grained material, that coated apparently unaltered chlorite linings.
III. Brownish or reddish, very sparse, fine-grained material, coating visibly altered fracture walls.

All samples are individually described in Table 1.

Table 1
Sample descriptions

Core	Depth (m)	Description	Sample group
KAS06	5.9	Scarce, brownish precipitate covering light-green, visibly altered chlorite.	Type III
	14.3	Abundant, red-purple precipitate.	Type I
	19.5	Scarce, brownish precipitate covering light-green visibly altered chlorite.	Type III
KOV01	101.9	Red precipitate staining visibly altered chlorite surface.	Type III
	112.8	Very scarce, brown precipitate on blackish fracture linings that have a glossy appearance.	Type II
	146.9	Red-brown glossy precipitate. Optical microscopy shows larger grains of quartz and feldspar.	Type I
	620.3	Red-brown glossy precipitate. Whitish minerals appear in veins. Optical microscopy shows larger grains of quartz and feldspar.	Type I
	775.8	Brown-purple glossy precipitate. Optical microscopy shows larger grains of quartz and feldspar.	Type I
	782.6	Brown glossy precipitate. Optical microscopy shows quartz grains.	Type I
	Chlorite	Blackish fracture lining. Optical microscopy shows no evidence of staining from Fe-oxide precipitation.	–
KFM02A	642	Very scarce, brown precipitate on blackish fracture linings that have a glossy appearance.	Type II
	Kax	Mud-like material retrieved from the borehole after drilling.	–
	Drill-bit	Piece of drill.	–
	Scraping	Scrapings of rust from the drill.	–

Mineral composition was then defined using conventional PXRD for large samples and CT-XRD for samples with very little material. Fig. 1 shows typical diffractograms for the two methods. Phase composition was determined semi-quantitatively from PXRD (Table 2) by visually matching the patterns to theoretical diagrams calculated from the crystal structure data of minerals. For the CT-XRD measurements, only a crude estimation of quantities was possible. All samples contain quartz and chlorite and most also contain Na or K-feldspars. Some samples also contain calcite, fluorite, muscovite and/or epidote. Most patterns show diffraction maxima typical for Fe-oxides, including hematite, goethite and magnetite.

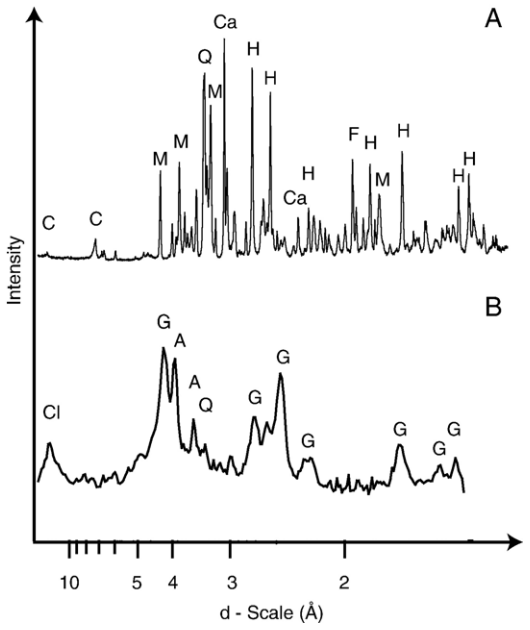

Fig. 1. (A) Powder X-ray diffractogram of sample KOV01 782.6. (B) Capillary tube X-ray diffractogram of sample KAS06 19.5. Note the much broader peaks of the CT-XRD pattern. The phases responsible for the diffraction maxima are: A = glass capillary; C = chlorite; Ca = calcite; Cl = clay, most likely smectite; F = fluorite; G = goethite; H = hematite; M = microcline; Q = quartz.

Type I samples all contain hematite and frequently fluorite, a phase characteristic of hydrothermal origin. These samples had sufficient material for PXRD. The particle size of hematite was estimated to be ~ 100 nm. SEM images of Type I samples revealed platy 80–100 nm particles, which were clustered in aggregates (Fig. 2). These particles were associated with larger, roughly hexagonal, sheet-like particles, typical of chlorite.

Type II samples, such as KOV01 112.8 and KFM02A 642, show no visible diffraction maxima characteristic of Fe-oxides or hydroxides, but a high background suggests larger quantities of amorphous components which can include sub-crystalline metallic iron or its oxides and hydroxides (Mössbauer spectroscopy results described later). Both samples have greater quantities of calcite than Type I samples. KFM02A KAX had the consistency of mud; it was retrieved from the hole after drilling. It contains magnetite as the main component (MS proved an absence of isostructural maghemite) and even some elemental iron, which is most likely derived from the drilling equipment.

CT-XRD of Type III samples shows either goethite or hematite. Unfortunately, peak broadening associated with CT-XRD hindered calculation of the average crystallite size. These samples also contain chlorite and quartz, and more calcite than Type I samples. An exception is sample KAS06 19.5, which is almost pure goethite.

Table 2
Mineral phases identified by XRD

Core	Group	Depth	Method	Hem	Goet	Mag	Fe(0)	Chl	Cl	Q	Fsp	Cal	Fl	Mus	Ep
KAS06	Type III	5.9	CT-XRD		T			M		S	S	S		S	
	Type I	14.3	CT-XRD	S				S		M			M	S	
	Type III	19.5	CT-XRD		M				S	T					
KOV01	Type III	101.9	CT-XRD	T				M		M		M			
	Type II	112.8	PXRD					35		10	20	35			
	Type I	146.9	PXRD	5				25		20	50				
	Type I	620.3	PXRD	5				15		20	45				15
	Type I	775.8	PXRD	10				15		10	40		10	15	
	Type I	782.6	PXRD	10				15		15	40	15	5		
KFM02A	–	KAX	PXRD		10	55	5	T		10	15	5			
	Type II	642	PXRD					5		25	55	15			

Hem = hematite; Goet = goethite; Mag = magnetite; Chl = chlorite; Cl = clay; Q = quartz; Fsp = feldspar; Cal = calcite; Fl = fluorite; Mus = muscovite; Ep = epidote.
Modal proportions of mineral phases are estimated to ±5%; M = major phase; S = subordinate phase; T = trace presence.

Spectra of the hematite-bearing Type I samples display MS absorption lines for hematite, chlorite and possibly epidote (Fig. 3). Hematite in these samples has a magnetic hyperfine field, B_{hf}=51.3±0.3 T at room temperature. This is lower than for pure, crystalline hematite and may indicate Al structural incorporation and/or small particle size (Mørup and Ostenfeld, 2001).

MS of the two Type II samples, for which Fe-oxides could not be identified with XRD (KOV01 112.8 and KFM02A 642), showed, besides a doublet due to chlorite, other components, which must be attributed to phases which were not observed in the XRD measurements. Fig. 4 shows examples of spectra for KOV01 112.8. At all temperatures, but most obvious at room temperature and 150 K, small sextet components resulting from metallic iron and magnetite can be observed. These phases likely arise from contamination by the steel drilling stem and its corrosion products (e.g., García et al., 2003). At lower temperatures, the spectra also display sextet components from magnetically ordered material with a hyperfine field typical for Fe (III) (B_{hf}>40 T). The relative areas of the Fe(III) sextet components increase with decreasing temperature and

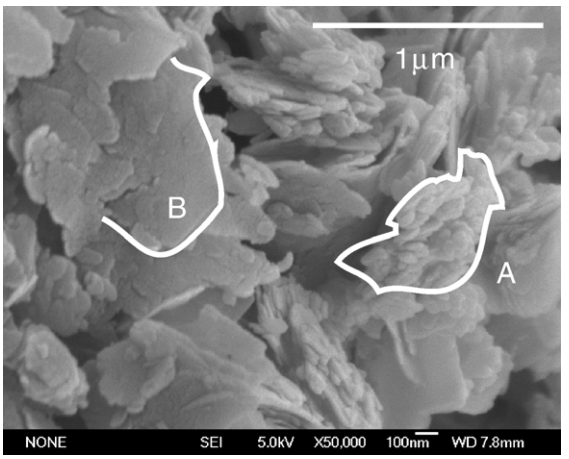

Fig. 2. Scanning electron microscopy image for sample KOV01 146.9. Plate-like particles (80 to 100 nm) that form aggregates (such as A) are consistent with hematite morphology and larger, sheet-like particles (such as B) have morphology typical for chlorite.

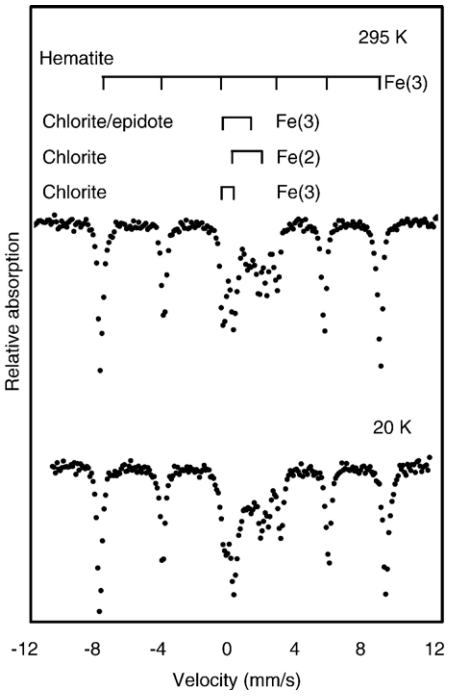

Fig. 3. Mössbauer spectra of sample KOV01 620.3 obtained at RT and 20 K. Absorption lines attributable to Fe(III) in hematite, Fe(II) and Fe(III) in chlorite, as well as a component that may represent Fe(III) in epidote or chlorite are evident.

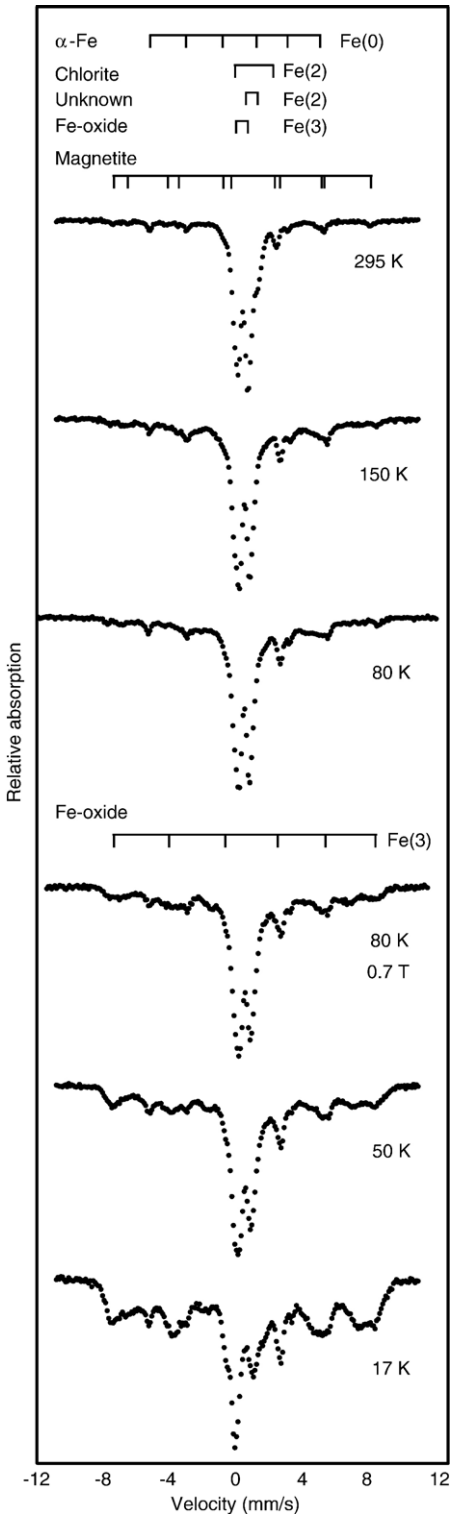

Fig. 4. Mössbauer spectra of sample KOV01 112.8 obtained at various conditions. Note the marked change of appearance as temperature decreases, indicating that Fe-oxides are present as nanometre-sized particles.

also with the application of an external magnetic field at 80 K at the expense of the Fe(III) doublet. This behaviour is consistent with the presence of nanometre-size Fe-oxides (e.g., Mørup et al., 1995; Bødker et al., 2000). For such material, the thermal energy at higher temperatures may be of the same order of magnitude as the energy barrier that separates directions of easy magnetisation. This results in fast fluctuations of the magnetisation directions (superparamagnetic relaxation), leading to collapse of sextets into doublets in the spectra. When a magnetic field is applied to a sample of superparamagnetic particles, relaxation can be suppressed.

For the low-temperature spectra in Fig. 4, good fits required several sextets, indicating that Fe(III) has several coordination environments, possibly indicating the presence of more than one phase. The broad, overlapping lines prevent an unambiguous interpretation but suggest that, consistent with the XRD data, that most of the Fe(III) is present in amorphous or poorly crystalline phases. One of the sextet components in the 17 K spectrum has a magnetic hyperfine field of about 49 T and an isomer shift of 0.45 mm/s. This could be explained by nanoparticles of maghemite or magnetite, minerals commonly observed during corrosion of steel (e.g., García et al., 2003). Such ferrimagnetic nanoparticles can also explain the field dependence of the spectra at 80 K. Another sextet has a magnetic hyperfine field of about 44 T and may be attributed to ferrihydrite. At room temperature, an unidentified Fe(II) phase produces a doublet with an isomer shift of 1 mm/s and quadrupole splitting of 0.5 mm/s. At lower temperatures, absorption from this phase is not visible, probably because it displays magnetic ordering with broad absorption lines.

MS of sample KFM02A 642 also shows an increase of the relative area of magnetically split components with decreasing temperature. For this sample, crystalline oxides can be clearly identified indicating a more ordered Fe-oxide structure. The Mössbauer parameters are in accordance with the presence of maghemite (values for the 150 K spectrum: isomer shift: 0.34 mm/s; quadrupole shift: ~ 0 mm/s; B_{hf}=50.6 T) and goethite (isomer shift: 0.47 mm/s; quadrupole shift: −0.14 mm/s; B_{hf}=43.8 T).

The type III samples in which goethite was identified by XRD (KAS06 5.9 and KAS06 19.5) do not display sextets in the room temperature Mössbauer spectra as expected for crystalline goethite, but only a doublet with an isomer shift of ~ 0.35 mm/s and quadrupole splitting of ~ 0.60 mm/s. This indicates that the goethite particles are so small that they are superparamagnetic at room temperature. Further, in all SEM images of these

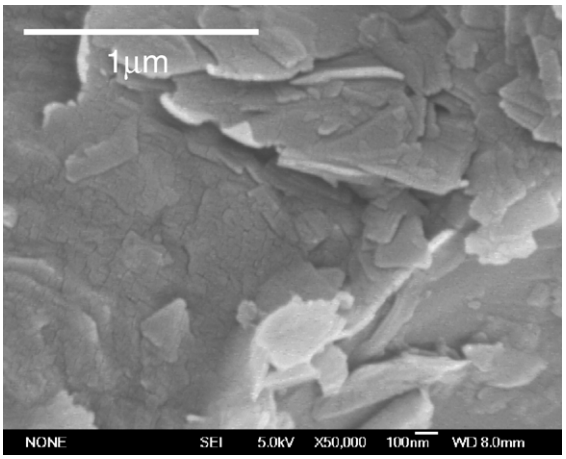

Fig. 5. Scanning electron microscopy image of sample KAS06 19.5. Pt coating or SEM resolution limits prevent observation of nanometre-scale particles showing the expected morphology of crystalline Fe-oxides, such as the thin rods typical of goethite.

samples (Fig. 5), no particles could be identified as having form consistent with crystalline Fe-oxides. For sample KOV01 101.9, MS shows hematite with a magnetic hyperfine field of 50.8 T, significantly lower than the Type I samples, suggesting higher Al incorporation or even smaller particle size than the Type I samples.

The structure and form of the Fe-oxides suggest three mechanisms of formation:

(1) Type I: These hematite-bearing fracture fillings have several characteristics indicating precipitation during hydrothermal activity. First, the material is present in large amounts, and coexists with large quantities of chlorite. Although we sampled only the most Fe-oxide-rich part of the fracture material, no hematite was encountered where chlorite was absent. Chlorite formation usually requires temperatures >50 °C in granitic environments (Walker, 1993; Hillier, 1993). Precipitation of hematite at lower temperature after formation of chlorite would require oxidation of large quantities of dissolved Fe(II), so it is difficult to propose a scenario where fine-grained chlorite would not also be oxidised. By way of comparison, ferrihydrite is currently forming on the walls and in the drainage ditches in the Äspö tunnel where $Fe(II)_{aq}$-bearing groundwater flows out from fractures and is oxidised after exposure to air. However, within the detection limit of XRD it contains no other phases. Ferrihydrite can transform to hematite with time, but SEM images and observed broadening of the hematite peaks in the X-ray diffractograms indicate particle dimension of ~ 100 nm, which is somewhat larger than crystals observed in natural hematite produced at low-temperatures (Cornell and Schwertmann, 1996).

(2) Type II: Fe-oxide precipitate that covers apparently unaltered chlorite contains X-ray amorphous Fe(III)-oxides, which are very fine-grained, indicating rapid formation at low-temperatures. In aqueous, low-temperature and silicate-containing environments, amorphous Fe-oxides transform to more crystalline phases such as goethite and hematite within about 10 yr (Schwertmann et al., 2000) and even faster in the presence of aqueous Fe(II) (Pedersen et al., 2005). The presence of amorphous phases therefore indicates recent formation. Finally, the KOV01 112.8 sample contains traces of Fe(0) indicating anthropogenic input, interpreted to represent transport of material from the drilling operation into the fractures.

(3) Type III: The presence of weathered chlorite and the proximity of the samples to the surface suggest Fe-oxide formation as a consequence of low-temperature oxidation. Furthermore, most samples contain crystalline but very fine-grained goethite, typical of low-temperature genesis. Only the hematite-containing sample, KOV01 101.9, displays a hyperfine field at room temperature, but it is smaller than values observed for the Type I sample suite, indicating a different origin. This is consistent with the weathered appearance of the fracture walls for Type III samples.

3.2. Fe isotope composition

3.2.1. Testing for analytical artefacts as a result of dissolution

Several experiments were conducted during this study to optimise dissolution of Fe-oxides, while ensuring that accompanying silicate phases were only slightly digested and also to evaluate if partial dissolution of Fe-oxides might produce unwanted fractionation of Fe isotope ratios.

Initially, dissolution of samples in 6 M HCl was tested at various temperatures and exposure times. The experiments were performed on material from the natural sample KOV01 146.9, which contained quartz, K-feldspar, hematite and chlorite. Mineralogical and morphological characteristics indicated a hydrothermal origin and MS showed that the chlorite was Fe-poor, meaning that ~ 95% of the Fe resided in hematite. A large batch was finely crushed, thoroughly mixed, and

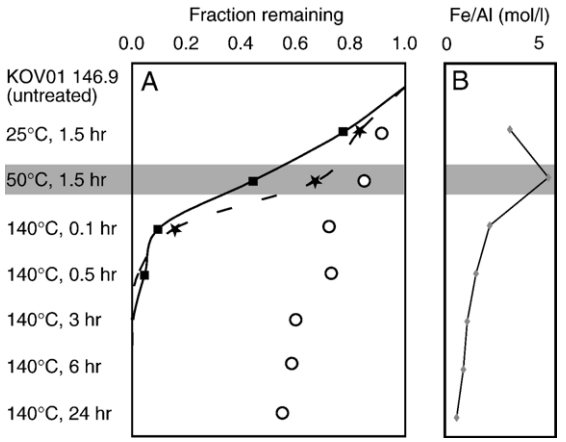

Fig. 6. A) The quartz-normalised content of hematite (black squares) and chlorite (black stars) present in the residue after each of the dissolution tests plotted as a function of the initial quartz-normalised content. Total material remaining (open circles) decreases with increased exposure time and temperature. B) Fe/Al molar ratio of the dissolution supernatant. Optimum conditions that result in maximum dissolution of hematite and minimum dissolution of chlorite are obtained by dissolving for 1.5 h at 50 °C.

divided into equal portions so that the composition of the starting material of each test dissolution experiment would be identical. Each aliquot consisted of ~ 20 mg of material, i.e., comparable to all the other investigated samples. Test samples were then exposed to 6 M HCl at room temperature, 50 °C and 140 °C. Samples at 140° C were exposed for various leaching times to test for full Fe-oxide dissolution.

After dissolution and centrifugation, the residual solid was examined with PXRD to probe leaching selectivity. In these diffractograms, quartz reflections become progressively more dominant with increasing leaching intensity, consistent with progressive dissolution of the Fe-bearing phases and the acid resistance of quartz. To quantify the dissolution of the other phases, the relative contents of hematite, chlorite and feldspar were determined with respect to quartz, i.e., each mineral was normalised to quartz as the internal standard. A major reflection that had minimum interference with peaks from other phases was chosen to represent each mineral (*d*-values: quartz, 3.34; K-feldspar, 3.24; chlorite, 7.10; hematite, 2.70 Å). Normalisation used the intensities of reflections expressed as integrated area of diffraction maxima.

The quartz-normalised mineral content of the residues was compared to the same ratios from the starting material. For example, the hematite to quartz-peak intensity ratio of the initial material was 0.43, compared to 0.33 for the residual remaining after 1.5 h dissolution at room temperature. For dissolution at room temperature, the calculated hematite fraction remaining is 0.33/0.43 or ~ 0.8, indicating that ~ 20% of the hematite had dissolved. Fig. 6A compares the relative proportions of the quartz-normalised residuals for each of the dissolution experiments.

From this figure it can be concluded that the dissolution of hematite was always accompanied by substantial dissolution of chlorite. Because chlorite represents the only important Fe-bearing constituent other than the Fe-oxides, it is important to estimate the proportion of Fe released by chlorite during dissolution. Comparing results of the various dissolutions shows that acid leaching at 50 °C for 1.5 h leads to substantial digestion (>50%) of the Fe-oxides, while minimising digestion of chlorite (~ 30%), suggesting optimal conditions for the purposes of this study. For well-crystalline hematite-bearing samples, where the Fe-oxides are expected to be least soluble, Fe from chlorite may represent 45% of the total Fe, suggesting that for a few Type I samples (KAS06 14.3 and KOV01 620.3) approximately 30% of the released Fe may originate from chlorite (Table 4).

Fe/Al molar ratios of the supernatants are presented in Table 3 and Fig. 6B. The sample digested at 50 °C for 1.5 h has the highest ratio of dissolved Fe to Al, indicating preferential dissolution of Fe-oxides over chlorite. Fe isotope data for the dissolution tests are listed in Table 3. Data might be expected to vary with the extent of dissolution because of: (i) isotopic fractionation during the HCl digestion, (ii) precipitation of secondary Fe-bearing phases, (iii) adsorption of Fe to residual particles, or (iv) release of adsorbed Fe from chlorite. For example, Fe-phase precipitation would be most likely under conditions promoting extensive leaching, where Fe and matrix ion concentration would be high, whereas sorption would be more pronounced where digestion was limited. Fe isotope ratios showed no significant variation (Table 3), suggesting that none of these processes were significant.

Table 3
Fe/Al molar ratio and Fe isotope composition for the supernatant from the dissolution tests on sub-samples of KOV01 146.9 in 6 M HCl at various temperatures and exposure times

T (°C)	Time (h)	Fe/Al	δ^{56}Fe (‰)	2 SE
25	1.5	2.9	–	–
50	1.5	4.7	0.01	0.06
			0.04	0.06
140	0.1	2.0	–	–
140	0.5	1.4	− 0.02	0.06
140	3	1.0	0.02	0.06
140	6	0.8	0.00	0.05
140	24	0.5	0.00	0.06

Table 4
Fe isotope composition of samples

Core	Sample	Sample type	δ^{56}Fe (‰)	2 SE	Fe(III)/ΣFe	Fe_{oxide}/Fe_{chl}	Leached $Fe_{chl}/(Fe_{oxide}+Fe_{chl})$
KAS06	5.9	Type III	−0.37	0.06	0.89	8.1	0.04
	14.3	Type I	−0.26	0.05	0.74	1.3	0.29
	19.5	Type III	−0.08	0.05	0.96	24	0.01
			−0.02	0.05			
KOV01	101.9	Type III	−0.77	0.06	0.89	8.1	0.04
	112.8	Type II	−0.21	0.06	0.64	7.4	0.04
	146.9	Type I	0.01	0.06	0.98	19	0.03
			0.04	0.06			
	620.3	Type I	−0.22	0.06	0.72	1.6	0.26
	775.8	Type I	0.05	0.06	0.95	6.1	0.08
	782.5	Type I	0.04	0.06	0.88	4.6	0.11
	Chlorite	–	−0.39	0.06	0.43	0	1
KFM02A	KAX	–	0.26	0.06	0.70	49	0.01
	642	Type II	0.75	0.06	0.75	4.0	0.08
	Drill-bit[a]	–	0.07	0.06	–		
	Scrapings[a]	–	0.10	0.06	–		

Unless noted otherwise, all material was exposed to 6 M HCl at 50 °C for 1.5 h. Fe_{oxide}/Fe_{chl} from Mössbauer data. Leached $Fe_{chl}/(Fe_{oxide}/Fe_{chl})$ is calculated from Fe_{oxide}/Fe_{chl} assuming a chlorite dissolution of 30% for all samples and a Fe-oxide dissolution of 55% for type I samples and 100% for type II (drill-induced) and type III (natural low-temperature) samples.
[a] Samples were dissolved completely during exposure to 6 M HCl for 24 h.

The Fe-oxides of the KOV01 146.9 sample are not representative for the whole sample suite; it is feasible, that Fe-oxides that formed at lower temperature could be isotopically zoned, in which case partial dissolution would reflect the signature of the outer rims of the particles (Skulan et al., 2002). However, the lower temperature Type II and III Fe-oxides are poorly crystalline with a particle size smaller than for Type I and because dissolution rate depends on surface area, leaching is expected to proceed rapidly for the fine-grained samples. To test this, the solid left as residue after dissolution from some of the other samples (KAS06 19.5, KOV01 101.9 and KFM02A KAX) that originally contained goethite, hematite, or magnetite, was probed with CT-XRD. Diffractograms showed no sign of Fe-oxides after dissolution.

3.2.2. Fe isotope ratios of samples

Table 4 and Fig. 7 present Fe isotope results. Type I samples, shown by the mineralogical and morphological examination to be of hydrothermal origin, have an average δ^{56}Fe = − 0.1‰ with relatively little variation (2 SD = ±0.3‰; n = 5). Type II samples, for which Fe-oxide structure and form suggest formation as an artefact of drilling, are on average heavier in Fe isotope composition (δ^{56}Fe = +0.2‰) and display greater variation (2 SD = ±0.8‰; n = 3). Finally, Type III samples of natural, low-temperature genesis have an Fe isotope composition averaging δ^{56}Fe = −0.4‰ with considerable variation (2 SD = ±0.7‰; n = 3). Thus, Fe isotope data show trends consistent with sample origin, but do not by themselves allow conclusions about the genetic history of the Fe-oxides.

The Fe isotope composition does, however, display a systematic relationship when compared with Fe redox state. Fig. 8 plots relative Fe(III) content versus δ^{56}Fe for the three sample types. It shows groupings for the hydrothermal, drill-induced and natural low-temperature Fe-oxides. For the hydrothermal samples, release of Fe from chlorite associated with the hematite could affect the Fe isotope/redox state relationship. To probe the effect of chlorite leaching, data were collected for a chlorite sample from core KOV01. Microscopic examination of the black-greenish sample revealed no sign of staining with Fe-oxides and neither PXRD or MS showed any evidence of crystalline Fe-oxides in that sample. Its Fe isotope composition and redox state, plotted in Fig. 8, suggest that if we assume the pure chlorite sample to be representative of the chlorite in the mixed chlorite/hematite samples, partial dissolution of chlorite can account for the Fe isotope/redox state relationship observed for the hydrothermal samples. Thus, the hydrothermal sample data may be explained by mixing of Fe-oxides, with $\delta^{56}Fe \approx 0$‰, and chlorite, with $\delta^{56}Fe \approx -0.5$‰.

For the drill-induced or low-temperature samples, chlorite Fe constitutes less than 20% of the samples' total Fe (compared to 45% for some hydrothermal samples) and leaching leads to complete dissolution of the Fe-oxides, thus decreasing the effect of partial chlorite dissolution significantly. Assuming that the dissolution behaviour of the chlorite in sample KOV01

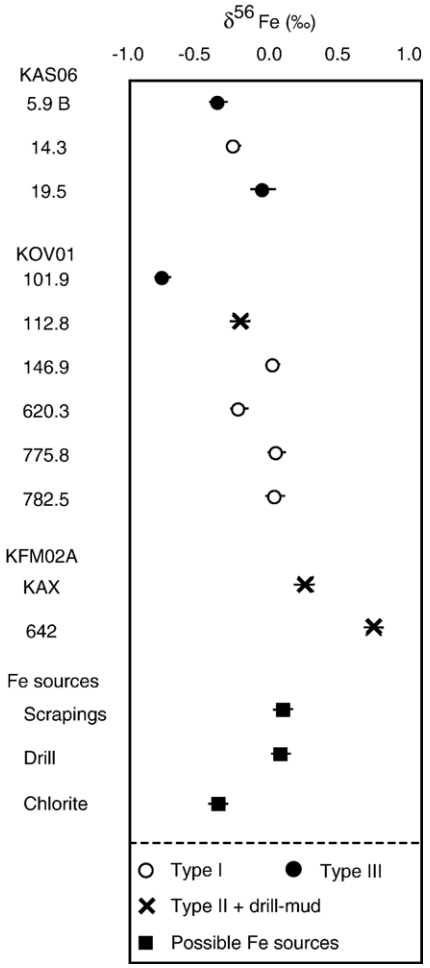

Fig. 7. Fe isotope composition of samples after dissolution in 6 M HCl for 1.5 h at 50 °C.

146.9 is similar to that of the chlorite in the remaining samples, Fe from chlorite amounts to less than 10% of the total released Fe for the drill-induced and natural low-temperature samples (Table 4).

Although the number of samples is small, the trends shown by Fig. 8 are clear. A higher Fe(III) to Fe_{tot} ratio is associated with heavier Fe isotope composition, suggesting that the processes responsible for changing redox state are linked to Fe isotope fractionation. The shift in Fe isotope and Fe redox data for the drill induced and the low-temperature samples allows differentiation between the two types. There are several processes that may be responsible for fractionation in these two types:

1) *Dissolution* of Fe-bearing phases, notably the ubiquitous chlorite as well as the steel drill. Studies of Fe isotope fractionation during dissolution of hornblende demonstrate non-stoichiometric dissolution of Fe-bearing silicate and the formation of an Fe-leached layer through which cations must diffuse. This is likely to promote preferential release of isotopically light Fe, especially when release is promoted by organic ligands or bacteria (Brantley et al., 2004). For chlorite, non-stoichiometric dissolution with preferential release of Fe has been reported for low pH solutions (Brandt et al., 2003) favouring release of cations from the hydroxide layer and possibly leading to localised alteration of the chlorite to vermiculite/smectite. This suggests that chlorite dissolution may fractionate Fe isotopes if: (i) the Fe coordinated in the 2:1 layers and hydroxide sheets differs in valence as has been suggested (e.g., Borggaard et al., 1982), then fractionation associated with oxidation is affected (details below), (ii) isotope composition of the two structural components differs, or (iii) the interstratified vermiculite/smectite acts as a barrier through which Fe must diffuse before release in a manner similar to that of the hornblende leached layer.

For dissolution of metallic Fe from the drill, the formation of a more permanent leached layer is improbable considering the continuous abrasion that the drill, core casing and drilling rods are subjected to. Thus, one can assume that Fe released from the drill inherited the Fe isotope composition of the steel. The similarity in Fe isotope composition of drill ($\alpha^{56}Fe = 0.10 \pm 0.06$‰) and Fe-oxide scrapings from the drill after use ($\alpha^{56}Fe = 0.07 \pm 0.06$‰) support this. These results also indicate that the drill-induced Fe-

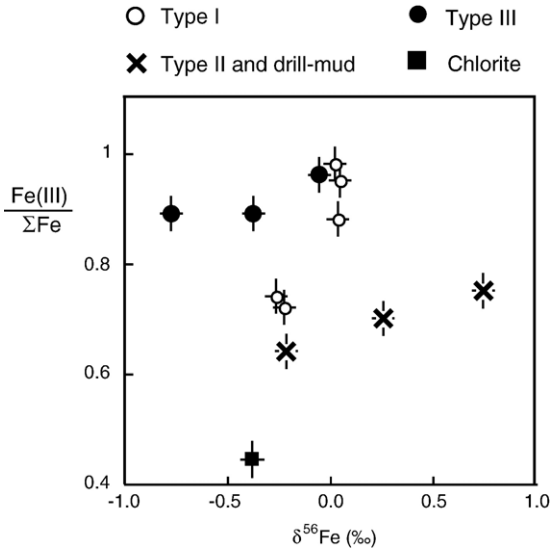

Fig. 8. Fe redox state plotted as a function of Fe isotope composition. Uncertainties for Fe(III) concentrations determined by Mössbauer spectroscopy are estimated to be ~ 3%, based on computer fitting with various peak symmetry and peak intensity ratio constraints.

oxides are not simply ground-up pieces drill, but rather that they are the result of processes entailing Fe isotope fractionation.

2) *Oxidation* of dissolved Fe(II). Laboratory studies have shown significant fractionation between aqueous complexes of Fe(II) and Fe(III), with reported temperature dependence ranging from $\Delta^{56}Fe_{Fe(III)-Fe(II)} \approx 2.8‰$ at 22 °C to $\Delta^{56}Fe_{Fe(III)-Fe(II)} \approx 3.5‰$ at 0 °C (Johnson et al., 2002; Welch et al., 2003). Thus, partial oxidation leads to a Fe(III) pool that is heavier in Fe isotopes, with composition controlled by the Fe(II) to Fe(III) ratio. For example, if nearly all Fe is oxidised, or dominantly Fe(III) is released, the resulting Fe(III) isotope composition would be close to that of the initial composition.

3) *Precipitation* of Fe-oxides. Equilibrium fractionation factors for slow rates of Fe-oxide precipitation have been estimated from spectroscopic data and modelling using density function theory (Polyakov and Mineev, 2000; Schauble et al., 2001; Anbar et al., 2005). Results indicate that fractionation between Fe^{3+} and Fe-oxides favours incorporation of lighter isotopes for goethite and hematite and heavier isotopes for magnetite (Schauble et al., 2001; Anbar et al., 2005). Notably, predicted fractionation is smaller than that determined for oxidation. Unfortunately, experimental information on the behaviour of Fe isotopes during precipitation is currently limited; fast precipitation of hematite from Fe(III) solution leads to preferential uptake of the lighter isotopes by the solid, whereas slower precipitation, closer to chemical equilibrium, leads to hematite with an isotope composition similar to the dissolved Fe^{3+} (Skulan et al., 2002).

For the sample suite, we observed that: (i) within the drill-induced and low-temperature Fe-oxide types, redox state was correlated with Fe isotope composition; more oxidised samples were dominated by heavier isotope fractions, and (ii) the Fe isotope composition of the drill-induced samples was on average heavy, especially considering their relatively reduced redox state. In contrast, the samples interpreted to be of natural, low-temperature origin, had a lighter average Fe isotope composition.

There are two conclusions to be made from these observations. First, fractionation associated with oxidation is likely to have been important in developing the observed redox dependence of the Fe isotope composition. Here, insoluble and isotopically heavier Fe(III) is expected to be incorporated in the Fe-oxides, whereas the more soluble and isotopically lighter Fe(II) is lost to the environment.

Second, isotope fractionation associated with dissolution may also be important. For the natural, low-temperature samples, where the Fe-oxides are likely to have formed from Fe released from chlorite, leaching may have released isotopically lighter Fe through kinetic isotope effects, leading to the lighter Fe isotope composition of samples in this group. Also, for the low-temperature samples, oxidation may have been intense and resulted in extensive transformation of Fe(II) to Fe (III), meaning that the isotope composition of the Fe-oxides largely reflects that of the leached Fe. Alternatively, leaching of Fe from domains in the chlorite, where Fe isotope composition or valence differ from bulk composition, may also lead to the observed values. For example, preferential release of Fe(III), which has been reported to dominate the Fe pool of chlorite hydroxide layers (Borggaard et al., 1982; Kloprogge and Frost, 2000), would mean that oxidation and the associated fractionation would be limited. Thus, the Fe isotopes incorporated in the Fe-oxides would be mostly affected by fractionation during dissolution. The Fe released from the drill is, however, expected to be largely unaffected by fractionation during leaching and thus likely reflects the heavier isotopes of the drill-derived material ($\delta^{56}Fe = 0.10 \pm 0.06‰$). For the drill-induced sample group, oxidation may also have been less intense, resulting in significant loss of isotopically light Fe(II) to the environment and a heavier residue in the Fe-oxides.

4. Conclusions and implications

The structure, form and chemical composition of Fe-oxides sampled from drill-cores and from the well slurry after drilling indicate three different genetic origins for fracture material: Hydrothermal precipitation, natural low-temperature formation and drill-induced contamination.

The hydrothermal samples consist of well-crystallised hematite with particle sizes (~ 100 nm) somewhat larger than typical soil hematite (Cornell and Schwertmann, 1996). The natural, low-temperature samples are also well-crystallised, but they have a significantly smaller particle size, consistent with low-temperature formation. The drill-induced samples from the cores are X-ray amorphous and have particles of ~ 10 nm or less. Some of these samples contain Fe(0) and others possibly contain very fine-grained maghemite, a phase typically associated with steel corrosion.

For all three sample groups, Fe isotope composition correlates with redox state. For the hydrothermal samples, Fe isotope composition probably reflects partial leaching of Fe-oxides and chlorite having different isotope composition. The observed Fe isotope composition of the low-temperature and the drill-induced samples agrees with that expected from fractionation occurring during dissolution and oxidation.

In this investigation, we have found no evidence for the formation of natural, low-temperature Fe(III)-oxides beneath a depth of ~ 100 m below current ground surface. However, recognising that the distribution of fractures in granite bedrock is likely to be inhomogeneous and that some fractures might have been open during deglaciation that are closed now, there is a relatively large margin of uncertainty about the actual depth of the redox boundary. Furthermore, considering the relatively small sample set, we cannot exclude the possibility that low-temperature Fe(III)-oxides might also exist in deeper fractures that were not sampled.

Nevertheless, the results of this investigation suggest that oxidising waters have reached as far as 100 m below ground surface and that these waters were at low-temperature when the Fe(III)-oxides formed. Currently, the redox boundary in the groundwater of the Oskarshamn/Äspö area is estimated to vary from depths of a few metres down to possibly 100 m at certain places (e.g., in highly transmissive fracture zones and in areas with a higher topography) (Laaksoharju, 2004). The presence of low-temperature precipitates from Äspö island (5.9 and 19.5 m depth) is in good agreement with interpretations made from U-series analyses (Tullborg et al., 2003) indicating a redox front at ~ 20 to 30 m depth at Äspö. In the Oskarshamn borehole, the present study has identified low-temperature precipitates at 101.9 m. This is consistent with the higher topography in the vicinity of the borehole and the presence of several larger fracture zones, all of which suggest a deeper redox front in this borehole than on Äspö Island.

In our study, we have made no attempt to constrain the age of the Fe-oxide formation. It is possible that the natural, low-temperature Fe-oxides predate recent glacial events and be the result of oxidative deep-weathering, for example during periods of warming. However, prolonged intervals of oxidative deep-weathering would entail significant transformation of fracture material; the natural, low-temperature Fe-oxide samples are of minute quantities and contain Fe(II)-bearing chlorite, inconsistent with such a scenario. The presence of hematite that has not recrystallised agrees with precipitation in the fairly recent geological past i.e., Quaternary. Although Fe(III)-oxides can be dissolved again when redox conditions change, they are relatively resistant. Conversion from solid Fe(III) to Fe(II), requires a reducing agent, such as redox-active organic acids or electron-donating bacterial activity. Thus, the absence of low-temperature Fe-precipitates at greater depth suggests that glacier advance or retreat either: (i) does not lead to general and significant change of the flow patterns over time periods long enough to be registered by precipitation of Fe-oxides in fractures, or (ii) that the oxic water from glaciers that can penetrate into fractures opened during rebound is deoxygenated by reaction with minerals exposed in the fractures within a few tens of metres of the surface, such as the weathered chlorite observed underneath the natural, low-temperature hematite. Thus, although degradation of organic matter might not consume oxidation capacity in fresh glacier melt-water, in contrast to soil/sediment activity in the Äspö-Oskarshamn region at present, at the time of deglaciation, fracture surfaces themselves may offer redox buffer capacity, preventing deep penetration of oxic waters, until organic matter would have time to accumulate on a newly exposed moraine surface. The investigated area is similar in geology to the sites proposed as hosts for radioactive waste repositories in Sweden. In our study, we have not found evidence indicating that deep penetration of oxygenated water is likely to compromise the safety of such repositories, which are planned to be situated at a depth of ~ 500 m below ground surface.

Acknowledgements

We thank Helge Rasmussen and Daniel E. Madsen for performing Mössbauer spectroscopy on some of the samples, Helene Almind for help with X-ray diffraction, Birgit Damgaard for analyses by atomic absorption spectroscopy, and Bjarne Bisballe for access to scanning electron microscopy facilities. Martin Bizzarro and David Ulfbeck contributed to valuable discussions about the Fe isotope results, and Helen Williams kindly provided the ETH Zürich in-house Fe standard. We are grateful for the valuable input and discussions on Fe-oxide genesis offered by John Smellie and Ignasi Puigdomenech, as well as Peter Wikberg who initiated this project and comments offered by Donald Canfield, Mark Rehkamper, Clark Johnson and Derek Vance. Funding was provided by SKB (Svensk Kärnbränslehantering AB). The NanoGeoScience laboratory was established by a grant from the Danish Natural Sciences Research Council.

References

Anbar, A.D., Jarzecki, A.A., Spiro, T.G., 2005. Theoretical investigation of iron isotope fractionation between $Fe(H_2O)_6^{3+}$ and $Fe(H_2O)_6^{2+}$: implications for iron stable isotope geochemistry. Geochim. Cosmochim. Acta 69, 825–837.

Bødker, F., Hansen, M.F., Bender Koch, C., Lefmann, K., Mørup, S., 2000. Magnetic properties of hematite nanoparticles. Phys. Rev., B 61, 6826–6838.

Borggaard, O.K., Lindgreen, H.B., Mørup, S., 1982. Oxidation and reduction of structural iron in chlorite at 480 °C. Clays Clay Miner. 30, 353–364.

Brandt, F., Bosbach, D., Krawczyk-Bärsch, E., Arnold, T., Bernhard, G., 2003. Chlorite dissolution in the acid pH-range: a combined

microscopic and macroscopic approach. Geochim. Cosmochim. Acta 67, 1451–1461.

Brantley, S.L., Liermann, L.J., Guynn, R.L., Anbar, A., Icopini, G.A., Barling, J., 2004. Fe isotopic fractionation during mineral dissolution with and without bacteria. Geochim. Cosmochim. Acta 68, 3189–3204.

Broecker, W.S., 1998. The end of the present interglacial: how and when? Quat. Sci. Rev. 17, 689–694.

Cornell, R.M., Schwertmann, U., 1996. The Iron Oxides: Structure, Properties, Reactions, Occurrences and Uses. Wiley VCH, New York.

Dideriksen, K., Baker, J.A., Stipp, S.L.S., 2006. Iron isotopes in natural carbonate minerals determined by MC-ICP-MS with a ^{58}Fe–^{54}Fe double spike. Geochim. Cosmochim. Acta 70, 118–132.

Drake, H., Tullborg, E-L., 2004. Fracture mineralogy and wall rock alteration. Results from drill core KSH01A+B. Oskarshamn site investigation. Swedish Nuclear Fuel and Waste Managements Co. SKB P-04-250.

Epstein, S., Buchsbaum, R., Lowenstam, H.A., Urey, H.C., 1953. Revised carbonate-water isotopic temperature scale. Geol. Soc. Amer. Bull. 64, 1315–1325.

García, K.E., Morales, A.L., Arroyave, C.E., Barrero, C.A., Cook, D.C., 2003. Mössbauer characterization of rust obtained in an accelerated corrosion test. Hyperfine Interact. 148/149, 177–183.

Glynn, P.D., Voss, C.I., Provost, A.M., 1999. Deep penetration of oxygenated meltwaters from warm based ice sheets into the Fennoscandian shield. Use of Hydrogeochemical Information in Testing Groundwater Flow Models. Technical summary and proceedings of a workshop, Borgholm, Sweden, September 1–3, 1997. Nuclear Energy Agency and Organization of Economically Developed Countries, pp. 201–241.

Hillier, S., 1993. Origin, diagenesis, and mineralogy of chlorite minerals in Devonian lacustrine mudrocks, Orcadian Basin, Scotland. Clays Clay Miner. 41, 240–259.

Johnson, C.M., Skulan, J.L., Beard, B.L., Sun, H., Nealson, K.H., Braterman, P.S., 2002. Isotopic fractionation between Fe(III) and Fe(II) in aqueous solutions. Earth Planet. Sci. Lett. 195, 141–153.

King-Clayton, L.M., Chapman, N.A., Kautsky, F., Svensson, N-O., Marsely, G., Ledoux, M., 1995. The Central Scenario for SITE-94: A Climate Change Scenario. SKI report, vol. 95:42. Swedish Nuclear Power Inspectorate (SKI). (Can be ordered free of charge at www.ski.se).

Kloprogge, J.T., Frost, R.L., 2000. Thermal decomposition of Ferrian chamosite: an infrared emission spectroscopic study. Contrib. Mineral. Petrol. 138, 59–67.

Kornfält, K.A., Persson, P.O., Wikman, H., 1997. Granitoids from the Äspö area, southeastern Sweden: geochemical and geochronological data. GFF 119, 109–114.

Laaksoharju, M. (Ed.), 2004. Hydrogeological evaluation for Simpevarp model version 1.2. Preliminary site description of the Simpevrp area. Swedish Nuclear Fuel and Waste Managements Co. SKB R-04-74.

Levasseur, S., Frank, M., Hein, J.R., Halliday, A.N., 2004. The global variation in the iron isotope composition of marine hydrogenetic ferromanganese deposits: implications for seawater chemistry. Earth Planet. Sci. Lett. 224, 91–105.

Mørup, S., Ostenfeld, C.W., 2001. On the use of Mössbauer spectroscopy for characterisation of iron oxides and oxyhydroxides in soils. Hyperfine Interact. 136, 125–131.

Mørup, S., Bødker, F., Hendriksen, P.V., Linderoth, S., 1995. Spin-glass-like ordering of the magnetic moments of interacting nano-sized maghemite particles. Phys. Rev., B 52, 287–294.

Page, L., Hermansson, T., Söderlund, P., Andersson, J., Stephens, M.B., 2004. Bedrock mapping U/Pb, ^{40}Ar/^{39}Ar an (U–Th)/He geochronology. Forsmark site investigation. Swedish Nuclear Fuel and Waste Managements Co. SKB P-04-126.

Pedersen, H.D., Postma, D., Jakobsen, R., Larsen, O., 2005. Fast transformation of iron oxyhydroxides by the catalytic action of aqueous Fe(II). Geochim. Cosmochim. Acta 69, 3967–3977.

Polyakov, V., Mineev, S., 2000. The use of Mössbauer spectroscopy in stable isotope geochemistry. Geochim. Cosmochim. Acta 64, 849–865.

Schauble, E.A., Rossman, G.R., Taylor Jr., H.P., 2001. Theoretical estimates of equilibrium Fe-isotope fractionation from vibrational spectroscopy. Geochim. Cosmochim. Acta. 65, 2487–2497.

Schwertmann, U., Friedl, J., Stanjek, H., Schulze, D.G., 2000. The effect of Al on Fe oxides. XIX. Formation of Al-substituted hematite from ferrihydrite at 25 degrees C and pH 4 to 7. Clays Clay Miner. 48, 159–172.

Severmann, S., Johnson, C.M., Beard, B.L., McManus, J., 2006. The effect of early diagenesis on the Fe isotope compositions of porewaters and authigenic minerals in continental margin sediments. Cosmochim. Acta 70, 2006–2022.

Skulan, J.L., Beard, B.L., Johnson, C.M., 2002. Kinetic and equilibrium Fe isotope fractionation between aqueous Fe(III) and hematite. Geochim. Cosmochim. Acta 66, 2995–3015.

Tullborg, E-L., Smellie, J.A.T., MacKenzie, A.B., 2003. The use of natural uranium decay series studies in support of understanding redox conditions at potential radioactive waste disposal sites. MRS. Scientific basis for Nuclear Waste Management XXVII, vol. 807, pp. 571–576.

Urey, H.C., 1947. The thermodynamic properties of isotopic substances. J. Chem. Soc. Lond. 562–581.

Walker, J.R., 1993. Chlorite polytype geothermometry. Clays Clay Miner. 41, 260–267.

Welch, S.A., Beard, B.L., Johnson, C.M., Braterman, P.S., 2003. Kinetic and equilibrium Fe isotope fractionation between aqueous Fe(II) and Fe(III). Geochim. Cosmochim. Acta 67, 4231–4250.

Williams, H.M., McCammon, C.A., Peslier, A.H., Halliday, A.N., Teutsch, N., Levasseur, S., Burg, J-P., 2004. Iron isotope fractionation and the oxygen fugacity of the mantle. Science 304, 1656–1659.

Appendix 2

Natural Occurrences of Green Rust

B.C. Christiansen[1*], T. Balic-Zunic[2] and S.L.S. Stipp[1]

Submitted to Environmental Science & Technology 22. April 2008

Natural Occurrences of Green Rust

BO C. CHRISTIANSEN[1*], TONCI BALIC-ZUNIC[2] AND S.L. SVANE STIPP[1]

Nano-Science Center, Department of Chemistry, University of Copenhagen, Universitetsparken 5, DK-2100 Copenhagen Ø, Denmark, and Department of Geography and Geology, University of Copenhagen, Øster Voldgade 10, DK-1350 Copenhagen K, Denmark.

submitted to *Environmental Science and Technology*

Green rust, a group of Fe(II)/Fe(III) layered double hydroxides, are believed to be present in environments close to the Fe(II)-Fe(III) transition zone. Attempts to find and prove the existence of the minerals has proven difficult because the minerals oxidises quickly upon exposure to oxygen. In this work we show that by a simple sampling method it is possible to indentify GR. The method was applied to groundwaters of different origin, but both in the Fe(II)-Fe(III) transition system. By adding a droplet of solution to a piece of glass we used XRD and AFM to examine for the minerals. The solution composition was also used to test for the saturation index of the minerals. In all sampling areas GR_{Cl} and GR_{CO3} compounds were supersaturated. In this work we have found the presence of GR_{CO3} at 3 different sites.

Introduction

Layered double hydroxides (LDH) are a group of compounds which contain brucite-like hydroxide layers with metal sites occupied by both di- and trivalent cations. The surplus positive charge of the layers is compensated by additional anions, cations and water molecules which occupy the inter-layer space. Green rust, a family of layered double hydroxides (LDH), is easily synthezised under laboratory conditions. In it the metal layers contains Fe(II) and Fe(III). The first type of green rust which has been called GR-1, has spherical or planar anions e.g. Cl^- and CO_3^{2-} in the interlayer, whereas the second type, GR-2, has tetrahedral anions such as SO_4^{2-} that compensate the extra charge. The thermodynamic and oxidation-reduction properties, as they have been defined up to now, suggest that it should be a common mineral in soils and sediments [1-9]. However, it is very likely that its general occurrence in nature goes unnoticed because it oxidises to other minerals on contact with the atmosphere, before it can be verified by analysis. Green rust is known as an intermediate corrosion product when steel corrodes in reinforced concrete [10, 11], in sea water [7, 12, 13] and in water supply pipes [14]. One could also speculate that it is the active agent for redox processes in reactive barriers that rely on metal iron for groundwater remediation [15, 16].

Some occurrences of green rust have been documented in nature after careful sample handling. By collecting large block soil samples from hydromorphic soils in France and storing them under the original water solution from the sampling location, Trolard and colleagues [17-19] used transmission Mössbauer spectroscopy to show the presence of a mineral where iron was coordinated and bound in a similar way to iron in green rust carbonate. Koch and Mørup [20] described green rust in a Danish water treatment sludge that had reacted with decomposing organic matter. Recently, Bearcock et al. [21] used X-ray powder diffraction to identify a GR-1 compound with *c*-axis period of 23.697 Å in coal mine drainage sediment. However, these are reports of isolated observations. We lack documentation that green rust is a common and pervasive phase in all natural systems where groundwater Fe(II) is high and oxidation potential is low.

Knowing the extent of green rust occurrence in soil, sediment and groundwater is important for knowing if parameters describing its behaviour should be included in contaminant transport modelling. Synthetic and natural green rust observed to date have small particle size and therefore high surface area. This, together with its high reactivity both as an adsorbate and as a reducing agent (Table 1) suggests that it must be an important actor in the fate of toxic components in the environment, if it is generally common.

The two types can be distinguished using Mössbauer spectroscopy and X-ray diffraction. Using X-ray diffraction it is possible to measure the spacing

Table 1. Redox sensitive elements that have been investigated for reactivity with green rust. GR serves as an adsorbent or a reducing agent.

Reaction type	Component	Reference
Adsorption	As	[22, 23]
Redox reaction	Cr	[24-27]
	Ag, Au, Cu, Hg	[28]
	NO_2^-	[1, 29]
	NO_3^-	[2, 3, 30, 31]
	Se	[32, 33]
	Sb	[34]
	Organic compounds	[35-41]
	U	[42-44]
	Tc	[44, 45]

* corresponding author phone +45 2064 4023, e-mail Bochr@nano.ku.dk
[1] Department of Chemistry
[2] Department of Geography and Geology

Figure 1a) Bornholm (Well RL 264.761). The artesian well tube is about 0.5 m above water level. The oxidised iron red staining on the rocks reveals that dissolved Fe^{2+} in flowing groundwater is high (photo Kasper Bendsen); b) Äspö Tunnel in the SKB Hard Rock Laboratory near Oskarshamn (Borehole SA2273A). Groundwater flows directly out of a pipe into the fracture system in the granite. Again dissolved iron oxidises as it drips from the tap on the pipe, forming bright red deposits of iron oxide. Samples removed from inside the flowing pipes insures collection of reduced groundwater.

between the layers. This spacing depends on the size of the interlayer anion and therefore identifies the type of green rust. The use of Mössbauer spectroscopy to identify GR in soil or sediments is not definitive. Although Mössbauer spectroscopy identifies bonding environment and redox state of the Fe in the solid, neither the Fe bonding, nor the Fe(II)/Fe(III) ratio observed for green rust are unique or diagnostic. For example common soil minerals like chlorite and several Fe-bearing clay minerals exhibit the same Mössbauer parameters. The purpose of this article is to report on the discovery of green rust generally in groundwater environments where conditions are near the Fe(II)/Fe(III) redox boundary and to present a simple and reliable method for finding and identifying this elusive mineral.

Experimental Section

Sampling. Samples were collected from locations where groundwater is known to be at or near the Fe(II)/Fe(III) transition zone: from an artesian well in a chalk aquifer (Fig. 1a) and from Precambrian granite fractures in an underground tunnel (Fig. 1b). The artesian well (RL 246.761) is situated in an aquifer located near the town of Rønne on Bornholm, Denmark (Fig. 2a). The well was established soon after 2000. Its purpose was to vent the aquifer for excess dissolved nickel and iron.
During the 1990's, the water table had been lowered so much that pyrite began to oxidise in the Cenomanian chalk aquifer. When the water table moved up again, nickel and iron were released.

The samples from the fractures of Precambrian granites were taken at two sites in SKB's Hard Rock Laboratory at Äspö, Sweden, near Oskarshamn (Fig. 2b). Sampling sites in the tunnels are constructed so groundwater can be extracted directly from the fractures through a valve to prevent contact of the reducing groundwater with air.

One site (Fig. 1b) was ~ 320 m below surface (SA2273A) and the other site, in the MICROBE lab, was 450 m below surface (KJ0050F01). The Fe^{2+} and total iron ($Fe_{(tot)}$) contents in water were measured in the tunnel sample (SA2273A). A sample (30 ml) of groundwater was collected and 1 drop of conc. HCl was added immediately to limit oxidation of ferrous iron during transport to the laboratory for analysis. Fe^{2+} was determined on a spectrophotometer using the ferrozine method [46]. Total Fe was measured using atomic absorption spectrometry (AAS). The water compositions from the two other sites (RL 246.761 and KJ0050F01) were not directly analysed in this study. Monitoring reports provided full groundwater composition for all three sites [47-49]. The relevant data are summarised in Table 2.

Figure 2a. Map of RL 264.761 sampling site, indicated by the arrow. Map after Kort og Matrikelstyrelsen (National Survey and Cadastre).

Table 2. Concentrations for selected compounds from monitoring reports and own sampling for the groundwaters from the three sampling sites.

Site	pH	Fe^{2+} mg/l	Fe(tot) mg/l	HCO_3^- mg/l	Cl^- mg/l	SO_4^{2-} mg/l
RL 246.761[1]	6.2-6.4	n.a.	5.2-9.2	100-143	26.5-38.5	97-120
SA2273A[2]	n.a.	0.65	0.76	n.a.	n.a.	n.a.
SA2273A[3]	7.4	n.a.	0.803	159	3,770	264
KJ0050F01[4]	7.3-7.4	0.105-0.125	0.109-0.125	30-64	6,580-8,040	148-155

	Ca^{2+} mg/l	Na^+ mg/l	SI halite[5]	SI gypsum[5]	SI GR_{Cl}[5]	SI GR_{CO3}[5]	SI $GR_{Na,SO4}$[5]
RL 246.761[1]	69	16	-7.79	-1.49	4.70-5.30	2.58-3.44	-13.50 – -12.45
SA2273A[2]	n.a.	n.a.	n.a.	n.a.	n.a.	n.a.	n.a.
SA2273A[3]	670	1,500	-3.94	-0.84	7.97	5.01	-10.19
KJ0050F01[4]	1,890-2,540	2,260-2,520	-3.60 – - 3.48	-0.92 – -0.86	4.37 – 5.02	-0.92 – -0.05	-19.10 – -18.09

[1] range from 2002-2005 [49], [2] this study, [3] [50], [4] range from 2000-2003 [47], [5] Calculated by PhreeqC [51]
n.a = not analysed.

Figure 2b. Map of sampling site at Äspö, Sweden. Map after Google Maps.

A chronic problem with the identification of naturally occurring green rust is the risk of oxidation during sample collection and analysis. Sample stabilising methods, such as the application of glycerol [52], prevent oxidation, but have not yet been tested for their possible influence on the mineral properties, such as expansion of the interlayer. Collection of particulate material from groundwater is complicated by the time required for filtration and transfer of the filtered sample into the analytical chamber. We chose to experiment with a sample stabilised using a material that is omnipresent in nature and that would be quick and easy to use during sampling and analysis.

Silica has long been known to inhibit the transformation of Fe(III)-oxides [53] and silicates such as clay, quartz or feldspar are present in most of the geological settings. Studies by Hansen and colleagues show that green rust has a high affinity for dissolved silica [54] and very recently, Si was shown to stabilise the structure of GR_{SO4} [55]. Muscovite, a silicate mineral, and silica glass are available commercially as microscope slides and cover slips and serve as excellent analogues for natural mineral surfaces while providing a flat substrate suitable for analysis by atomic force microscopy (AFM) and X-ray powder diffraction (XRPD).

At the artesian well (RL 246.761), water was collected directly from the outlet pipe using a pipette. At Äspö, the water was allowed to flow for a minute to allow fresh groundwater from the fracture to reach the outlet before sampling.

Within 30 seconds of taking a water sample, a droplet covering approximately 1 cm^2 was deposited on the substrate (glass or mica) and covered with a platelet made of the same material. The sample was left for a minute for particles in the solution to adhere on the substrate plates and thereafter the liquid was sucked away with a tissue. A few tests were made with different settling times (1/2 minute to 5 minutes) between the addition of the suspension to the substrate and the removal of water, but no difference in composition of the adsorbed material was observed. So for practical purpose one minute was chosen.

Within five minutes of collecting the water from the outlets, the finished samples were stored under N_2. They were transported to the lab in nitrogen and then stored in an anaerobic glove box at room temperature. The glove box has an atmosphere of 96% N_2 and 4% H_2 and is equipped with palladium catalyst that removes O_2 by reduction to water with H_2. AFM imaging was performed in the glove box while X-ray powder diffraction (XRPD) analyses were made in air. Reproducibility tests made with test samples of synthetic GR showed that dry GR samples fixed on these Si-bearing substrates are stable in air for at least 24 hours.

A control solution (synthetic groundwater) was prepared resembling the groundwater of KJ0050F01 according to the concentrations of Na^+, Ca^{2+}, Cl^- and SO_4^{2-},

to make a sample we could use for oriented precipitation of gypsum and halite. It contained 0.03 M $CaCl_2 \cdot 2H_2O$ and 0.05 M Na_2SO_4. The same XRD sampling procedure was applied to produce these samples.

Analytical Techniques. Powder X-ray diffraction (XRD) is a common tool for identifying very fine-grained soil minerals. We used a Philips PW3710 Bragg-Brentano diffractometer, with a Cu tube, (characteristic wavelength, $\lambda = 1.5418$ Å), secondary graphite monochromator and a variable divergence slit. The generator was set at 40 kV and the current, at 40 mA. The secondary graphite monochromator eliminates the influence of Fe-fluorescence. Samples were analysed in air for periods ranging from 2 to 9 hours. Data were treated with the EVA software (DIFFRACplus evaluation package, 2007, Bruker AXS, Karlsruhe, Germany) and peaks were compared with our own synthetic standards and the powder diffraction files published by the International Centre for Diffraction Data (ICDD, 2007).

Atomic force microscopy (AFM) uses a sharp tip to sense the forces at the surface of a sample at local scale and produces images of morphology and structure with sub-Ångström resolution [56]. We used a Digital Instruments Nanoscope Multimode IIIa equipped with a piezoelectric scanner with 12 micrometer maximum range in the *x,y* plane and sharpened Si_3N_4 tips with a spring constant of about 0.12 N/m. Images presented here were taken in deflection and height contact modes, in the atmosphere of the glove box. Relative humidity was about 36%. Scanner curvature was removed by applying a low order polynomial fit to the flat substrate baseline in the DI software but images were not treated with filtering.

Results and Discussion

The Fe concentration of the groundwaters varies (Table 2) and is lowest in KJ0050F01 with 0.1 mg/L. In the tunnel (SA2273A), the concentration is ~ 0.8 mg/l and in the groundwater from RL 246.743, concentration ranges between 5.2 to 9.2 mg/l. In the deep samples, Cl^- concentration is very high (3,770-8,040 ppm), which is typical for the saline groundwaters originating from the Litorina Sea (7500-4000 BP) [48]. Sulphate concentration ranges from 97 to 264 mg/l and bicarbonate, from 30 to 159 mg/l. The shallow groundwater sample (RL 246.761) from the chalk aquifer, has the highest bicarbonate concentration. Thus all three water samples contain the ions necessary for green rust formation.

Although the structure and composition are not known precisely for the green rust forms expected in natural groundwater, some studies have proposed thermodynamic constants that can be used to estimate a saturation state for GR [57, 58]. Using the chemical composition of the waters with the PhreeqC geochemical speciation code [51] with the Minteq2 database [59], we could test if modelling would predict precipitation of GR. We used a log K of 9.1 for GR_{CO3} [57], log K of 10.37 for GR_{Cl} [58] and a log K of 32.6 for $GR_{Na,SO4}$ [60]. For the groundwater at the sites investigated, calculations show that the saturation index is higher than 0 for green rust chloride or carbonate indicating that precipitation is expected (Table 2). However, the mass of solid in the water is very low – far too low to allow capture on a filter or to be observable with the traditional particle counting techniques. We have been able, however, to confirm presence of green rust in all three groundwaters, by approaches commonly used in nano-science. By analysing for a long time on a flat sample, we could collect peaks of sufficient intensity to indentify the material adhered even though it was present as only a few discrete grains.

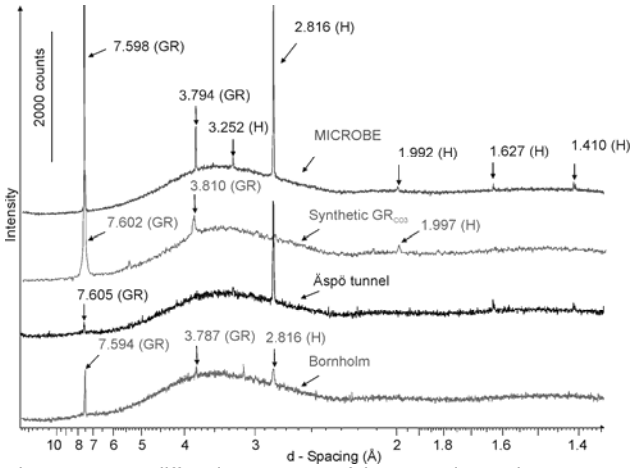

Figure 3. X-ray diffraction patterns of the natural samples, compared with a synthetic GR_{CO3} sample. The peaks representing the basal plane at d-spacing ~7.6 Å is characteristic for GR-1. H represents halite and GR represents green rust.

Figure 3 shows the XRPD patterns from the three samples prepared using groundwater, one from Rønne and two from Äspö. For comparison, a pattern of a synthetic GR_{CO3} is included. All of these were prepared on substrates of glass, which add a very broad diffraction maxima of which the largest hump at 3-5 Å can be recognised on all patterns. Glass is most suitable for mineralogical identification because it does not produce any sharp peaks of its own. The platy morphology of GR makes the crystals deposit with the basal plane parallel to the substrate surface (Fig. 4a). This preferential orientation makes it very easy to determine the layer spacing and thereby distinguish between GR-1 and GR-2 types and to distinguish them from all other possible minerals. In LDH, the interlayer anions can replace each other. The order of preference is: $CO_3^{2-} > SO_4^{2-} > Cl^-$ [61] but when the ratio of SO_4^{2-} to CO_3^{2-} is high, SO_4^{2-} dominates. This implies that in fresh waters, where CO_3^{2-} is abundant, one can expect a GR-1 type structure on XRD patterns whereas in saline water, SO_4^{2-} is abundant so GR-2 is formed, such as during the corrosion of steel in seawater [12].

The d-spacings of the XRPD patterns for the Bornholm sample (RL 246.761) deposited on glass (Fig. 3) and muscovite (not shown) both fit a GR-1 type structure. The chemical composition of the groundwater suggests that it is likely either the CO_3^{2-} or Cl^- form of green rust (Table 2). Additional peaks from halite (NaCl) are also

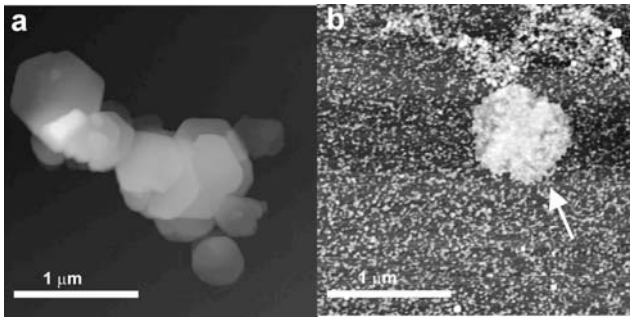

Figure 4. AFM height images of green rust: a) synthetic material on a muscovite (mica) substrate. Particles adhere on their basal plane. b) a muscovite substrate showing a green rust particle from the Bornholm sample. It is not as smooth and fine as synthetic particles, probably because other compounds in the water inhibit growth and it may have undergone several phases of growth and dissolution during its transport. The abundant small white particles are halite and gypsum, evaporated from the water.

observed, as in the reference sample. We used the presence of halite as an internal standard so when a sample was allowed to oxidise in air for several days, we could monitor decreased intensity of the green rust peaks compared to the stable intensity for halite. The halite peaks are also used to correct for 2-theta shift when the samples are not in plane with the focus of the XRD. With extended exposure to air, the samples gradually became reddish as expected when green rust oxidises and the basal plane peaks that represent GR-1 lost intensity (Fig. 5). XRD patterns of the synthetic groundwater (Figure 6) exhibits patterns of halite in both the fresh and the aged pattern. Gypsum only occurred when the sample had been exposed to the atmosphere for 14 days. This is consistent with recrystalisation of salts on surfaces exposed to the atmosphere [62]. Because the intensities of the peaks from the natural sample are decreasing opposite to what is seen in the synthetic groundwater sample, the presence of GR-1 compounds in the groundwater system is established. If there were clay minerals (eg. chlorite, smectite and kaolinite) one would expect the presence of basal plane peaks at app. 14 Å, we did not observe this, and furthermore the typical positions are at app. 7.0 Å or 8.0 Å for this type of minerals.

The crystal lattice parameters of GR_{Cl} and GR_{CO3} are not very different (Table 3), so it is not straight forward to determine whether the green rust phase is GR_{Cl} or GR_{CO3}. There is still considerable uncertainty in the structure and composition of these phases, and likewise, parameters published for them vary. Of course, the groundwater composition helps limit the possibilities. Anion exchange studies show that carbonate is by far the most preferred interlayer anion in LDH at ambient temperatures and pressure [61, 63, 64].

Figure 4b presents an AFM height image of one of the muscovite substrates prepared using groundwater from Bornholm (RL 246.761). It shows a tabular particle with a roughly hexagonal outline. Its thickness varies from ~3 to 7 nm. In a separate study of the stickiness of green rust on a series of mineral surfaces, Hansson and Stipp [65] showed that particles attach more readily to some

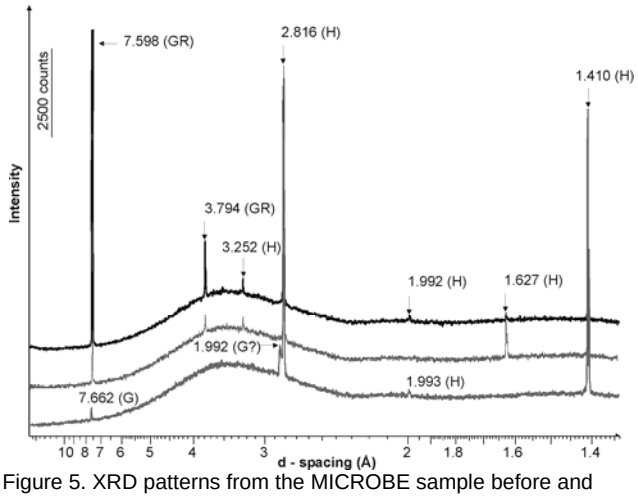

Figure 5. XRD patterns from the MICROBE sample before and after oxidation in air, compared to a sample made from salt test solutions (bottom). The fresh sample (top) shows clear peaks for GR which strongly diminish after oxidation in air for 14 days (middle). Other peaks on the diagrams are marked G for gypsum ($CaSO_4 \cdot 2H_2O$) and H for halite (NaCl).

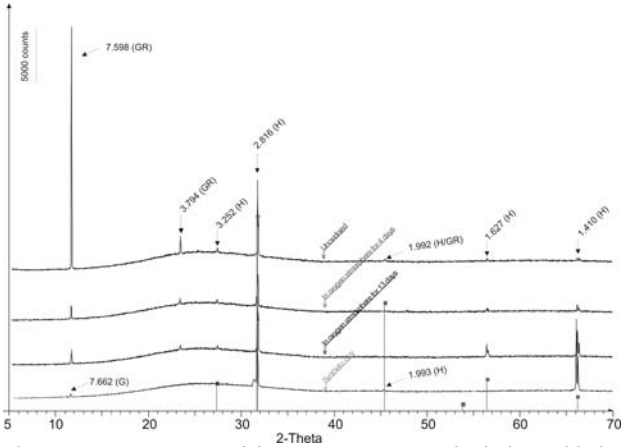

Figure 6. XRD patterns of the KJ0050F01 sample during oxidation. The GR peak decreases in intensity as a function of air exposure time. GR peaks decrease in intensity compared with the peaks representing halite (NaCl).

substrates than others but the crystal size and morphology are the same. Particles attached immediately when a GR suspension was deposited on the substrates. In other experiments of that study, green rust particles nucleated and grew directly on the substrate from a filtered solution but growth of micrometer-size particles took more than an hour and the morphology was different from that of suspension grown particles. It was influenced by the substrate. Thus we can say with certainty, that the colloidal particles of green rust that were trapped on the silicate-bearing substrates were already present in the groundwater when it was sampled. They could not have grown on the substrate in the minute or so used for their collection.

We have shown that by simple measures it is possible to test for the presence of GR in groundwater systems by XRPD and occasionally one can observe green rust directly as sub-micrometer particles. XRPD is more reliable for identification of GR than Mössbauer spectroscopy because it gives all information about the structural state of the material and easily records the

Table 3. Structural parameters for GR_{CO3} and GR_{Cl}.

GR type	*a*-axis (Å)	*c*-axis (Å)	Interlayer spacing (Å)	Ref.
GR_{CO3}	3.181	21.82	7.273	[63]
	3.16	22.45	7.483	[60]
	3.166	22.52	7.507	[64]
	-	22.59	7.53	[65]
	-	22.662	7.554	[66]
	3.17	22.8	7.6	[22]
	-	22.8	7.6	[67]
	3.16	23.61 (XRD) 22.54 (SAED)	7.870 (XRD) 7.513 (SAED)	[68]
	-	-	7.59-7.60	this work
GR_{Cl}	-	23.8	7.93	[69]
	3.19	23.85	7.95	[1]
	-	23.85	7.95	[65]
	3.198	24.2	8.07	[70]
	-	24.3	8.09	[71]

changes induced by the exposure to air. The fact that green rust disappears from the XRPD patterns as it oxidises is proof of GR presence.

Samples of synthetic green rust in the growth solution oxidise after about 30 minutes and dried samples need twice that long. The samples that were attached to glass and to mica, both silica-bearing substrates, did not oxidise during the 9 hours required to collect the XRPD patterns. Thus, attachment to silicate-bearing substrates slows GR oxidation. Absence of solution slows oxidation further. However after several days exposure to air, green rust did oxidise and the peaks decreased in intensity.

In these investigated sites the chemical analysis and XRPD suggest the predominance of GR_{CO3} which is consistent with the observed preference of CO_3^{2-} over Cl^- in LDH's [61]. Our findings demonstrate that GR should be included in transport modelling for groundwater systems. Because of the reactive nature of GR, its role in the retention/mobilisation of redox-sensitive elements in the groundwater, must be taken into account when one considers contaminant remediation in or near the Fe(II)-Fe(III) transition system.

Our new method allows for a more extensive investigation of GR presence in the natural environment. Sampling on silica-bearing substrates preserves GR from oxidation during the time needed to record XRD diagrams. Measurement of the characteristic crystal lattice parameters (e.g. the value of the basal spacing) allows for identification of the type of GR.

Acknowledgements

We thank Peer Jørgensen, Birgit Damgaard and Helene Almind for technical support, Kasper Bendsen for photos the NanoGeoScience group for discussion and especially Knud Dideriksen and Lone Skovbjerg for constructive comments. Karsten Pedersen, Göteborg University provided access to his Äspö MICROBE lab for water sample from his flow-through bioreactors and Eva-Lena Tullborg arranged access to the Hard Rock Lab tunnel and groundwater concentrations. We thank Eva-Lena Tullborg, John Smellie and Ignasi Puigdomenech for their interest and encouragement. This work was partly supported by Svensk Kärnbränslehantering AB (SKB) and by a grant from Danish Natural Science Research Council (FNU).

References

(1) Hansen, H. C. B.; Borggaard, O. K.; Sørensen, J., Evaluation of the free energy of formation of Fe(II)-Fe(III) hydroxide-sulphate (green rust) and its reduction of nitrite. *Geochimica et Cosmochimica Acta* **1994,** *58*, 2599-2608.

(2) Hansen, H. C. B.; Koch, C. B., Reduction of nitrate to ammonium by sulphate green rust; activation energy and reaction mechanism. *Clay Minerals* **1998,** *33*, 87-101.

(3) Hansen, H. C. B.; Koch, C. B.; Nancke-Krogh, H.; Borggaard, O. K.; Sørensen, J., Abiotic nitrate reduction to ammonium: Key role of green rust. *Environmental Science and Technology* **1996,** *30*, 2053-2056.

(4) Génin, J.-M. R.; Ruby, C.; Upadhyay, C., Structure and thermodynamics of ferrous, stoichiometric and ferric oxyhydroxycarbonate green rusts; redox flexibility and fougerite mineral. *Solid State Sciences* **2006,** *8*, (11), 1330-1343.

(5) Génin, J.-M. R.; Aissa, R.; Géhin, A.; Abdelmoula, M.; Benali, O.; Ernstsen, V.; Ona-Nguema, G.; Upadhyay, C.; Ruby, C., Fougerite and FeII-III hydroxycarbonate green rust; ordering, deprotonation and/or cation substitution; structure of hydrotalcite-like compounds and mythic ferrosic hydroxide Fe(OH)(2+x). *Solid State Sciences* **2005,** *7*, (5), 545-572.

(6) Génin, J.-M. R.; Bourriér, G.; Trolard, F.; Abdelmoula, M.; Jaffrezic, A.; Refait, P.; Maitre, V.; Herbillon, A., Thermodynamic Equilibria in Aqueous Suspensions of Synthetic and Natural Fe(II)-Fe(III) Green Rusts: Occurrences of the Mineral in Hydromorphic Soils. *Environmental Science and Technology* **1998,** *32*, (8), 1058-1068.

(7) Génin, J.-M. R.; Olowe, A. A.; Resiak, B.; Confente, M.; Rollet-Benbouzid, N.; L'Haridon, S.; Prieur, D., Products obtained by microbially-induced corrosion of steel in a marine environment: Role of green rust two. *Hyperfine Interactions* **1994,** *93*, 1807-1812.

(8) Génin, J.-M. R.; Refait, P.; Bourrié, G.; Abdelmoula, M.; Trolard, F., Structure and stability of the Fe(II)-Fe(III) green rust "fougerite" mineral and its potential for reducing pollutants in soil solutions. *Applied Geochemistry* **2001,** *16*, 559-570.

(9) Génin, J.-M. R.; Refait, P.; Olowe, A. A.; Abdelmoula, M.; Fall, I.; Drissi, S. H., Identification of Green Rust Compounds in the Aqueous Corrosion Processes of Steels; the Case of Microbially Induced Corrosion and Use of 78 K CEMS. *Hyperfine Interactions* **1998,** *112*, (1), 47-51.

(10) Refait, P.; Drissi, S. H.; Pytkiewicz, J.; Génin, J.-M. R., The anionic species competition in iron aqueous corrosion: Role of various green rust compounds. *Corrosion science* **1997,** *39*, (9), 1699-1710.
(11) Kounde, B.; Raharinaivo, A.; Olowe, A. A.; Rezel, D.; Bauer, P.; Génin, J.-M. R., Mössbauer characterization of the corrosion products of steel in civil works: Suspension bridge and reinforced concrete. *Hyperfine Interactions* **1989,** *46*, 421-428.
(12) Génin, J.-M. R.; Olowe, A. A.; Benbouzid-Rollet, N. D.; Prieur, D.; Confente, M.; Resiak, B., The simultaneous presence of green rust 2 and sulfate reducing bacteria in the corrosion of steel sheet piles in the harbour area. *Hyperfine Interactions* **1991,** *69*, 875-878.
(13) Rodríguez, J. J. S.; González, J. E. G., Identification and formation of green rust 2 as an atmospheric corrosion product of carbon steel in marine atmospheres. *Materials and Corrosion* **2006,** *57*, (5), 411-417.
(14) Stampfl, P. P., Ein Basisches Eisen-II-III-Karbonat in Rost. *Corrosion Science* **1969,** *9*, 185-187.
(15) Roh, Y.; Lee, S. Y.; Elless, M. P., Characterization of corrosion products in the permeable reactive barriers. *Environmental Geology* **2000,** *40*, (1-2), 184-194.
(16) Agrawal, A.; Ferguson, W. J.; Gardner, B. O.; Christ, J. A.; Bandstra, J. Z.; Tratnyek, P. G., Effects of Carbonate Species on the Kinetics of Dechlorination of 1,1,1-Trichloroethane by Zero-Valent Iron. *Environmental Science and Technology* **2002,** *36*, (20), 4326-4333.
(17) Trolard, F.; Génin, J.-M. R.; Abdelmoula, M.; Bourrié, G.; Humbert, B.; Herbillon, A., Identification of a green rust mineral in a reductomorphic soil by Mössbauer and Raman spectroscopies. *Geochimica et Cosmochimica Acta* **1997,** *61*, (5), 1107-1111.
(18) Trolard, F.; Bourrié, G., Influence of green rusts on oxido-reduction sequences in soils: L'influence des oxydes de fer de type « rouilles vertes » sur les séquences d'oxydo-réduction dans les sols. *Comptes Rendus de l'Academie des Sciences - Series IIA - Earth and Planetary Science* **1999,** *329*, (11), 801-806.
(19) Trolard, F.; Bourrié, G., Structure of fougerite and green rusts and a thermodynamic model for their stabilities. *Journal of Geochemical Exploration Extended Abstracts presented at the 7th Symp. on the Geochemistry of the Earth's Surface (GES-7)* **2006,** *88*, (1-3), 249-251.
(20) Koch, C. B.; Mørup, S., Identification of green rust in an ochre sludge. *Clay Minerals* **1991,** *26*, 577-582.
(21) Bearcock, J. M.; Perkins, W. T.; Dinelli, E.; Wade, S. C., Fe(II)/Fe(III) 'green rust' developed within ochreous coal mine drainage sediment in South Wales, UK. *Mineralogical Magazine* **2006,** *70*, 731-741.
(22) Lien, H.-L.; Wilkin, R. T., High-level arsenite removal from groundwater by zero-valent iron. *Chemosphere* **2005,** *59*, (3), 377-386.
(23) Randall, S. R.; Sherman, D. M.; Ragnarsdottir, K. V., Sorption of As(V) on green rust ($Fe_4(II)Fe_2(III)(OH)_{12}SO_4{\cdot}3H_2O$) and lepidocrocite (γ-FeOOH): Surface complexes from EXAFS spectroscopy. **2001,** *65*, 1015-1023.
(24) Skovbjerg, L. L.; Stipp, S. L. S.; Utsunomiya, S.; Ewing, R. C., The mechanisms of reduction of hexavalent chromium by green rust sodium sulphate: Formation of Cr-goethite. *Geochimica et Cosmochimica Acta* **2006,** *70*, (14), 3582-3592.
(25) Loyaux-Lawniczak, S.; Refait, P.; Ehrhardt, J. J.; Lecomte, P.; Génin, J.-M. R., Trapping of Cr by formation of ferrihydrite during the reduction of chromate ions by Fe(II)-Fe(III) hydroxysalt green rusts. *Environmental Science and Technology* **2000,** *34*, 438-443.
(26) Legrand, L.; Figuigui, A. E.; Mercier, F.; Chaussé, A., Reduction of Aqueous Chromate by Fe(II)/Fe(III) Carbonate Green Rust: Kinetic and Mechanistic Studies. *Environmental Science and Technology* **2004,** *38*, 4587-4595.
(27) Williams, A. G. B.; Scherer, M. M., Kinetics of the Cr(VI) reduction by carbonate green rust. *Environmental Science and Technology* **2001,** *35*, 3488-3494.
(28) O'Loughlin, E. J.; Kelly, S. D.; Kemner, K. M.; Csencsits, R.; Cook, R. E., Reduction of Ag^{I}, Au^{III}, Cu^{II} and Hg^{II} by Fe^{II}/Fe^{III} hydroxysulfate green rust. *Chemosphere* **2003,** *53*, 437-446.
(29) Dhouibi, L.; Refait, P.; Triki, E.; GÃ©nin, J.-M. R., Interactions between nitrites and Fe(II)-containing phases during corrosion of iron in concrete-simulating electrolytes. *Journal of Materials Science* **2006,** *V41*, (15), 4928-4936.
(30) Hansen, H. C. B.; Guldberg, S.; Erbs, M.; Koch, C. B., Kinetics of nitrate reduction by green rusts - effects of interlayer anion and Fe(II):Fe(III) ratio. *Applied clay science* **2001,** *18*, 81-91.
(31) Bender Koch, C. a. H., H.C.B., Reduction of Nitrate to Ammonium by Sulphated Green Rust. **1997,** *30*, 373-393.
(32) Myneni, S. C. B.; Tokunaga, T. K.; Brown Jr., G. E., Abiotic selenium redox transformations in the presence of Fe(II,III) oxides. *Science* **1997,** *278*, 1106-1109.
(33) Johnson, T. M.; Bullen, T. D., Selenium isotope fractionation during reduction by Fe(II)-Fe(III) hydroxide-sulfate (green rust). *Geochimica et Cosmochimica Acta* **2003,** *67*, 413-419.
(34) Mitsunobu, S.; Takahashi, Y.; Sakai, Y., Abiotic reduction of antimony(V) by green rust ($Fe_4(II)Fe_2(III)(OH)_{12}SO_4 \cdot H_2O$). *Chemosphere* **2008,** *70*, (5), 942-947.
(35) Maithreepala, R. A.; Doong, R.-A., Enhanced Dechlorination of Chlorinated Methanes and Ethenes by Chloride Green Rust in the Presence of Copper(II). *Environmental Science & Technology* **2005,** *39*, (11), 4082-4090.
(36) Lee, W.; Batchelor, B., Reductive Capacity of Natural Reductants. *Environmental Science and Technology* **2003,** *37*, (3), 535-541.
(37) O'Loughlin, E. J.; Burris, D. R., Reduction of halogenated ethanes by green rust. *Environmental Toxicology and Chemistry* **2004,** *23*, (1), 41-48.
(38) Elsner, M.; Schwarzenbach, R. P.; Haderlein, S. B., Reactivity of Fe(II)-Bearing Minerals toward Reductive Transformation of Organic Contaminants. *Environmental Science and Technology* **2004,** *38*, (3), 799-807.
(39) Roh, Y.; Lee, S. Y.; Elless, M. P., Characterisation of corrosion products in the permeable reactive barriers. *Environmental Geology* **2000,** *40*, 184-194.
(40) Lee, W.; Batchelor, B., Abiotic Reductive Dechlorination of Chlorinated Ethylenes by Iron-Bearing Soil Minerals. 2. Green Rust. *Environmental Science and Technology* **2002,** *36*, (24), 5348-5354.
(41) Maithreepala, R. A.; Doong, R.-A., Synergistic Effect of Copper Ion on the Reductive Dechlorination of Carbon Tetrachloride by Surface-Bound Fe(II) Associated with Goethite. *Environmental Science & Technology* **2004,** *38*, (1), 260-268.
(42) Dodge, C. J.; Francis, A. J.; Gillow, J. B.; Halada, G. P.; Eng, C.; Clayton, C. R., Association of Uranium with

Iron Oxides Typically Formed on Corroding Steel Surfaces. *Environmental Science and Technology* **2003,** *36*, 3504-3511.

(43) O'Loughlin, E. J.; Kelly, S. D.; Cook, R. E.; Csencsits, R.; Kemner, K. M., Reduction of Uranium(VI) by Mixed Iron(II)/Iron(III) Hydroxide (Green Rust): Formation of UO2 Nanoparticles. *Environmental Science and Technology* **2003,** *37*, 721-727.

(44) Roh, Y.; Lee, S. Y.; Elless, M. P.; Foss, J. E., Incorporation of radioactive contaminants into pyroaurite-like phases by electrochemical synthesis. *Clays and Clay Minerals* **2000,** *48*, 266-271.

(45) Pepper, S. A.; Bunker, D. J.; Bryan, N. D.; Livens, F. R.; Charnock, J. M.; Pattrick, R. A. D.; Collison, D., Treatment of radioactive wastes: An X-ray absorption spectroscopy study of the reaction of technetium with green rust. *Journal of Colloid and Interface Science* **2003,** *268*, 408-412.

(46) Gibbs, C. R., Characterization and application of FerroZine iron reagent as a ferrous iron indicator. *Anal. Chem.* **1976,** *48*, (8), 1197-1201.

(47) Pedersen, K. *The MICROBE framework. Site descriptions, instrumentation and characterisation.*; IPR-05-05; Svensk Kärnbränslehantering AB: Stockholm, February 2005, 2005; p 85.

(48) Laaksoharju, M.; Tullborg, E.-L.; Wikberg, P.; Wallin, B.; Smellie, J., Hydrogeochemical conditions and evolution at the Aspo HRL, Sweden. *Applied Geochemistry* **1999,** *14*, (7), 835-859.

(49) GEUS JUPITER - Hydrogeologisk database. http://arcims.mim.dk/website/geus/dk/DB/JUPITER/viewer.htm

(50) Laaksoharju, M.; Wold, S. *The colloid investigations conducted at the Äspö Hard Rock Laboratory during 2000-2004*; TR-05-20; Svensk Kärnbränslehantering AB: Stockholm, December 2005, 2005; p 211.

(51) Parkhurst, D. L.; Appelo, C. A. J. *User's guide to PHREEQC (version 2) - a computer program for speciation, batch-reaction, one-dimensional transport, and inverse geochemical calculations.*, U.S. Geological Survey: Denver, 1999.

(52) Hansen, H. C. B., Composition, stabilization, and light absorption of Fe(II)Fe(III) hydroxy-carbonate (green rust). *Clay Minerals* **1989,** *24*, 663-669.

(53) Cornell, R. M.; Schwertmann, U., The Iron Oxides. Structure, Properties, Reactions, Occurences and Uses. *VCH Weinheim* **1996**.

(54) Hendriksen, P. T.; Hansen, H. C. B., The effect of orthosilicate on the reactivity of iron(II)iron(III)hydroxide chloride (green rust). In *Internat. workshop Biogeochemical processes involving iron minerals in natural waters*, Monte Verita, Switzerland., 2003.

(55) Kwon, S.-K.; Kimijima, K.; Kanie, K.; Suzuki, S.; Muramatsu, A.; Saito, M.; Shinoda, K.; Waseda, Y., Influence of silicate ions on the formation of goethite from green rust in aqueous solution. *Corrosion Science* **2007,** *49*, (7), 2946-2961.

(56) Eggleston, C. M., High-Resolution Scanning Probe Microscopy: Tip-Surface Interaction, Artefacts, and Application in Mineralogy and Geochemistry. *In: CMS Workshop Lectures volume 7. Scanning Probe Microscopy of Clay Minerals (Eds. Nagy, K.L. and Blum, A.E.) Clay Mineral Society, Aurora, CO, USA* **1994**, jan-90.

(57) Drissi, H.; Refait, P.; Abdelmoula, M.; Génin, J.-M. R., The preparation and thermodynamic properties of Fe(II)-Fe(III) hydroxide-carbonate (Green Rust 1); Pourbaix diagram of iron in carbonate-containing aqueous media. *Corrosion Science* **1995,** *37*, 2025-2041.

(58) Refait, P.; Génin, J.-M. R., The oxidation of ferrous hydroxide in chloride-containing aqueous media and Pourbaix diagrams of green rust one. *Corrosion Science* **1993,** *34*, (5), 797-819.

(59) Allison, J. D.; Brown, D. S.; Novo-Gradac, K. J. *MINTEQA2/PRODEFA2—A Geochemical Assessment Model for Environmental Systems: Version 3.0 User's Manual.*, U.S. Environmental Protection Agency.: Athens, Georgia, 1990.

(60) Davesne, E.; Dideriksen, K.; Christiansen, B. C.; Ayala-Luis, K. B.; Koch, C. B.; Hansen, H. C. B.; Stipp, S. L. S., Determination of the free energy of formation of sodium- and sulphate-containing green rust (Na-Fe(II)-Fe(III) hydroxide-sulphate). *Geochimica et Cosmochimica Acta* **In preparation**.

(61) Miyata, S., Anion-exchange properties of hydrotalcite-like compounds. *Clays and Clay Minerals* **1983,** *31*, 305-311.

(62) Stipp, S. L. S.; Gutmannsbauer, W.; Lehmann, T., The dynamic nature of calcite surfaces in air. *American Mineralogist* **1996,** *81*, 1-8.

(63) Bontchev, R. P.; Liu, S.; Krumhansl, J. L.; Voigt, J.; Nenoff, T. M., Synthesis, Characterization, and Ion Exchange Properties of Hydrotalcite $Mg_6Al_2(OH)_{16}(A)_x(A')_{2-x}\cdot 4H_2O$ (A, A' = Cl^-, Br^-, I^-, and NO_3^-, $2 \geq x \geq 0$) Derivatives. *Chemistry of Materials* **2003,** *15*, 3669-3675.

(64) Mendiboure, A.; Schöllhorn, R., Formation and anion exchange reactions of layered transition metal hydroxides. *Revue de Chimie Minérale* **1986,** *23*, 819-827.

(65) Hansson, E.; Stipp, S. L. S., Colloidal green rust behaviour: Adhesion, transformation and mobility. **In preparation**.

Appendix 3

Composition and structure of an iron-bearing, layered double hydroxide (LDH) – Green rust sodium sulphate

Bo C. Christiansen[1,2], Tonci Balic-Zunic[2], Pierre-Olivier Petit[3,2], Cathrine Frandsen[4], Steen Mørup[4], Horst Geckeis[5], Anna Katerinopoulou[2] and S.L. Svane Stipp[1,2]*

Submitted to Geochimica et Cosmochimica Acta 16. May 2008

Composition and structure of an iron-bearing, layered double hydroxide (LDH) – Green rust sodium sulphate

Bo C. Christiansen[a*], Tonci Balic-Zunic[b], Pierre-Olivier Petit[c,b], Cathrine Frandsen[d], Steen Mørup[d], Horst Geckeis[e], Anna Katerinopoulou[b], S.L. Svane Stipp[a]

[a] *Nano-Science Center, Department of Chemistry, University of Copenhagen, Universitetsparken 5, DK-2100 København Ø, Denmark*

[b] *Department of Geography and Geology, University of Copenhagen. Øster Voldgade 10, DK-1350 Copenhagen K, Denmark*

[c] *LCMCP, UMR-CNRS 7574, L'Ecole Nationale Supérieure de Chimie de Paris (ENSCP), 11 Rue Pierre et Marie Curie, 75231 Paris Cedex 05, France*

[d] *Department of Physics, Bldg. 307, Technical University of Denmark, DK-2800 Kongens Lyngby, Denmark*

[e] *Institute for Nuclear Waste Disposal, Forschungszentrum Karlsruhe, Postfach 3640, D-76021 Karlsruhe, Germany*

submitted to *Geochemica et Cosmochimica*

Abstract

Mixed-valent Fe(II),Fe(III)-layered hydroxide, known as green rust, was synthesized from slightly basic, sodium sulphate solution in an oxygen-free glove box. Solution conditions were monitored with pH and Eh electrodes and optimized to ensure a pure sulphate green-rust phase. The solid was characterised using Mössbauer spectroscopy, X-ray diffraction, scanning electron microscopy and atomic force microscopy. Composition of the solution from which the green rust precipitated was established by mass and absorption spectroscopy. Green rust sulphate is composed of brucite-like layers with Fe(II) and Fe(III) in an ordered distribution. The inter-layers contain sulphate, water and sodium in an arrangement characteristic for the nikischerite-group. The crystal structure is highly disordered by stacking faults. The composition, formula and crystallographic parameters are: $NaFe(II)_6Fe(III)_3(SO_4)_2(OH)_{18}\cdot 12H_2O$, space group P-3, a = 9.528(6) Å, c = 10.968(8) Å and Z = 1. Green rust sodium sulphate, $GR_{Na,SO4}$, crystallizes in thin, hexagonal plates. Particles range from less than 50 nanometers to 2 micrometers in diameter and are 40 nm thick or less. The material is semi-conducting, with easy electron transfer along and across layers, so redox activity is high and reaction rates are fast. Extremely small particle size and high surface area contribute to rapid oxidation, transforming green rust to an Fe(III)-phase within minutes.

1. INTRODUCTION

Iron is present in nearly all natural environments. The dissolved species and solid phases that are favoured depend on redox conditions. Where oxygen partial pressure is low, iron is present as water soluble Fe(II)-species. Under ambient conditions, where oxygen is present, Fe(III) precipitates as iron-oxy(hydr)oxide phases. At the iron redox boundary, mixed-valent Fe(II),Fe(III)-compounds form, such as magnetite ($Fe(II)Fe(III)_2O_4$) and green rust. Green rust (GR) is the generic name for a family of compounds consisting of brucite-like layers of Fe(II),Fe(III)-hydroxide and is a member of the layered double hydroxide (LDH) group, also known as hydrotalcite-like compounds. Previous studies have reported structurally bound water and anions in the interlayer (SIMON et al., 2003). Until now, the thickness of the interlayer has been assumed to be defined by the intercalated anion. Compounds containing spherical or planar anions, such as Cl or CO_3, produce similar X-ray diffraction (XRD) patterns and as a group they have been known as GR1. The tetrahedral anions, such as SO_4, produce larger basal-plane spacing; this group has been known as GR2

The first LDH to be described, hydrotalcite ($Mg_6Al_2(OH)_{16}CO_3\cdot 4H_2O$), was reported in 1842 from Snarum, Norway (CARL, 1842). Several other LDH minerals have been identified and described (ALLMANN, 1968; AMINOFF and BROOMÉ, 1930) and the first report of synthetic compounds was made in 1967 (GASTUCHE et al., 1967). All those solids, both natural and synthetic, had Cl or CO_3 as interlayer ions. Miyata (1983) reported the first

* corresponding author:
Email address: bochr@nano.ku.dk

synthetic LDH-SO_4 compounds. Bernal and colleagues in 1959 and described it as hexagonal, with space group R-3 and cell parameters: a = 3.178 Å and c = 10.94 Å. Hansen et al. (1994a) assumed a unit cell with three times larger c period. They note that Arden (1950) had already synthesised this compound in 1950, but no details were reported about its composition, structure or relationship with other layered minerals. Already in 1927, Deiss and Schikkorr (1927) described experiments which probably lead to the synthesis of GR compounds, but details about the nature of the products are lacking. Although several research groups have investigated green rust sulphate and Fe-LDH compounds that contain other anions (BRINDLEY and BISH, 1976; DRISSI et al., 1994; GÉNIN et al., 2001; MCGILL et al., 1976a; MCGILL et al., 1976b; SIMON et al., 2003; TROLARD and BOURRIÉ, 2006), only once (HANSEN et al., 1994a) has it been suggested that the accepted structural description might be incomplete. Based on the work of Drits et al. (1987), Hansen and colleagues (1994a) suggested that Na might also be a part of the structure. Drits et al. (1987) had examined ocean floor sediments and reported a sodium-containing LDH with the composition $Mg_{3.96}Al_{1.98}Fe(III)_{0.06}(OH)_{12}[Na_{0.56}(SO_4)_{1.30}]\cdot 7.3H_2O$, which is reminiscent of GR_{SO4}. Recently, two sodium and sulphate-bearing, hydrotalcite-like minerals have been reported with full structural details: shigaite, $NaMn(II)_6Al_3(SO_4)_2(OH)_{18}\cdot 12H_2O$ and nikischerite, $NaFe(II)_6Al_3(SO_4)_2(OH)_{18}\cdot 12H_2O$ (COOPER and HAWTHORNE, 1996; HUMINICKI and HAWTHORNE, 2003).

The crystal size and reactivity of green rust make it a challenge to study. The maximum crystal size of only few micrometers prevents single-crystal structure analysis and the solid oxidises after only a few minutes exposure to air. When in contact with air or another oxidising agent, GR transforms to magnetite, goethite (α-FeOOH), lepidocrocite (γ-FeOOH) or ferrihydrite ($5Fe_2O_3\cdot 9H_2O$). The end product that is favoured depends on experimental conditions. For characterisation, one has three choices: i) to ensure that analyses are made in the absence of an oxidising agent; ii) to treat the samples so as to decrease their reactivity; or iii) to accept oxidation and attempt to correct the data afterwards. With this last option, the X-ray pattern is compounded by extra transition product peaks, so it is possible to overlook some significant green rust reflections. To inhibit oxidation, GR has often been stabilised with glycerol (HANSEN, 1989), which works well for the confirmation of GR presence, but glycerol treatment changes the interlayer spacing in LDH-SO_4 compounds (BISH, 1980; DRITS et al., 1987) and enhances preferred orientation of the powder (HANSEN, 1989) complicating an accurate structural determination. In this work, we aimed at the first method.

A recent paper by Simon and colleagues (SIMON et al., 2003) reports new XRD data for GR_{SO4} and proposes a structure based on Rietveld refinement. The material was produced by reacting ferrous hydroxide (formed from ferrous chloride and sodium hydroxide) mixed with sodium sulphate in open air while stirring. After synthesis, the material was sealed in capillaries to avoid further oxidation during XRD analyses. Some of the observed small peaks were interpreted as contamination and omitted from data analysis. The lattice parameters were reported (1959) reported a sulphate intercalated green rust, GR_{SO4}, as: a = 5.524 Å and c = 11.011 Å, space group P-31m or, in some parts of the paper, P-3m1, which we interpret to be a misprint. The authors determined the number of water molecules to be 8.5 per formula unit, using differential scanning calorimetry, but they chose to adopt the composition previously reported (HANSEN et al., 1994a), namely, $Fe(II)_4Fe(III)_2(SO_4)(OH)_{12}\cdot 8H_2O$, which reflects the ideal crystal structure derived from their Rietveld refinement. Although the structural model gave a fair fit to the experimental data, it does not explain all the observed reflections and, moreover, it contains an orientation of sulphate groups that is not consistent with results from similar hydrotalcite minerals (DRITS et al., 1987).

Reliable structure and composition data are critical for studies of GR reactivity with natural contaminants and for determining the thermodynamic constants that are essential in databases intended for predictive modelling, such as for example, in environmental risk assessment and developing methods for inhibiting corrosion. Our investigation was designed to fill this gap. Our goals were: i) to develop a method for producing green rust under stringent, anoxic conditions, in solutions without the addition of buffers or stabilising agents that could modify the compound; ii) to prepare samples for analysis in sample holders that would prevent oxidation during the measurement; iii) to determine reliable chemical and structural parameters of GR_{SO4} by X-ray powder diffraction aided by some spectrometric methods; and iv) to investigate the morphology and surface structure of GR nanoparticles by high resolution microscopy.

We chose to base our structural model on the analogous, non-redox active, mixed cation LDH compounds, for which reliable crystal structures have been published. The LDH family includes a range of phases where only one of the hydroxide layer cations is a transition metal, e.g. Mg-Cr(III), Mn(II)-Al, Fe(II)-Al, and Ni(II)-Al (BISH, 1978; EL MALKI et al., 1989; ENNADI et al., 1994; HANSEN et al., 1994b; KHALDI et al., 1997). Among these, the two sulphate compounds, nikischerite, $NaFe(II)_6Al_3(SO_4)_2(OH)_{18}\cdot 12H_2O$ (HUMINICKI and HAWTHORNE, 2003) and shigaite $NaAl_3Mn(II)_6(SO_4)_2(OH)_{18}\cdot 12H_2O$ (COOPER and HAWTHORNE, 1996), are particularly interesting, because of their similarities in composition with green rust. The possible presence of a monovalent cation in the GR interlayer has not previously been considered in the construction of a green rust structural model but its essential position in the structures of nikischerite and shigaite makes it an obvious place to start. These two minerals share all other features of the previously published models for GR2. The assumption of an essential interlayer monovalent cation was further supported by experimental observations. When SO_4 -bearing LDH compounds of Zn-Cr and Cu-Cr were washed with Na-SO_4-containing solutions, no change in basal plane spacing was recorded. When the compounds were rinsed with Li-SO_4 or NH_4-SO_4 solutions, the basal plane spacing decreased from 11.1 Å to 8.9 Å, suggesting removal of alkali ions from the interlayer (EL MALKI et al., 1989; KHALDI et al., 1997). If GR was washed with K-SO_4-containing solutions, the basal plane distance increased

from 11.1 Å to 11.3 Å. Thus interlayer thickness is a direct function of the solution composition and presumably, the interlayer exchanges to be at equilibrium with it. Khaldi (1997) showed that GR structure collapsed to 8.9 Å after storing the alkali metal-depleted compound for a week at 50% relative humidity, whereas the basal spacing of the initial, unrinsed material decreased only slightly during exposure to humidity ranging from 20 to 100%. This indicates that water more easily leaves the interlayer if the structural ions are washed out.

2. EXPERIMENTAL DETAILS

2.1 Green rust synthesis

Green rust was synthesised and samples prepared inside an oxygen-free glove box. The soft-walled, PVC chamber, supplied by Coy Laboratory Products, has a slightly over-pressured anaerobic chamber and a fast-entry chamber to allow exchange of samples and equipment without venting the entire volume. The entry chamber is a steel box with Plexiglas doors designed to hold low vacuum (10^{-3} to 10^{-4} bar). After placing the sample into the entry chamber, the door is sealed, and the chamber is evacuated to approximately 2.5 x 10^{-3} bars three times; after each of the first two evacuations, the chamber is refilled with 99.9990% nitrogen and after the last evacuation, with a mixture of 4% H_2 and 96% N_2. Even with this procedure, about 7500 ppm residual oxygen remains in the fast-entry chamber, resulting in accumulated contamination of as much as 200 ppm O_2 in the main chamber (COY-LABORATORY, 2002). In addition, about 0.5-1.0 ppm O_2 min^{-1} diffuses through the slightly permeable PVC membrane (COY, 2002). To keep O_2 levels below the 20 ppm detection limit, the chamber gas is constantly blown through palladium pellet filters, which catalyse the reaction of H_2 with O_2. An additional filter of alumina absorbs the resulting water. When pressure sensitive equipment, such as the atomic force microscope (AFM), is transferred into the chamber, the vacuum part of the purging cycle is omitted, and additional oxygen enters. During such operations, all redox-sensitive samples stored in the glove-box are closed in gas-tight bottles, and the whole chamber is evacuated and refilled with the $H_2 + N_2$ gas mix. The time for O_2 to decrease below the detection level averages about 15 minutes.

GR was synthesised in 300 ml PFA (perfluoroalkoxy) jars using doubly-deionised (MilliQ) water (< 0.1 µS/cm). We used a plastic pH electrode and solutions were made and stored in plastic or PFA, whenever possible. Contact with glass was minimised to avoid dissolved Si, which has been shown to be sorbed by green rust, considerably reducing its reactivity(KWON et al., 2007) and probably affecting its structure. All PFA-ware was washed outside the glove box, using standard laboratory methods. Iron-oxide and oxyhydroxide on the lab ware from previous experiments were first removed by soaking for 24 hours in 20% HCl. Remaining Cl was removed by soaking overnight in 10% HNO_3. Finally, the vessels were rinsed 5 times with MilliQ deionised water and allowed to air dry bottom-up. The doubly-deionised water for making solutions under controlled atmosphere was bubbled with N_2 (99.999%) for 3 hours prior to transfer into the glove box.

For green rust synthesis, we used 0.200 L stirred solutions of 0.05 M $FeSO_4 \cdot 7H_2O$ (melanterite p.a. grade). Base was added to produce an Fe/OH ratio of 0.6. This required a final concentration of 0.83 M NaOH (p.a. grade) added as pellets, which quickly dissolved in the ferrous solution. Addition of base to the Fe(II) solution caused precipitation of $Fe(II)(OH)_{2(s)}$, often called white rust, which remained in suspension; pH was about 8.4. Conversion to green rust began when oxygen was added by slowly pumping air into the vessel using a peristaltic pump. The air was first purged of CO_2, to avoid formation of GR_{CO3}, by bubbling it through 1 M NaOH. Thereafter the air was cleaned of NaOH in the gas phase and humidified by bubbling through pure water. Air flow was controlled at 19.5 +/- 2 ml/min using a flow meter. $Fe(OH)_{2(s)}$ transformation to GR was monitored using pH and Eh electrodes. The desired end-point for GR precipitation at the start of the pH drop was verified by the XRD and AFM data. $Fe(OH)_{2(s)}$ conversion to GR was complete after about 20 minutes. A batch produces approximately 13 g of GR.

2.2 Preparation of samples for analysis

For analyses which require dry samples, the solid was separated from solution using a centrifuge inside the glove box, spun at 14 000 rcf for 10 min. The supernatant was decanted, the small amount of remaining solution was sucked away with the corner of a tissue, and the sample was left in the centrifuge tube to dry. These samples (~ 20 mg) took about 24 hours to dry. They were subsequently pulverised in an agate mortar.

The dried material was sealed in oxygen-tight sample holders. Some of the samples investigated by powder XRD were inserted dry into capillaries made of quartz-glass (internal diameter, ø = 0.4 mm, glass wall thickness, t = 0.01 mm) which were sealed by dipping the open end into melted paraffin. However, the best powder diffraction diagrams, with the sharpest peaks, were obtained from larger samples deposited on vacuum grease smeared on a zero-background quartz plate that was fastened into a sample holder for Bragg-Brentano reflection. The whole assembly was sealed with a disk cut from 0.006 mm thick biaxially oriented polyethylene terephthalate film (Mylar®), held in place with vacuum grease. Test XRD patterns made as a function of time showed no visible signs of transformation in samples that had been out of the glove box for 24 hours, which gave enough time for the XRD measurement.

For transmission Mössbauer spectroscopy, larger samples were diluted by mixing with dry silica gel, mounted in closed Plexiglass holders and stored under liquid nitrogen for transport.

Atomic force microscopy (AFM) samples were examined inside the glove box. They were prepared from a few millilitres of unfiltered suspension removed from the reaction vessel using a plastic pipette. A drop of suspension was placed on a piece of freshly cleaved mica and left to settle for about 30 s, to allow time for the particles to adhere. The substrate was squirted with a quick

jet of MilliQ water to remove loose material. Excess water was sucked away with the corner of a tissue held to one side of the droplet, to avoid precipitation of salts. The substrate was attached to a steel sample disk with double-sided tape and left to dry on top of a fan box for at least half an hour.

For determination of composition, the GR was dissolved and analysed. We used inductively coupled plasma atomic emission spectroscopy (ICP-AES) and atomic absorption spectroscopy (AAS). The aim was to determine the mole ratio of Fe:S:Na in the GR. For defining the ratio, it was not important whether Fe was present as Fe(II) or Fe(III). Because mole ratios do not depend on sample mass or its change with loss or addition of water or oxygen, no precautions were taken to protect against oxidation. Samples were centrifuged for 10 min at 14 000 rcf, the solid was left to dry, transported to the ICP-AES facility, dissolved in 6 M HCl and analysed. A small amount of supernatant always remains with the solid even after centrifugation, so chemical analyses were also performed using the same methods on 2 mL of the supernatant. This allowed us to subtract what might have precipitated from the adsorbed liquid. Measured concentrations are presented in Table 1.

Table 1. Chemical composition.

Sample		1	2
Mass	wet (mg)	37	44
	dry (mg)	10	12
Mass of adsorbed supernatant (mg)		27	32
Fe	total in sample (mg)	3.857	4.072
	from supernatant (mg)	0.002	0.002
	from GR (mg)	3.855	4.070
	from GR (mmoles)	0.06903	0.0729
Na	total in sample (mg)	0.232	0.260
	from supernatant (mg)	0.048	0.047
	from GR (mg)	0.183	0.212
	from GR (mmoles)	0.00797	0.00878
S	total in sample (mg)	0.5355	0.5662
	from supernatant (mg)	0.0363	0.0359
	from GR (mg)	0.4992	0.5303
	from GR (mmoles)	0.01556	0.01630

2.3 Instrument parameters

X-ray diffraction patterns were collected from samples sealed in capillaries on a BrukerAXS Smart diffractometer equipped with a CCD detector (6.5x6.5 cm and 512x512 pixel active detector area) using a $Mo_{K\alpha}$ source ($\lambda = 0.7093$ Å), with a graphite monochromator and a 0.5 mm collimator. The detector was placed 12 cm from the sample, with two different detector settings, each for 15 min., with angular range up to 45° 2θ (*i.e.* down to 0.93 Å). Positions of diffraction rings were calibrated against an external quartz standard.

Powder X-ray diffraction patterns on larger samples that had been covered with Mylar foil were obtained using a Philips (now Panalytical) PW1730 powder diffractometer with the focusing Bragg-Brentano geometry, which ensures high resolution. We used a $Cu_{K\alpha}$ source ($\lambda = 1.5418$ Å) with a secondary-beam graphite monochromator, which effectively removes the other wavelengths from the X-ray spectrum and, most important, screens out significant fluorescence radiation from Fe, induced by $Cu_{K\alpha}$ radiation. A variable divergence slit for the primary beam ensures a constant sample illumination at all angles above 10° 2θ. Diffraction patterns were collected from 2° to 110° 2θ.

Mössbauer spectra were obtained using a constant acceleration spectrometer with a ^{57}Co source in a rhodium matrix. The spectrometer was calibrated with an α-Fe foil at room temperature and spectra of the GR sample were obtained at 80 K and 20 K. The sample was measured under vacuum ($< 10^{-2}$ mbar) for about 20 hours per spectrum.

For atomic absorption spectroscopy, we used a Perkin-Elmer 5100 AAS, running in flame mode to determine approximate concentrations of Na and total Fe, for the first stage of Rietveld modelling and to determine how much sample would be needed for the ICP-AES determinations. Plasma energy was adjusted to 1300 W and emission Concentrations were well above detection limits and uncertainty was about 5%.

The elements Fe, Na and S were analysed in solid and solution, after dissolution in dilute HCl (ultrapure grade), by inductively coupled plasma atomic emission spectroscopy (ICP-AES; Optima2000DV, Perkin-Elmer).intensities were measured at the selected element-specific wavelengths: 238.2 nm (Fe), 589.6 nm (Na), and 182.0 nm (S). The observation geometry of the emission light was radial for Na and axial for the other elements.

We used a Digital Instruments Multimode IIIa AFM (atomic force microscope) in scanning mode, mounted inside the glove box, to observe morphology of the solids at the various stages of GR formation and their transformation to the oxidation products. Images were collected in contact mode using standard Si_3N_4 tips and with force minimised to the point just before tip lift off. High resolution measurements of HOPG (highly ordered pyrolytic graphite) indicated that the uncertainty resulting from drift and scaling (HENRIKSEN and STIPP, 2002) in the atomic-scale images is not more than about 10%, typical for AFM data. SEM (scanning electron microscopy) showed the overall morphology of the $GR_{Na,SO4}$. We used a JEOL JSM-6335F running in secondary electron mode at 5.0 kV.

3. RESULTS AND DISCUSSION

3.1 Green rust composition

Figure 1a shows the evolution of oxidation potential (Eh) and pH in solution, starting from the initial suspension of $Fe(OH)_{2(s)}$, through its transformation to green rust, to the final oxidation product, which in this case is goethite, α-FeOOH. More information is provided about formation and transformation of green rust elsewhere (CHRISTIANSEN, 2004). Other researchers have assumed that green rust concentration is at its maximum at the point marked x (GÉNIN et al., 1996; GÉNIN and RUBY, 2004; OLOWE et al., 1989; RUBY et al., 2003; SIMON et al., 2003), but samples taken periodically and analysed simultaneously by AFM and XRD proved that the

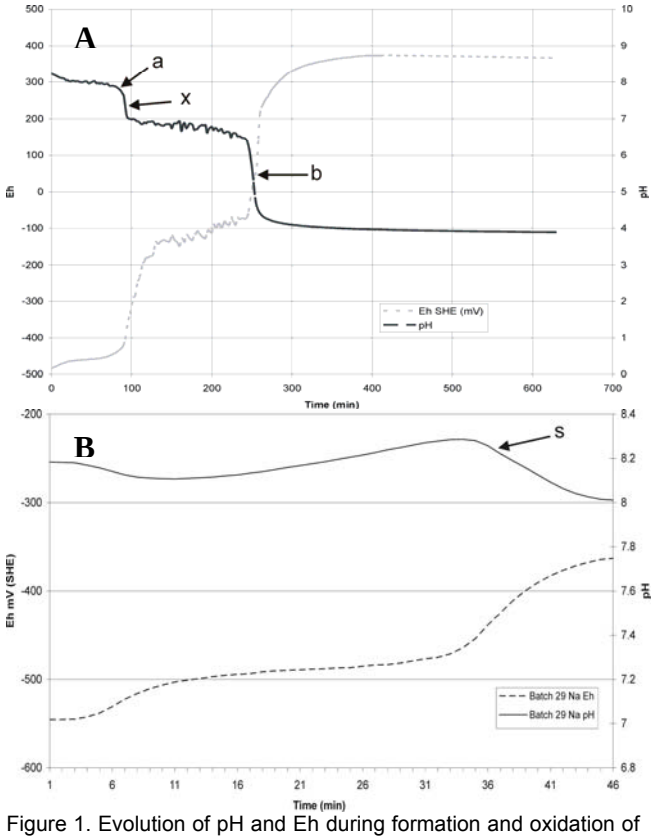

Figure 1. Evolution of pH and Eh during formation and oxidation of $GR_{Na,SO4}$. a) complete oxidation experiment and b) this experiment showing the point where oxygen addition stopped (s). Points a and b indicate sampling times for the AFM images of Figure 2. Until now, GR concentration was assumed to be maximum at x, but XRD shows 100% green rust at point a and development of some goethite at x.

maximum quantity of green rust is present at point a. At point b, the solid is essentially all goethite but by point x, some has already transformed. Figure 1b shows the solution conditions from which the samples for this study were obtained and is typical of all such experiments. Air flow, thus oxidation, stopped at point "s" and samples were taken for analysis. Samples from a and b were imaged with AFM (Figure 2) and analysed for composition. The break point in Eh and pH is easy to spot during an experiment thus optimising the production of the solid for characterisation. AFM (Figure 2) and Mössbauer spectroscopy (Figure 3) observations confirmed that other phases were present in negligible amounts. Ferrihydrite, which is easy to identify with AFM (STIPP et al., 2002) and Mössbauer spectroscopy, was completely absent.

We verified that Na is not simply adsorbed to the green rust surface. The very small amount of solution that remained after centrifugation could account for about 0.048 mg of Na in the dry sample which is subtracted from the total 0.25 mg of Na present in the sample before calculating the ratios (Table 1). The component ratios for $GR_{Na,SO4}$ are very close to those expected with a structure based on nikischerite: $Fe:SO_4 \sim 4.5:1$ and $Na: SO_4 \sim 1:2$ (Table 2). The Fe(II):Fe(III) ratios in the solid samples were determined directly using Mössbauer spectroscopy. The relative ratios of Fe, S and Na in the solid are presented in Table 2. In this system, all S is present as SO_4.

3.2 Green rust structure

The XRD patterns collected during this work resemble those reported in the literature; the strongest peaks are the basal plane Bragg reflections, at approximately 11, 5.5 and 3.7 Å, considered diagnostic for GR2 compounds (BERNAL et al., 1959). However, the slightly larger basal spacing of GR_{SO4} obtained by Lewis (1997) could result from incorporating K, from the synthesis solution, into the interlayer. Similarly, the larger basal spacing obtained by

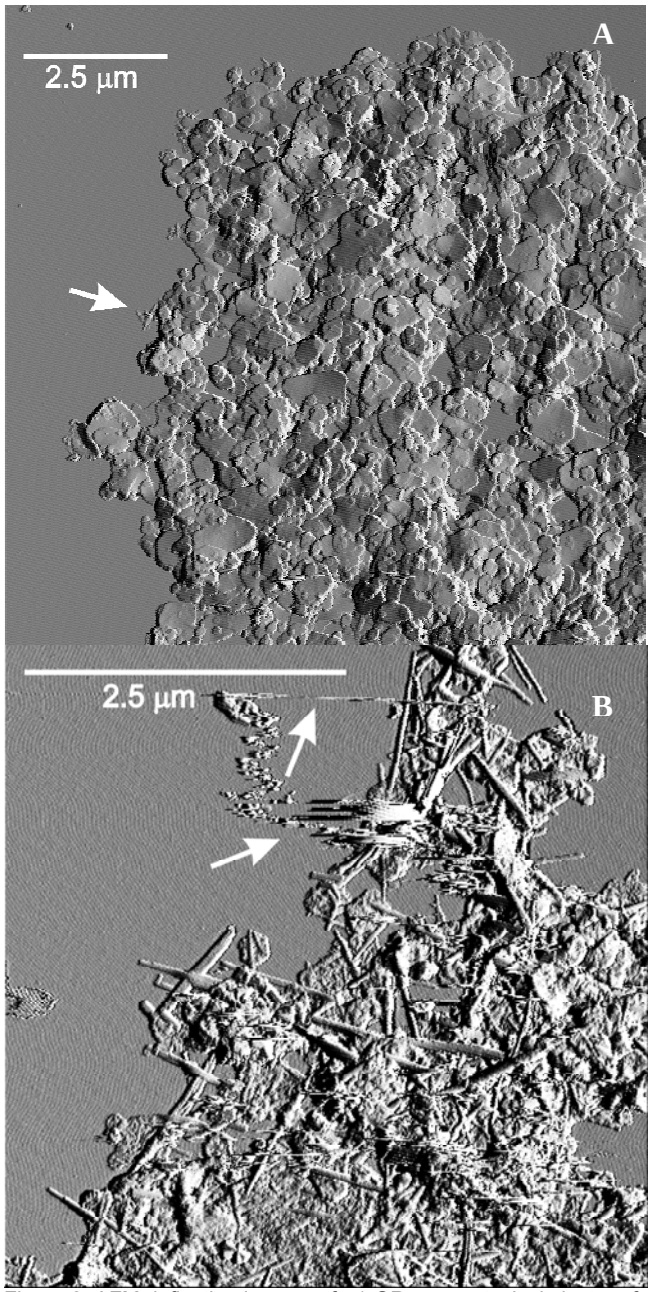

Figure 2. AFM deflection images of: a) $GR_{Na,SO4}$, a typical cluster of GR particles; the sample is essentially all GR. A few needles of goethite are visible (arrow) but there is too little to detect with XRD. b) The end product, goethite, after considerable oxygen addition. Some particles are loosely attached to the substrate, creating noise in the image (arrows). The oscillations that are especially visible on the flat muscovite surface on (b) are noise that comes from the fans in the glove box.

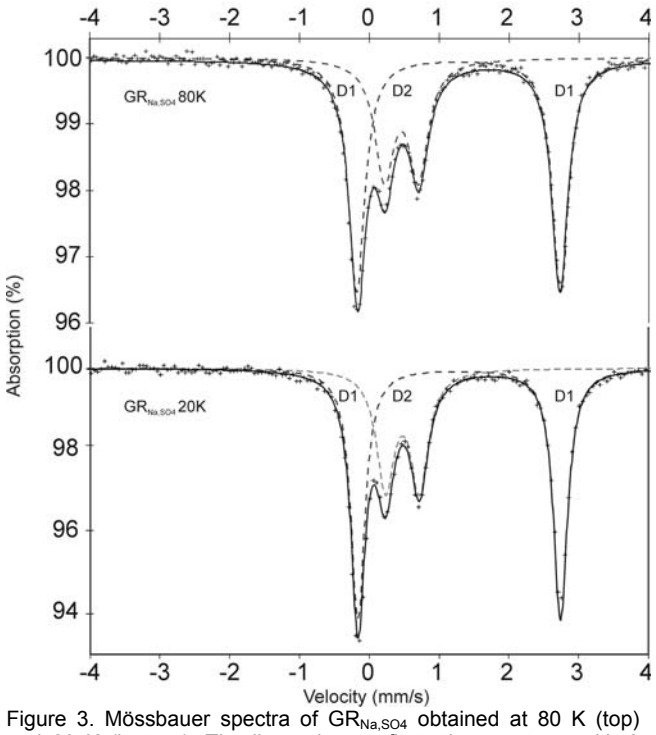

Figure 3. Mössbauer spectra of $GR_{Na,SO4}$ obtained at 80 K (top) and 20 K (bottom). The lines show a fit to the spectrum with 2 doublets. The line width of D2 is relatively large as can be expected from the environment for iron in the structure.

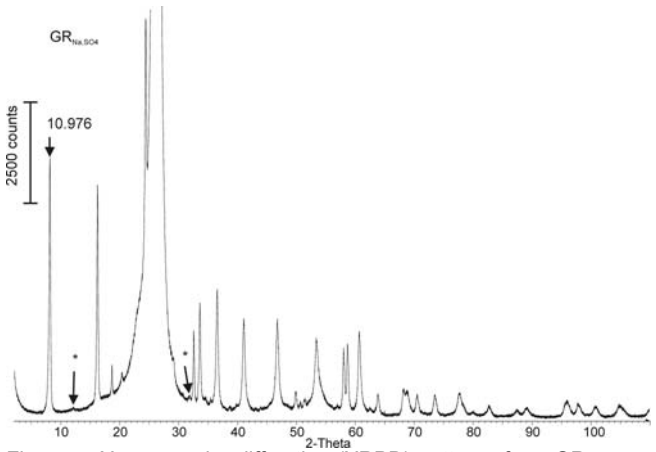

Figure 4. X-ray powder diffraction (XRPD) patterns from $GR_{Na,SO4}$. The intense, broad maximum at 25° 2θ comes from the Mylar foil used to cover the sample.

Vinš et al. (1987) could represent incorporation of NH_4 from the synthesis solution. Literature data for GR_{SO4} precipitated from Na-rich solutions have smaller basal spacings, very close to those found for $GR_{Na,SO4}$ in this work (HANSEN et al., 1994a; LIN et al., 1996; SIMON et al., 2003; SRINIVASAN et al., 1996).

Typical X-ray diffraction patterns for $GR_{Na,SO4}$ are presented in Figure 4 and the data are listed in Table 3. The data from Bernal et al. (1959) and Vinš et al. (1987) are indexed as in the original work, by the smallest unit cell ($a \approx 3.18$, $c \approx 11$ Å). The transformations from this smallest unit cell to the other unit cells used for $GR_{Na,SO4}$ are according to the following matrices: 1, 0, 0; 0, 1, 0; 0, 0, 3 (HANSEN et al., 1994a); 1, -1, 0; 1, 2, 0; 0, 0, 1 (SIMON et al., 2003) and 3, 0, 0; 0, 3, 0; 0, 0, 1 (this work). Powder patterns were collected from many separately prepared samples, both in closed capillaries and covered with Mylar foil. They were examined for consistency and for the presence of diffraction lines from additional phases. A few samples contained small amounts of the original $Fe(OH)_2$, and others, magnetite or goethite, but in general we were able to prepare essentially pure $GR_{Na,SO4}$. The very weak maxima at 7.365 Å and 2.816 Å are only observed when GR is forming and not in the beginning when $Fe(OH)_2$ is the sole phase or after the oxidation when goethite dominates. They may belong to GR and indicate larger spacing(s) resulting from a higher degree of order than assumed in our structural model, or to very small amounts of an unidentified impurity. The two weak diffraction maxima observed by (SIMON et al., 2003), but not explained by their proposed crystal lattice are observed also in our measurements and conform to the lattice assumed in this work.

We used the program Topas 3.0 (CHEARY and COELHO, 1992; CHEARY et al., 2004; KERN et al., 2004) for Rietveld refinement. The space group P-3, a subgroup of the R-3 of nikischerite, was consistent with the observed diffraction maxima. This symmetry implies an average structure that is a consequence of stacking disorder so the *c* lattice parameter was defined as 1/3 of that of an ordered structure. The refinement details are summarized in Table 4 (the structural results are supplied as supporting information). The contribution of the polyethylene terephthalate (Mylar®) to the diagram was modelled by introducing its structural details (TSE and MAK, 1975) as

Table 2. Molar ratios for $GR_{Na,SO4}$. The ideal ratios come from $NaFe(II)_6Fe(III)_3(SO_4)_2(OH)_{18}{\cdot}xH_2O$.

Sample	Fe:Na	Fe:SO_4	Na:S
1	8.661	4.435	0.5121
2	8.301	4.472	0.5387
Ideal	9	4.5	0.5

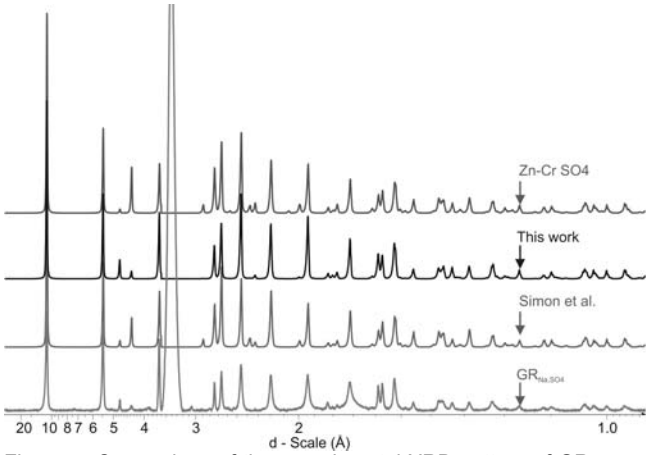

Figure 5. Comparison of the experimental XRD pattern of $GR_{Na,SO4}$ (bottom) with the three calculated models based on Zn-Cr-Na-SO_4 LDH (Ennadi et al., 1994) (Zn and Cr replaced by Fe), nikischerite (Huminicki and Hawthorne, 2003) (present work) and (Simon et al., 2003) (no Na and some water missing in the interlayer). The background around the broad maximum of the covering foil is partially cut off to allow the GR maxima to be visible.

Table 3. Powder diffraction data for GR_{SO4} from previous studies and from this one. The monovalent cations present in the precipitation medium are indicated.

NH_4 ? (BERNAL et al., 1959)			**glycerol (HANSEN et al., 1994a)**		**Na[a] (SIMON et al., 2003)**			**K (LEWIS, 1997)**	**NH_4 (VINŠ et al., 1987)**			**Na this work**		
hkl	d (Å)	I[b]	hkl	d (Å)	hkl	d (Å)	I/I_t	d (Å)	hkl	d (Å)	I/I_t	hkl	d (Å)	I/I_t
001	10.92	vs	003	11.03	001	10.89	100	11.19	001	11.2	80	001	10.976	100
												*	7.365	1
002	5.48	s	006	5.49	002	5.442	41	5.60	002	5.58	40	002	5.491	86
					010	4.728	11					110	4.775	11
					011	4.326	7					111	4.376	5
					*	3.953	4					021	3.908	2
003	3.65	s	009	3.657	003	3.610	33	3.73	003	3.77	100	003	3.656	72
					*	3.084	9					120	3.068	4
												*	2.816	2
004, 100	2.747	m	00 12, 100	2.751	004 110	2.759	31		100	2.76	20	030 004	2.752	28
101	2.660	ms	013	2.668	111	2.640	36		101	2.69	20	031	2.669	40
												014	2.602	3
102	2.459	ms			112	2.455	33		102	2.48	40	032	2.460	46
005, 103	2.195	ms	019	2.200	005 113	2.201	21		103	2.22	5	033 005	2.198	36
104	1.938	ms	10 12	1.958	114	1.945	16		104	1.94	5	034	1.942	37
			00 18	1.829					105	1.74	5	006	1.827	8
					120	1.793	5					140	1.800	5
												141	1.777	5
105	1.712	w	10 15	1.716	115	1.719	9					035	1.715	28
110	1.587	w	110	1.589	030	1.592	23		110	1.59	10	330	1.588	24
111	1.570	w	113	1.573	031	1.575	26		111	1.58	10	331 007	1.572	27
112	1.525	w	116	1.525	032	1.530	22		112	1.53	5	332	1.525	32
												117	1.485	3
			119	1.453	033	1.465	8		113	1.46	5	333	1.457	8
												060 334	1.373	11
												061	1.364	10
												062	1.334	9
												063 335	1.287	8
												064	1.228	9
												336	1.199	2
												065	1.163	4
												337 039	1.114	2
												066	1.098	4
												00 10	1.039	7
												360 338	1.037	6
												362	1.021	5
												363 00 11	0.9995	4
												068	0.9714	5

? solution composition not known.
[a] no data presented; these have been determined from Figure 2 of the article.
[b] v = very strong, s = strong, m = medium, w = weak.
* not possible with the proposed lattice parameters.

the additional phase in the refinement. For the GR, we had to place constraints on bond distances and to define the SO_4 tetrahedron as a "rigid body", thus allowing only its translation along and rotation around the *c*-axis.

The applied structural model gives a satisfactory match with the measured pattern. Figure 5 shows that this model explains the features of the observed diffraction pattern more accurately than that proposed by Simon et al. (2003) or another of our attempts based on the structure of zinc

Table 4. Crystallographic data for $GR_{Na,SO4}$ as well as instrument and refinement details

formula	$NaFe(II)_6Fe(III)_3(SO_4)_2(OH)_{18}\cdot 12H_2O$
formula weight	1198 g/mole
T (K)	299(1)
crystal system	Hexagonal
space group	P-3 (No. 147)
a (Å)	9.528(6)
c (Å)	10.968(8)
volume (Å^3)	862(1)
Z	1
D_x (Mg m^{-3})	2.306(3)
μ (cm^{-1})	319.0(5)
wavelength (Å)	1.5406 (α_1) 1.5444 (α_2)
intensity ratio α_1:α_2	2.4
2θ range	10 – 110
step size	0.02^0
divergence slit	variable
monochromator	secondary graphite
profile function	fundamental parameters
background treatment	Chebyshev polynomials (4th order)
R_{exp} (%)	2.80
R_p (%)	8.89
wR_p (%)	13.33
GOF	4.77
additional phase	polyethylene terephthalate

$R_p = 100[\sum | y_0 - y_c | / \sum y_0]^{1/2}$; $R_{wp} = 100[\sum w(y_0 - y_c)^2 / \sum w y_0^2]^{1/2}$; $R_{exp} = 100[(M - P)/ \sum w y_0^2]^{1/2}$; $GOF = R_{wp}/R_{exp}$

chromium hydroxide sodium sulphate hydrate (ENNADI et al., 1994) The three models define various types of long-range disorder consistent with different space groups and vary in their details of the interlayer structure. The nikischerite model gives the best match to the diffraction maxima, i.e., the correct relative intensities of reflections 110 and 111 with d-values 4.78 Å and 4.38 Å, negligible intensity of reflections 113 and 114 with d-values 2.90 Å and 2.38, correct relative intensities for reflections 330 and 331 with d-values 1.59 Å and 1.57 Å, etc. (indices defined using the space group of our model).

Structural disorder from stacking faults is a common feature in LDH compounds (DRITS and BOOKIN, 2001). In GR, there is a high degree of stacking disorder, consistent with lattice parameters where $c \approx 11$ Å and the space group is P-3. The interlayer atomic positions for Na, sulphate and water (Figure 6) overlap and are represented with partial occupancies. There are 3 potential sites per unit cell for Na, 6 potential sites for sulphate, 18 for water coordinating Na and 18 for water associated with sulphate. We tried refining occupancies for the symmetry-unique Na and S sites, adjusting the amount of oxygen in the sulphate and water associated with each of them accordingly. If the stacking disorder in the structure is not complete, one could expect that Na would prefer one of the sites and S the other(s). However, all occupancies converged to 1/3 within standard deviation, suggesting complete disorder. Thus, this parameter was fixed for the final refinement to minimise the number of free parameters. Atomic displacement was refined as an overall parameter. It did not change significantly from 1 Å^2, so it was also fixed to this value in the last stage of refinement.

3.3 Comparison with previous work

Our results differ in some important features from those of Simon et al. (2003) Our model requires Na atoms in the interlayer and a different orientation for sulphate, consistent with nikischerite. In our model, the bases of the sulphate tetrahedra are closest to the hydroxide layers; their apices point into the interlayer space and they are surrounded by three water molecules. Drits et al. (1987) and Ennadi et al. (1994) reported the same orientation of the sulphate groups in the other members of the hydrotalcite-group. In contrast, Simon et al. (2003) oriented the sulphate so the apical oxygen was closest to the hydroxide layer, because that gave the best refinement results. The better agreement, however, may have resulted from the lacking Na site. Sodium must have been present, because the solid was synthesised from Na solutions. Perhaps the most compelling argument for including Na in the interlayer arises from the similarity in composition of $GR_{Na,SO4}$, nikischerite and other members of the hydrotalcite family.

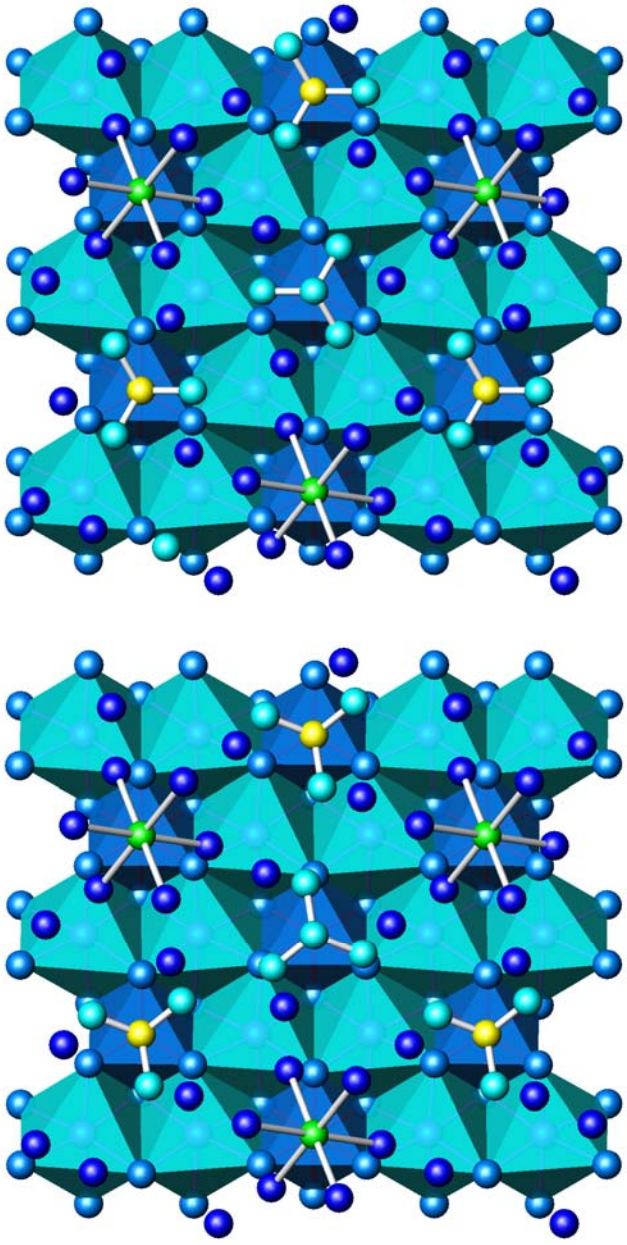

Figure 6. One hydroxide layer from the structure of (top) nikischerite and (bottom) $GR_{Na,SO4}$ together with the atoms from the overlying interlayer. Light blue coordination octahedra represent Fe(II) and Al and dark blue, Fe(III) coordination sites. Light blue represents oxygen; medium blue, hydroxide; dark blue, oxygen from water; green, Na; yellow, S.

If we compare our model to that of nikischerite (Figs. 6b with a) only very small differences are apparent. shows a similar view for GR where the overlapping are apparent. Figure 6a shows one underlying Fe-hydroxide layer and the atoms in the interlayer above it. Figure 6b shows a similar view for GR where the overlapping atoms have been removed and the same interlayer order of Na, sulphate and water as in nikischerite over the mixed sites is assumed. This assumption is valid if disorder results solely from stacking of layers that are otherwise uniform in composition. The main difference between $GR_{Na,SO4}$ and nikischerite is sulphate orientation; they are rotated by about 30° relative to each other. The reasons for this difference are not clear. The only difference in interatomic interaction that the rotation produces, is an increase in distance between oxygen in the sulphate base and the closest oxygens from the hydroxide layer (from 2.78 Å in nikischerite to 2.82 Å in GR). Because those contacts most probably represent hydrogen bonding, the differences might be caused by the different atomic species occupying cation sites in the hydroxide layers (i.e. Al + Fe in nikischerite vs. exclusively Fe in GR) and their bonding influence on hydroxide. This and the other fine details await data collected without Mylar.

3.4 Fe(II):Fe(III) ratio

The 20 and 80 K Mössbauer data for $GR_{Na,SO4}$ show four absorption peaks (Fig. 4), indicating that no magnetically ordered phases are present. In the past, Mössbauer spectra for GR synthesized from Na-rich solutions were fitted with as many as 6 doublets, (OLOWE et al., 1989) but more recent interpretations have used only two quadrupole doublets constrained to equal line width and intensity (LEWIS, 1997; SIMON et al., 2003). We have adopted this latter approach. The Mössbauer parameters are presented in Table 5. The Fe(II)/Fe(III) area ratio for $GR_{Na,SO4}$ is 63:37, making the Fe(II):Fe(III) ratio 1.7:1. This is not far from the ideal 2:1 and is consistent with other mixed metal LDH compounds (KHALDI et al., 1997). Interpretation of Mössbauer results of GR materials have, in the past, been based on various combinations of between 2 and 6 doublets (CUTTLER et al., 1990; GÉNIN et al., 2005; OLOWE et al., 1989). Our model for $GR_{Na,SO4}$ requires 3 symmetrically independent Fe sites, two for Fe(III) and one for Fe(II). It is tempting to propose, therefore, a fit with 3 components. In an ordered nikischerite-type structure, this would indeed make sense, because one of the Fe(III) sites would be flanked by $Na(H_2O)_6$ complexes on one side, and sulphate on the other, whereas the other Fe(III) site would be surrounded by three water molecules on each side. However, the structure refinement for GR shows that the two Fe(III) sites, although in distinct crystallographic positions, have a similar mixed neighbourhood. Translating the bulk structural picture into the local situation, this means that each Fe(III) atom could have as many as six different combinations of interlayer neighbours. These would consist of $Na(H_2O)_6$ complexes, sulphate or triads of water, if a complete stacking disorder is present, as the model suggests. The overall result would be an almost continuous spectrum of slightly different Fe(III) sites that could only be fitted by one somewhat broadened doublet. This is exactly what we see in the Mössbauer spectra, a slightly broadened doublet D2 (Figure 4, Table 5).

Table 5. Mössbauer parameters at 20 and 80 K.

$GR_{X,SO4}$	T (K)	IS (mm/s)	QS (mm/ s)	Line width (mm/s)	RA(%)	Site
Na	20	1.289	2.904	0.245	63	Fe(II)
		0.475	0.486	0.312	37	Fe(III)
	80	1.273	2.917	0.286	63	Fe(II)
		0.456	0.486	0.334	37	Fe(III)

IS = Isomer shift relative to α-Fe,
QS = Quadrupole splitting
RA = relative area.

3.5 Crystal morphology and surface structure

SEM and AFM images of samples taken from the bulk GR-suspension show hexagonal particles (Fig. 2a and 7) that range from a few nanometers to 2 micrometers across (average 800 nm) and 6 to 40 nm in height (average 20 nm). Figure 2b shows rods and needles typical of goethite, the final oxidation product in this case. The sample was taken from the suspension at point b on Figure 1a. Goethite often forms on or near green rust, aligning itself along one of the crystallographic *a* axes.

Mineral surfaces often have a different structure than the bulk as a result of relaxation in the outer two or three molecular layers. The dangling bonds at the termination of the bulk structure satisfy their unsatisfied charge either by reacting with the gas or liquid in contact, or in the absence of reacting species, by modifying the bonding of the surface atoms. For green rust precipitated in a solution with Na and SO_4 in excess, one could expect the surface to equilibrate unsatisfied charge by adsorbing some of the ions appropriate for the next interlayer. High resolution AFM images are consistent with this expectation. Figure 8a was taken from the basal plane of a GR crystal such as those shown in Figure 2a. We see row pattern spacing more clearly on a two dimensional Fourier transformation (Fig. 8b).

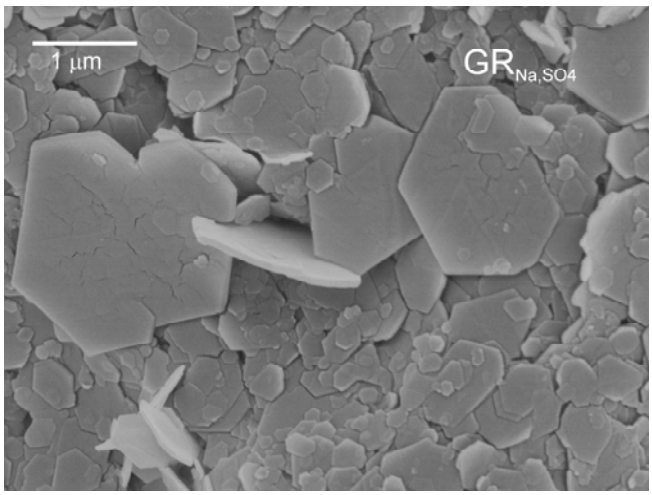

Figure 7. Secondary electron microscopy (SEM) images of $GR_{Na,SO4}$.

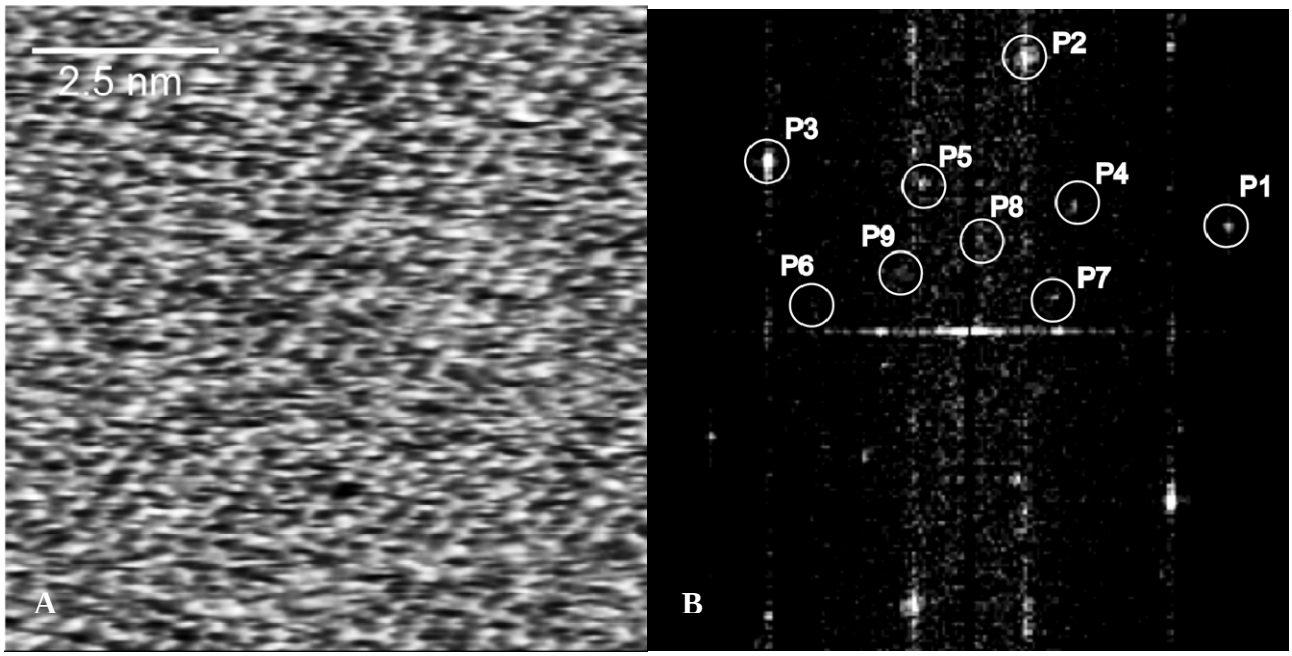

Figure 8. a) High resolution AFM image of $GR_{Na,SO4}$. b) Two-dimensional Fourier transformation of Figure 8a.

In GR, iron atoms are arranged in a hexagonal pattern, filling the octahedral interstices between the two closed-packed layers of hydroxyl (Fig. 9). The distance between two neighbouring Fe atoms or two neighbouring hydroxyl, *a*, can be derived from the distance between the atomic rows, h, by:

$$a = h/\sin(60°). \quad (1)$$

For green rust, *a* is ~ 3.17 Å. Hexagonal symmetry predicts three equal periods representing the three axes: a_1, a_2 and a_3, at 120° to each other. Row periodicities are plotted as points in reciprocal Fourier space. The main row spacing, observed easily in Figure 8a, produces the Fourier points P1, P2 and P3 on Figure 8b. From all images, their spacings are within 10% of the distances expected. Distance error in AFM images is often 10 to 15% because of difficulties in calibration and distortion caused by the non-hysteretic behaviour of the piezoelectric scanner (HENRIKSEN and STIPP, 2002). Points P1, P2 and P3 also mark the basis of the reciprocal unit cell of the first approximation for the crystallographic axes, as the smallest unit cell (BERNAL et al., 1959). In the Fourier transform, several larger periodicities are also apparent. Irrespective of drift, they show a well-defined relationship with P1, P2 and P3. The second set of Fourier points, P4, P5 and P6, are offset by 30° from the first and represent an atomic spacing $\sqrt{3}a$. This is the reciprocal unit cell in the model used by Simon et al. (2003) Finally, a third set of points, P7, P8, and P9, are observed at 1/3 the Fourier spacing, on the same axes as P1, P2 and P3. These represent the basic parameters of the reciprocal unit cell used in the present structural model.

When we examine the distribution of atoms in the basal plane of the expected 3-dimensional green rust structure (Figure 9), we see that spacing matches these three main periodicities, i.e. the repeat distance of hydroxyl along a row is *a*, the repeat distance of Fe(III), is $\sqrt{3}a$ and the repeat distance of Fe(II) is 3*a*. Thus, the corrugation in the surface imaged by AFM, which is illuminated in the 2 dimensional Fourier transforms of the high resolution AFM images, could directly represent different surface force environments over O from hydroxyl, Fe(II) and Fe(III), or it could represent force differences over adsorbed ions, namely O from H_2O, SO_4, or Na.

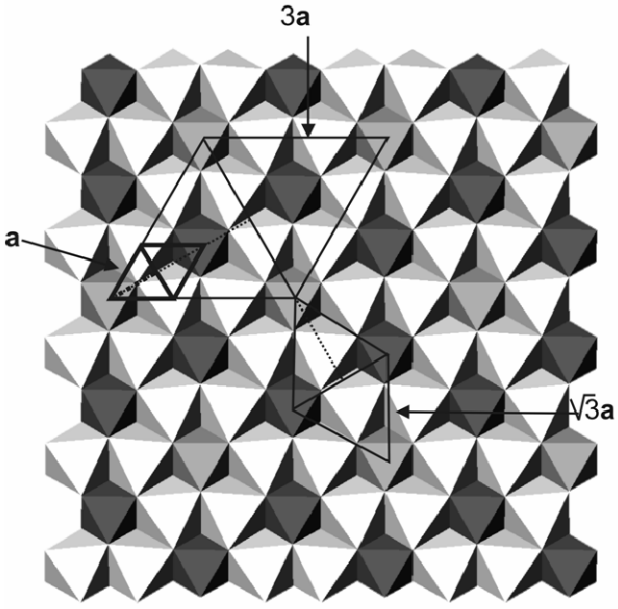

Figure 9. Structure of the iron hydroxide layer. All octahedra contain Fe and are coordinated with OH. The lightest grey polyhedra represent Fe(II), medium grey, Fe(III)1 and dark gray Fe(III)2. The periodicities observed on the green rust surface by AFM are indicated.

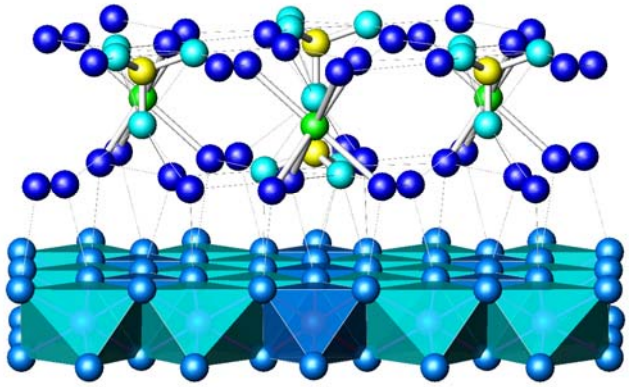

Figure 10. A portion of the $GR_{Na,SO4}$ crystal structure, an iron-hydroxide layer with cations in the overlying interlayer. Probable hydrogen bonds in the structure are indicated by thin lines to water molecules (dark blue). This view is turned about 75° from Figure 6b.

4. CONCLUSIONS AND IMPLICATIONS

We were able to confirm the reports of Drits et al. (1987) and Hansen et al. (1994a), who suggested that green rust includes Na in the interlayer. The cation is a necessary part of the crystal structure. This is consistent with observations where LDH-SO_4 collapsed when rinsed with alkali-free water (EL MALKI et al., 1989). Aside from recommending that green rust sulphate should not be rinsed or freeze-dried if it is to be characterised or used for investigations of trace component uptake, these results imply that green rust will not form or remain stable in solutions where suitable cations to help balance excess negative charge in the interlayer are absent or in limited supply.

The crystal structure of $GR_{Na,SO4}$ is of nikischerite type, highly disordered by stacking faults. It consists of Fe-hydroxide layers where all octahedral sites are occupied, whereas the octahedrally hydrated sodium, sulphate and additional water fill the interlayer spaces (Fig. 10). The basal plane spacing, $\mathbf{d_{001}}$, for the compound is 10.97 Å, while the in-plane periodicity is 9.528 Å. These parameters are well within the range expected for layered double hydroxides. The results suggest that $GR_{Na,SO4}$ has a complete occupancy of the interlayer sites.

In this work, and in many previous studies, green rust has been synthesised in neutral to alkaline solutions where oxidation potential is near the Fe(II) to Fe(III) redox transition and where SO_4^{2-}, and a common monovalent cation such as Na, have been available. Thus, one would expect $GR_{Na,SO4}$ to be observed in natural environments. Green rust is of interest to environmental scientists because of its ability to take up, or to react with, contaminating species such as trace metals, organic solvents and radioactive elements, reduce them, and sometimes immobilise them, either in the bulk or on the surface of the end-product. Although GR has been reported from natural environments, its apparent rarity is probably a simple result of its rapid reactivity in the presence of oxygen, i.e. the researcher cannot sample it and preserve it for analysis before it has oxidised and transformed to another phase. In experiments performed in our laboratory, green rust oxidised by air forms colloidal magnetite, $Fe(III)_2Fe(II)O_4$, or goethite, α-FeOOH, implying that the presence of these common iron oxides in natural samples may indicate a previous presence of green rust. It is also interesting that in several years of experiments, we have never been able to observe transformation of green rust to ferrihydrite through oxidation by air. The tendency of green rust to form nano-scale particles that are stable in the redox conditions below the groundwater table implies that they may provide a vector for transport of contaminants through porous media.

ACKNOWLEDGEMENTS.

We warmly thank Hans Christian Bruun Hansen for his encouragement to begin research on green rust compounds and his support throughout, Helene Almind, Helge Rasmussen and Bjarne Bisballe for technical assistance, Lone L. Skovbjerg and Knud Dideriksen for editing the text and other members of the NanoGeoScience group for discussion. Funding for this work was provided by Svensk Kärnebränselshandtering (SKB), FUNMIG - an Integrated Project under EC 6. Framework Program EURATOM, the Danish Natural Sciences Research Council (FNU) and the Carlsberg Foundation.

Electronic annex available: A crystallographic information file (CIF) for the compound $NaFe(II)_6Fe(III)_3(SO_4)_2(OH)_{18}\cdot 12H_2O$. This material is available free of charge via the Internet at http://www.elsevier.com.

REFERENCES

Allmann, R., 1968. The Crystal Structure of Pyroaurite. *Acta Crystal* **B24**, 972-977.

Aminoff, G. and Broomé, B., 1930. Contributions to the knowledge of the mineral Pyroaurite. *Kungliga Svenska Vetenskabs Akademiens Handlingar* **9**, 23-48.

Arden, T. V., 1950. The Solubility Products of Ferrous and Ferrosic Hydroxides. *Journal of the Chemical Society* **1**, 882-885.

Bernal, J. D., Dasgupta, D. R., and Mackay, A. L., 1959. The oxides and hydroxides of iron and their structural inter-relationships. *Clay mineral bulletin* **4**, 15-30.

Bish, D. L., 1978. Anion exchange in takovite: applications to other hydroxide minerals. *Bulletin du Bureau de Recherches Geologiques et Minieres, Section 2: Geologie des Gites Mineraux* **3**, 293-301.

Bish, D. L., 1980. Anion-exchange in takovite: applications to other hydroxide minerals. *Bulletin de Mineralogie* **103**, 170-175.

Brindley, G. W. and Bish, D. L., 1976. Green rust: a pyroaurite type structure. *Nature* **263**, 353.

Carl, H., 1842. Untersuchung über die Zusammensetzung einiger Mineralien. *Journal für Praktische Chemie* **27**, 375-378.

Cheary, R. W. and Coelho, A. A., 1992. *J. Appl. Cryst.* **25**, 109-121.

Cheary, R. W., Coelho, A. A., and Cline, J. P., 2004. *J. Res. Natl. Inst. Stand. Technol.* **109**, 1-25.

Christiansen, B. C., 2004. A transformational, structural and natural occurence study of green rust, University of Copenhagen.

Cooper, M. A. and Hawthorne, F. C., 1996. The Crystal Structure of Shigaite, $[AlMn^{2+}{}_2(OH)_6(SO_4)_2Na(H_2O)_6\{H_2O\}_6$, a Hydrotalcite-Group Mineral. *The Canadian Mineralogist* **34**, 91-97.

Coy-Laboratory, P., 2002. Model 10 Gas Analyzer Instruction Manual, Michigan.

Coy, B., 2002. Diffusion of oxygen. Pers. Comm.

Cuttler, A. H., Man, V., Cranshaw, T. E., and Longworth, G., 1990. A Mössbauer study of green rust precipitates; I, Preparations from sulphate solutions. *Clay Minerals* **25**, 289-301.

Deiss, E. and Schikorr, G., 1927. Über das Ferrohydroxyd (Eisen-2-hydroxyd). *Zeitschrift für Anorganische Chemie* **172**, 32-42.

Drissi, H., Refait, P., and Génin, J.-M. R., 1994. The oxidation of Fe(OH)(2) in the presence of carbonate ions - structure of carbonate green rust one. *Hyperfine Interactions* **90**, 395-400.

Drits, V. A. and Bookin, A. S., 2001. Crystal structure and X-ray identification of layered double hydroxides. In: Rives, V. (Ed.), *Layered double hydroxides: present and future*. Nova Science Publishers Inc., New York.

Drits, V. A., Sokolova, T. N., Sokolova, G. V., and Cherkashin, V. I., 1987. New members of the hydrotalcite-manasseite group. *Clays and Clay Minerals* **35**, 401-417.

El Malki, K., De Roy, A., and Besse, J. P., 1989. New copper-chromium layered double hydroxide compound: discussion of pillaring with intercalated tetrahedral anions. *European journal of solid state and inorganic chemistry* **26**, 339-351.

Ennadi, A., Khaldi, M., De Roy, A., and Besse, J.-P., 1994. Structural results about localization of tetrahedral oxo-anions intercalated in lamellar double hydroxides. *Molecular Crystals and Liquid Crystals Science and Technology, Section A: Molecular Crystals and Liquid Crystals* **244**, 373-378.

Gastuche, M. C., Brown, G., and Mortland, M. M., 1967. Mixed magnesium-aluminum hydroxides. I. Preparation and characterization of compounds formed in dialysed systems. *Clay Minerals* **7**, 177-192.

Génin, J.-M. R., Abdelmoula, M., Aïssa, R., and Ruby, C., 2005. Ordering in FeII-III Hydroxysalt green rusts from XRD and Mössbauer analysis (chloride, carbonate, sulphate, oxalate...); about the structure of hydrotalcite-like compounds. *Hyperfine Interactions* **166**, 391-396.

Génin, J.-M. R., Olowe, A. A., Refait, P., and Simon, L., 1996. On the stoichiometry and Pourbaix diagram of Fe(II)-Fe(III) hydroxyl-sulphate or sulphate containing green rust 2: an electrochemical and Mössbauer spectroscopy study. *Corrosion science* **38**, 1751-1762.

Génin, J.-M. R., Refait, P., Bourrié, G., Abdelmoula, M., and Trolard, F., 2001. Structure and stability of the Fe(II)-Fe(III) green rust "fougerite" mineral and its potential for reducing pollutants in soil solutions. *Applied Geochemistry* **16**, 559-570.

Génin, J.-M. R. and Ruby, C., 2004. Anion and cation distributions in Fe(II-III) hydroxysalt green rusts from XRD and Mossbauer analysis (carbonate, chloride, sulphate, ...); the "fougerite" mineral. *Solid State Sciences* **6**, 705-718.

Hansen, H. C. B., 1989. Composition, stabilization, and light absorption of Fe(II)Fe(III) hydroxy-carbonate (green rust). *Clay Minerals* **24**, 663-669.

Hansen, H. C. B., Borggaard, O. K., and Sørensen, J., 1994a. Evaluation of the free energy of formation of Fe(II)-Fe(III) hydroxide-sulphate (green rust) and its reduction of nitrite. *Geochimica et Cosmochimica Acta* **58**, 2599-2608.

Hansen, H. C. B., Koch, C. B., and Taylor, R. M., 1994b. Synthesis and Characterization of Cobalt(II)-Iron(III) Hydroxide Carbonate, a Layered Double Hydroxide Belonging to the Pyroaurite Group. *Journal of Solid State Chemistry* **113**, 46-53.

Henriksen, K. and Stipp, S. L. S., 2002. Image distortion in scanning probe microscopy. *American Mineralogist* **87**, maj-16.

Huminicki, D. M. C. and Hawthorne, F. C., 2003. The crystal structure of nikischerite, $Na\ Fe^{2+}{}_6Al_3(SO_4)_2(OH)_{18}(H_2O)_{12}$, a mineral of the shigaite group. *The Canadian Mineralogist* **41**, 79-82.

Kern, A., Coelho, A. A., and Cheary, R. W., 2004. Convolution based profile fitting. In: Mittemeijer, E. J. and Scardi, P. Eds.), *Diffraction Analysis of the Microstructure of Materials*. Springer, New York.

Khaldi, M., De Roy, A., Chaouch, M., and Besse, J. P., 1997. New Varieties of Zinc-Chromium-Sulfate Lamellar Double Hydroxides. *Journal of Solid State Chemistry* **130**, 66-73.

Kwon, S.-K., Kimijima, K., Kanie, K., Suzuki, S., Muramatsu, A., Saito, M., Shinoda, K., and Waseda, Y., 2007. Influence of silicate ions on the formation of goethite from green rust in aqueous solution. *Corrosion Science* **49**, 2946-2961.

Lewis, D. G., 1997. Factors Influencing the Stability and Properties of Green Rusts. *Advances in GeoEcology* **30**, 345-372.

Lin, R., Spicer, R. L., Tungate, F. L., and Davis, B. H., 1996. A study of the oxidation of ferrous hydroxide in sligthly basic solution to produce γ-FeOOH. *Colloids and Surfaces A: Physicochemical and Engineering Aspects* **113**, 79-96.

McGill, I. R., McEnaney, B., and Smith, D. C., 1976a. Crystal structure of green rust formed by corrosion of cast iron. *Nature* **259**, 200-201.

McGill, I. R., McEnaney, B., and Smith, D. C., 1976b. Green rust: a pyroaurite type structure. *Nature* **263**, 353-354.

Miyata, S., 1983. Anion-exchange properties of hydrotalcite-like compounds. *Clays and Clay Minerals* **31**, 305-311.

Olowe, A. A., Génin, J.-M. R., and Bauer, P., 1989. Mössbauer effect evidence of a ferrous sulphate layer in the structure of green rust 2 and its atmospheric oxidation. *Hyperfine Interactions* **46**, 437.

Ruby, C., Géhin, A., Abdelmoula, M., Génin, J.-M. R., and Jolivet, J.-P., 2003. Coprecipitation of Fe(II) and Fe(III) cations in sulphated aqueous medium and formation of hydroxysulphate green rust. *Solid State Sciences* **5**, 1055-1062.

Simon, L., François, M., Refait, P., Renaudin, G., Lelaurain, M., and Génin, J.-M. R., 2003. Structure of the Fe(II-III) layered double hydroxysulphate green rust two from Rietveld analysis. *Solid State Sciences* **5**, 327-334.

Srinivasan, R., Lin, R., Spicer, R. L., and Davis, B. H., 1996. Structural features in the formation of the green rust intermediate and γ-FeOOH. *Colloids and Surfaces A: Physicochemical and Engineering Aspects* **113**, 97-105.

Stipp, S. L. S., Hansen, M., Kristensen, R., Hochella, J., M. F., Bennedsen, L., Dideriksen, K., Balic-Zunic, T., Leonard, D., and Mathieu, H.-J., 2002. Behaviour of Fe-oxides relevant to contaminant uptake in the environment. *Chemical Geology* **190**, 321-337.

Trolard, F. and Bourrié, G., 2006. Structure of fougerite and green rusts and a thermodynamic model for their stabilities. *Journal of Geochemical Exploration Extended Abstracts presented at the 7th Symp. on the Geochemistry of the Earth's Surface (GES-7)* **88**, 249-251.

Tse, J. S. and Mak, T. C. W., 1975. *Cryst. Mol. Struct.* **5**, 75-80.

Vinš, J., Šubrt, J., Zapletal, V., and Hanousek, F., 1987. Preparation and properties of green rust type substances. *Collection Czechoslovak Chemical communication* **52**, 93-102.

Appendix 4

Neptunyl (NpO_2^+) interaction with green rust, $GR_{Na,SO4}$

Bo C. Christiansen[1,], Horst Geckeis[2], Christian M. Marquardt[2], Andreas Bauer[2], Jürgen Römer[2], Dieter Schild[2] and Susan L. S. Stipp[1]*

To be submitted to Geochimca et Cosmochimca Acta

Neptunyl (NpO_2^+) interaction with green rust, $GR_{Na,SO4}$

Bo C. Christiansen[1,], Horst Geckeis[2], Christian M. Marquardt[2], Andreas Bauer[2], Jürgen Römer[2], Dieter Schild[2] and S.L.S. Stipp[1]*

[1]Nano-Science Center, Department of Chemistry, University of Copenhagen, Universitetsparken 5, 2100 Copenhagen Ø, Denmark.

[2]Institut für Nukleare Entsorgung, Forschungszentrum Karlsruhe, Postfach 3640, D-76021 Karlsruhe, Germany

To be submitted to Geochimica et Cosmochimica Acta

Abstract

Green rust (GR), the name given to a family of Fe(II),Fe(III) layered double hydroxides, has been shown to exist in groundwater and to form when steel corrodes. It has high surface area and reactivity, especially for redox-sensitive elements such as actinides. As spent fuel rods age, 237Np is the first longer-lived radionuclide to form in the 241Pu decay series (237Np half life is 2.14 x 106 years), so it is expected to increase in abundance. Neptunium exists as pentavalent Np in the waste, where it may form the very mobile neptunyl-ion, NpO2+ in an aqueous phase. In this work, we investigated the interaction of NpO2+ and the possible reduction of Np(V) to Np(IV) by green rust sodium sulphate (GRNa,SO4). The aim of the work was to define the processes involved and to determine the final form of both the Np and the green rust. We used high-resolution techniques to observe the solids directly at the nanometer scale. The GRNa,SO4 sorbed the NpO2+ within minutes of reaction and reduced it to Np(IV). The reaction took place at the edges and on the surface of the GR. After the Np had all sorbed, the GR was allowed to oxidise completely. About 50% of the Np remained associated with the oxidised product and about 75% of the associated Np was still present as Np(IV)

1. INTRODUCTION

One approach for disposing of high level nuclear waste is to bury it deep underground. In Sweden, spent fuel rods will be packed into copper canisters lined with cast iron and then sealed in a concrete repository about 500 m below ground surface. Bentonite liners around the canisters are expected to swell in contact with groundwater, minimising leakage of radionuclides. However, tectonic movements, such as might occur during an ice age, could fracture the linings and the canisters and lead to oxidising conditions, either near the storage site, or along the ground-water flow path. To insure the safest storage method, performance assessment models are being developed to simulate conditions in and around the Radioactive waste may contain neptunium-237, a daughter product of the decay series from pressurised disposal facility but for these to be reliable, all possible geochemical reaction must be considered.

* corresponding author:
Email address: bochr@nano.ku.dk

water reactor (PWR)-UO_2 fuels (ALLARD et al., 1984). ^{237}Np has a half-life of 2.14 Ma, which is much longer than its main short-lived mother isotope, ^{241}Am, which has a half-life of 432.2 a. Thus, the amount of ^{237}Np in the nuclear waste is expected to increase during the initial 1 Ma. Under normal oxidation conditions, Np exists in two oxidation states; tetra- and pentavalent. Under strong reducing or strong oxidizing conditions it can also be present in tri- and hexavalent form. If the groundwater penetrating a ruptured canister is oxidizing and slightly basic, as might be expected for water from a freshly melted glacier flowing through fractured granite, we would expect about 65% of the neptunium to be present as the mobile species, $Np(V)O_2^+$ (ALLARD et al., 1980).

It is well-known that iron-bearing minerals, especially those containing Fe(II), control the mobility of redox sensitive contaminants in groundwater systems (ELSNER et al., 2004; MAITHREEPALA and DOONG, 2004; MORAGHAN and BURESH, 1977; WARREN and ALLOWAY, 2003). Reactive barriers containing metallic iron, such as the "iron wall"

(GILLHAM and O'HANNESIN, 1994; JIRICEK et al., 2006; ROH et al., 2000a) are often installed across the flow-path of contaminated groundwater plumes. Contaminants are then reduced to a more stable phase and incorporated in, or adsorbed on, the oxidised product, often an Fe(III)-oxide or hydroxide. In groundwater passing through fractured granite, such as at the Swedish site, normal weathering would produce high concentrations of dissolved Fe(II) and this would be augmented by corrosion of iron in the degrading repository. Thus, the mobility patterns of escaping radioactive material would be determined, in part, by the presence of Fe-bearing minerals.

Green rust (GR) is the name given to a family of mixed Fe(II), Fe(III) layered double hydroxides. Anions (e.g. CO_3^{2-}, Cl^- and SO_4^{2-}), cations (Na^+, K^+ or others) and water are structurally arranged in the interlayers (CHRISTIANSEN et al., Submitted-a; REFAIT et al., 1998a). GR has been documented under natural conditions (BEARCOCK et al., 2006; KOCH and MØRUP, 1991) and at the Fe(II)/Fe(III) redox transition zone where the concentration of dissolved Fe is high (0.1 – 9.2 mg/l) and pH is in the range 6.2 to 7.4 (CHRISTIANSEN et al., Submitted-b). The high surface area and redox sensitivity of green rust make it a likely candidate for reaction with escaped redox-active species. Most actinides have several oxidation states, which determine their solution behaviour. In general, species are more soluble in the oxidised than in the reduced state because their ability to form oxy-anions increases with charge of the cation. To assess the possibility of migration of radioactive nuclides in the environment, and to produce valid risk assessment models, it is necessary to include possible interactions between the radionuclides and the redox active species or solids that are likely to prevail in the vicinity of the canisters and down-stream from the repository.

Green rust is known to react with a number of redox sensitive species, including chromium, uranium, selenium and technetium (DODGE et al., 2003; O'LOUGHLIN et al., 2003; PEPPER et al., 2003; ROH et al., 2000b; SKOVBJERG et al., Submitted; SKOVBJERG et al., 2006). In studies of the reaction between $GR_{Na,SO4}$ and chromate (CrO_4^{2-}) and selenite (SeO_3^{2-}), Skovbjerg et al. (Submitted; 2006) showed that the reaction mechanism depended on the geometry of the anion. In the case of chromate, the reaction took place in the interlayers of the GR and the chromium was incorporated into the structure of the end-product, goethite. For selenite, reduction took place at the GR edges and the selenite was reduced to elemental selenium, which was observed to form tiny crystallites on the remaining green rust. In studies of GR interaction with uranyl (UO_2^{2+}) the hexa-valent uranium precipitated as nanoparticles of UO_2, aligned along the edges of the GR (O'LOUGHLIN et al., 2003). Np(IV) stability is within the range where $GR_{Na,SO4}$ forms (ALLARD et al., 1980) suggesting that if the rate of reaction is not a hindrance, NpO_2^+ reduction by GR is likely. No information currently exists in safety assessment models to describe Np reactivity with green rust.

The purpose of this study was to test if $GR_{Na,SO4}$ reduces pentavalent Np (as NpO_2^+) and if the reduced species is immobilised by the solid. To begin the investigation, we chose to explore the behaviour of one member of the green rust family, namely, sodium sulphate ($GR_{Na,SO4}$, $NaFe(II)_6Fe(III)_3(OH)_{18}(SO_4)_2 \cdot 12H_2O$) because its structure, composition and thermodynamic properties are well-defined (CHRISTIANSEN et al., Submitted-a; DAVESNE et al., In preparation). We used suspensions of synthetic green rust that were well over 95% pure. They were exposed to solutions containing Np(V) and the resulting solutions and solids were characterised using a range of classical and high resolution techniques.

2. MATERIALS AND METHODS

All experiments and sample preparation were conducted in anaerobic glove boxes, unless otherwise stated. We used MilliQ water (< 0.01 µS/cm) and PFA (perfluoroalkoxy) and PE (polyethylene) vessels to avoid contamination by dissolved silica, which modifies GR behaviour (KWON et al., 2007). Np-solutions were made with perchlorate, because this is one of the least complexing ions. The maximum amount of NpO_2^+ was fixed at 20 µl in the 0.0144 M Np(V) solution, to keep radiation from the experimental solutions below the required limit.

2.1. Synthesis of $GR_{Na,SO4}$

Green rust sodium sulphate was synthesized using the method described by Christiansen et al. (CHRISTIANSEN et al., Submitted-a). Briefly, we prepared 0.200 L of solution from 2.78 g $FeSO_4 \cdot 7H_2O$ (melanterite p.a. grade) so concentration was 50.00 mM. While stirring, pellets of base were added, so the Fe/OH ratio was 0.6 (83.00 mM NaOH, p.a. grade). As pH increased in the Fe(II) solution, $Fe(II)(OH)_{2(s)}$ began to precipitate. When pH reached about 8.4, the Fe(II) solid suspension was oxidised to green rust by slowly bubbling air using a peristaltic pump. To avoid formation of carbonate green rust (GR_{CO3}), the air was first purged of CO_2 by bubbling through 1 M NaOH and subsequently rinsed for NaOH by bubbling through deionised water. $Fe(OH)_{2(s)}$ transformation to GR was monitored using pH and Eh electrodes. Optimised production of GR, which minimised the presence of both the initial Fe(II)-solid and an Fe(III) end-product, was verified using XRD and AFM (Figures 1 and 2). This procedure produced about 13 g of GR.

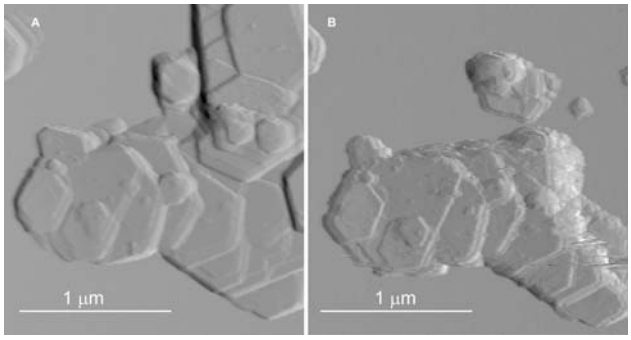

Figure 1. AFM deflection image of $GR_{Na,SO4}$ in air, at a) t=0 h and b) t=48 h. Notice that the particles has become slightly smaller. The difference in surface morphology is not because of the oxidation, but because of differences in the settings when capturing the images. The particle agglomeration in the upper right corner of A) has been pushed off by the tip in B). Scalebar is 1 μm.

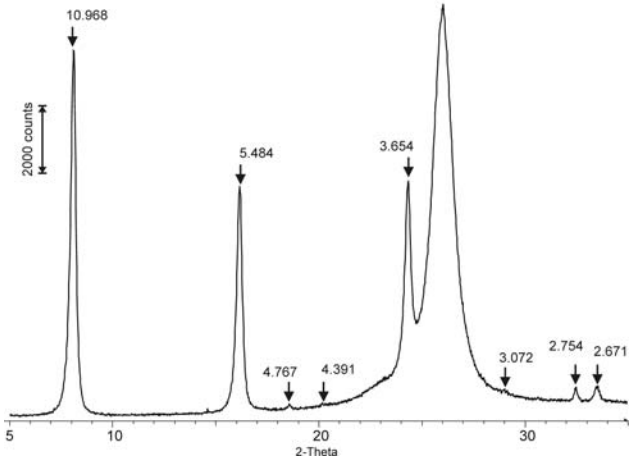

Figure 2. XRD of initial $GR_{Na,SO4}$. The numbers in the pattern indicates peak position in Ångstroms. The big broad peak at around 3.3 Å is the Mylar film.

2.2. Reaction between neptunyl (NpO_2^+) and $GR_{Na,SO4}$.

We prepared 0.0144 M Np solutions from $Np(ClO_4)_5$. Perchlorate is least complexing of all the anions, so it is preferred when stock solutions are prepared, to minimise solution and surface complexing. Volumes of 10 or 20 μl of this solution were added to the various volumes of $GR_{Na,SO4}$ slurry, both with a relatively high ratio of Np:GR and a low ratio, to enhance reaction processes for some or other of the techniques. Samples were taken periodically; solutions were analysed for composition and solids were monitored for change in the morphology, composition and structure (Table 1). The oxidation state and concentration of aqueous neptunium were determined using ultraviolet and visible light spectroscopy (UV/Vis) and liquid scintillation counting (LSC). The reaction process was observed ex-situ using atomic force microscopy (AFM), X-ray photoelectron spectroscopy (XPS), X-ray diffraction (XRD), Raman spectroscopy (RS) and scanning electron microscopy equipped with energy dispersive X-ray spectroscopy (SEM/EDS).

Cui and Eriksen (1996) reported that aqueous Fe^{2+} reacted with NpO_2^+. Their experiments were made in glassware. To test if the reaction was between aqueous Fe^{2+} and NpO_2^+, we used PE vessels and added 10 μl of the Np solution to 3 ml of a filtered supernatant from a GR suspension. LSC and UV/Vis analysis indicated that about 10% of the initial Np(V) was removed from solution, either by sorption to the vessel walls, or by reduction to Np(IV) through reaction with $Fe^{2+}{}_{(aq)}$.

To test how perchlorate might effect GR stability, we prepared a solution of $NaClO_4 \cdot H_2O$ with green rust. The Fe(II):ClO_4^- molar ratio was 8, so if perchlorate was reduced, we could monitor it as increased chloride concentration. Analysis for Cl^- and ClO_4^- using ion chromatography (Metrohm 861) showed no significant change in Cl^- concentration during 18 hours of exposure, indicating that no redox reaction took place. These observations are consistent with those reported by (LEWIS, 1997) for his study of GR_{ClO4}.

2.3. Techniques

X-ray photoelectron spectroscopy (XPS) measures the energy of photoelectrons that escape from the top few molecular layers of a solid sample during irradiation with an X-ray beam. Knowing the incident photon energy, the electron binding energy is determined and used to identify the elements from which the photoelectrons came as well as the type of bonding between the parent atoms and its neighbours. Thus, oxidation state as well as bonding environment can be determined. We used a PHI model 5600, with Al K_α radiation (1486.6 eV) both from a Mg/Al dual anode and from a monochromatised source. Background pressure in the ultrahigh vacuum chamber was about 7×10^{-8} Pa (5.25×10^{-10} torr). We prepared samples by pressing the wet paste from a 2 ml centrifuge tube onto indium foil and moved them from the glove box to the vacuum chamber using an anaerobic transfer vessel. Samples were kept in the entry chamber, pumping overnight to remove associated water. The XPS spectra revealed no evidence of oxidation or reduction from exposure to the X-ray beam. Although the fresh green rust was conducting, the oxidised end-product was insolating, so charge neutralization by slow electrons was applied to minimise surface charging.

During scans, the angle of emission, i.e. the angle between surface normal and analyzer axis, was 20°. Survey spectra were acquired to identify the elements present at the surface and to determine atomic concentration using standard methods. The binding

Table 1. Overview of samples and techniques applied.

Experiment	*Technique*
High Np:GR ratio	
80 µl GR solution + 20 µl Np(V)	TEM, XRD, SEM/EDS, RS
20 µl Np(V) (dry) + 80 µl GR solution	AFM
Low Np:GR ratio	
8 ml GR solution + 20 µl of Np(V)	UV/VIS, XPS, LSC
2 ml GR solution + 20 µl Np(V)	AFM, XPS, LSC, SEM/EDS
2 ml GR solution + 20 µl Np(V) oxidised in solution	XPS, UV/VIS
2 ml GR solution + 20 µl Np(V) dry sample oxidised	XPS
2 ml of oxidised GR solution + 20 µl Np(V)	LSC, UV/VIS
80 µl GR solution + 20 µl Np(V) oxidised dry	RS
ClO_4:GR - 1:1 ratio	
200 ml $GR_{Na,SO4}$ solution + 10 mM $NaClO_4$	IC

AFM: atomic force microscopy; XPS: X-ray photoelectron spectroscopy; LSC: liquid scintillation counting; UV/VIS: ultraviolet-visible light spectroscopy; SEM/EDS: scanning electron microscopy – energy dispersive X-ray spectroscopy; RS: Raman spectroscopy; IC: ion chromatrography.

energy scale was calibrated by use of the Cu $2p_{3/2}$, Ag $3d_{5/2}$, and Au $4f_{7/2}$ lines of sputter-cleaned pure metal foils (SEAH et al., 1998). Narrow scans of the elemental lines were acquired with pass energy of 11.75 eV in the hemispherical analyzer at 0.1 eV/step (0.1 s/step). For definition of the Np 4f satellites an intermediate resolution (46.95 eV pass energy) was used to increase analyser transmission, thus enhancing count rates for these low intensity peaks.

Atomic Force Microscopy (AFM) can image particles and surfaces, allowing observation of changes in morphology induced by GR-Np(V) reactions. Lateral resolution can be less than an Ångström and vertical resolution, a factor of at least 10 better. Imaging was conducted with a Nanoscope IV using standard Si_3N_4 tips in contact mode. To prepare a sample, a droplet of $GR_{Na,SO4}$ slurry was deposited on a piece of freshly cleaved mica. The particles were allowed to settle for 30 seconds before a short jet of MilliQ water was applied to the sample to remove excess solution. Subsequently, the water was sucked up with a tissue without touching the area intended for imaging and the sample was left to dry in the glove box. The samples were observed with AFM outside the anaerobic glove box. To determine the extent of reaction of such a sample, with oxygen during the time required for a typical imaging session, a Np(V)-free sample was prepared and imaged inside a glove box. There was no observable difference between the two samples. For imaging samples of Np-containing GR, the slurry was allowed to react for about 10 min before a droplet of solution was deposited on a freshly cleaved mica surface.

For Scanning electron microscopy (SEM) and energy dispersive X-ray spectroscopy (EDS) we used a Camscan CS44FE. Samples were prepared in the glove box, from a droplet of suspension on a piece of carbon tape. The sample was transferred in an air tight container to the SEM/EDS and examined without a conductive coating. Powder XRD patterns were recorded using a Bruker D8 powder diffractometer equipped with a BSI (Baltic Scientific Instrument) Si(Li) solid detector, and $Cu_{K\alpha}$ radiation. Intensities were recorded from 5 to 70° 2θ,, using 0.01 ° 2θ steps, and a 1 s counting time per step. We dried a droplet of solution containing 0.02 g of material on a silicon wafer and used a special X-ray transparent cap (Bruker Dome, Polytron) with a low oxygen diffusion rate, to minimise oxidation and to avoid interference peaks from the plastic. Samples for Raman spectroscopy (RS) were analyzed on a Bruker Senterra. The samples were analysed with the laser at 785 nm. They were prepared from a droplet of slurry dried on a silicon wafer. The purpose of the Raman analysis was to compare peaks for $GR_{Na,SO4}$ with those of the reaction products from the interaction between $GR_{Na,SO4}$ and neptunyl and to estimate how the Np was bound in the oxidised end product. Therefore, the sample was not protected against oxidation. Analysis by ultraviolet and visible light spectroscopy was made on a Cary 5 from Varian. Samples in 4 ml cuvettes were then capped with a lid with a silicone membrane and analysed within 15 minutes. The wavelength-band that we investigated for Np(V) was 950 to 1020 nm. Np concentration was determined directly by liquid scintillation counting (LSC) from samples that were prepared with 100 µl of slurry and 10 ml of Ultima Gold (Perkin Elmer). We used a Tricarb scintillation counter from Perkin-Elmer.

3. RESULTS AND DISCUSSION

UV/Vis analysis of the centrifuged supernatant, made within 10 min after reaction of 2 ml $GR_{Na,SO4}$ solution with 20 µl $Np(ClO_4)_5$ solution revealed no visible line in the range where the Np(V) absorbance band is expected. These results indicate that all Np(V) was removed from solution. To test if the removal was

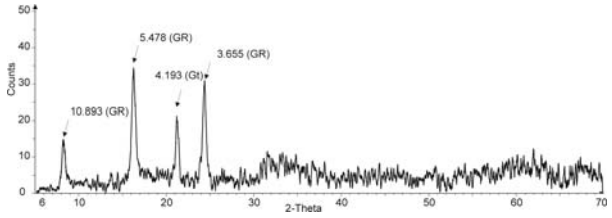

Figure 3. XRD diagram of Np reacted $GR_{Na,SO4}$. Numbers are d-spacing in Ångström, GR indicates $GR_{Na,SO4}$ peaks, and Gt indicates goethite peak.

a result of sorption to the walls of the cuvettes we analysed the solid with liquid scintillation. The results confirmed all Np was in the solid.

Analysis by XRD of the sample before and after reaction showed that $GR_{Na,SO4}$ had reacted with the neptunium solution to produce goethite (Fig. 3). With AFM, we could observe changes in $GR_{Na,SO4}$ particle morphology before and after reaction with neptunium. Originally flat, hexagonal particles transformed to particles with a cross-hatched surface, surrounded by a coherent, hexagonal rim (Fig. 4). Such a change cannot be explained by reaction with oxygen in the air during imaging because other experiments have proven that it takes more than 8 hours to oxidise GR attached to mica, and when it is allowed to oxidise for 48 hours, it does not form goethite needles, but keeps the hexagonal outline although it decreased in size (Fig. 1). The shape and pattern of change for GR exposed to Np is similar to that observed when CrO_4^{2-} reacts with $GR_{Na,SO4}$ (SKOVBJERG et al., 2006). Where a species is reduced by green rust oxidation and it cannot exchange with the interlayer anion, discrete particles of a secondary phase form along the edges of green rust (O'LOUGHLIN et al., 2003; SKOVBJERG et al., Submitted) but chromate fits in the interlayer, replacing sulfate. The reaction proceeds in two steps: first, chromate exchanges into the perimeter of the GR hexagons, 50 nm deep into the crystals. Next, chromate adsorbs on the GR surface and becomes reduced but at a slower rate. In the studies where uranyl (O'LOUGHLIN et al., 2003) or selenite (SKOVBJERG et al., Submitted) reacts with $GR_{Na,SO4}$ small particles are formed along the edge of the GR particles, indicating that the compounds do not enter the interlayer of the GR. Reaction of neptunyl is expected to be similar to uranyl because the shape of the ion is the same $O=Np^{+}=O$ (with double bond instead of triple bond). The electronegativity of neptunyl is however different (monovalent vs. di-valent) and it may thus behave different to that of uranyl (UO_2^{2+}). The negative oxygen ends may lead to exchange of sulphate and the overall positive valence that also sodium is exchanged.

To test where the reaction between neptunyl and $GR_{Na,SO4}$ took place, we used SEM with EDS. The SEM images showed hexagonal crystals typical of GR (Fig. 5) and EDS showed no evidence of Np in the solid, in the areas where the beam met the sample perpendicular to the basal plane of the GR particles (Fig. 5a). When the EDS beam was focused on the end of GR particles, i.e. parallel to the basal planes, the Np peak was visible (Fig. 5b). The amount of Np in these areas was as much as 8 wt %. This indicates that there is a difference in where the Np is attached. If neptunium was evenly distributed on the GR surface/interlayer, one would expect a homogeneous surface concentration. Np located mostly at the edges, would produce a non-homogeneous pattern (Fig. 5c). It is not possible to interpret with SEM/EDS

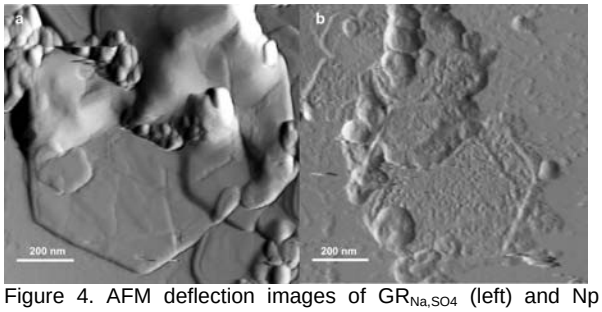

Figure 4. AFM deflection images of $GR_{Na,SO4}$ (left) and Np reacted GR. The hexagonal shape of the $GR_{Na,SO4}$ particle is clear on both images. On the right image the particle exhibits a hexagonal rim that seems to have fused, and internally in the particle a crosshatched pattern is visible, indicating that a reaction has changed the morphology of the $GR_{Na,SO4}$.

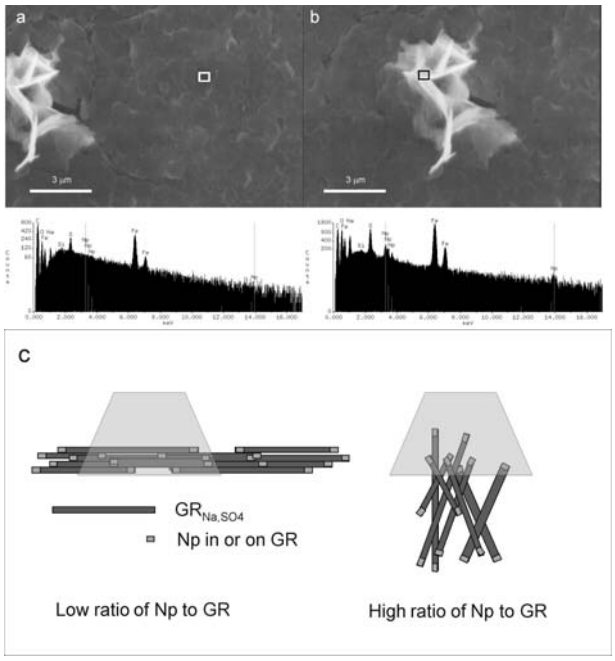

Figure 5. SEM image of Np reacted $GR_{Na,SO4}$. a and b) square indicates EDS area of the sample. c) interpretation of why the Np is not consistently present in all areas of the sample. If the particles only have Np in/on edges, then the ratio of Np to GR will be low, and Np can not be identified with in the sensitivity of the EDS. If the particles sit with the edges pointing up-wards then the ratio between Np and GR will be high and Np can be identified.

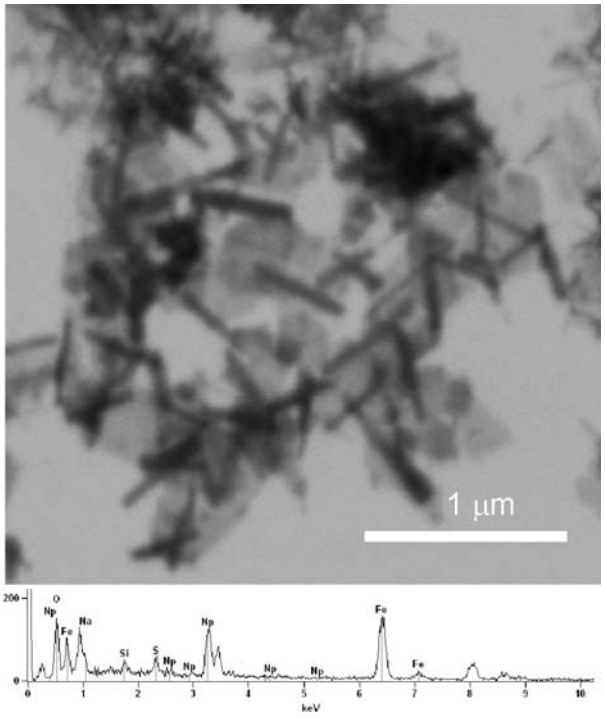

Figure 6. TEM image of Np reacted $GR_{Na,SO4}$. The more dense goethite particles shows up as dark needles in the image, the $GR_{Na,SO4}$ is the hexagonal particles. At the bottom is an EDS of the area, showing Np present in the solids.

whether the Np is adsorbed to or in the edges. It was possible to obtain pseudo-TEM images of the samples. The images all exhibit goethite needles and hexagonal shaped GR particles (Fig. 6). In a study by O'Loughlin et al. (2003) they found that U(VI) reacts with the GR_{SO4} and produced uranium nano-particles. The TEM images in that study (O'LOUGHLIN et al., 2003) exhibited clearly the nano-sized particles. In our TEM images it is not possible to indentify any particles with such morphology (Fig. 6).

Transition elements, including the actinides, exist in states where they have unpaired electrons. For the actinides, the unpaired electrons can hybridizise between the *p* and *f* electron shells. The hybridization creates distinct shake-up lines in the *4f* band (GUNNARSSON et al., 1988) of XPS. The shake-up lines shift in binding energy at the *4f* level depend on the oxidation state (KRAUSE et al., 1988; TETERIN and TETERIN, 2004; VEAL et al., 1977), meaning that XPS can be used to test the oxidation state of the higher actinides. In our results the XPS spectra (Fig. 7) of the Np *4f* shell binding energy range (Fig. 8), reveals the two main peaks of Np $4f_{5/2}$ and $4f_{7/2}$ positioned at 415.1 eV and 403.5 eV. Shake-up peaks are measured at 6.1 eV higher binding energies than the *4f* peaks, similar to the shake-up lines observed when Np(IV) compounds are forming (TETERIN and TETERIN, 2004). The ratio between the satellites and the main peaks is estimated to be 0.36 when it is 100% Np(IV)-oxide (NAEGELE et al., 1987).

Raman spectroscopy confirmed the presence of goethite (Fig. 9, Table 2). Raman spectroscopy also showed that the spectra of the Np-$GR_{Na,SO4}$ sample wasquite similar to that of pure $GR_{Na,SO4}$, the spectra of Np-$GR_{Na,SO4}$ contains a couple of extra peaks (Fig. 10). Most of these peaks can be attributed to the presence of goethite, and also perchlorate (952 cm^{-1}). There is some that is not attributable to $GR_{Na,SO4}$, goethite and perchlorate. These peaks are still present when the sample has oxidised. The literature on Raman spectroscopy and Np(IV) compounds is unfortunately

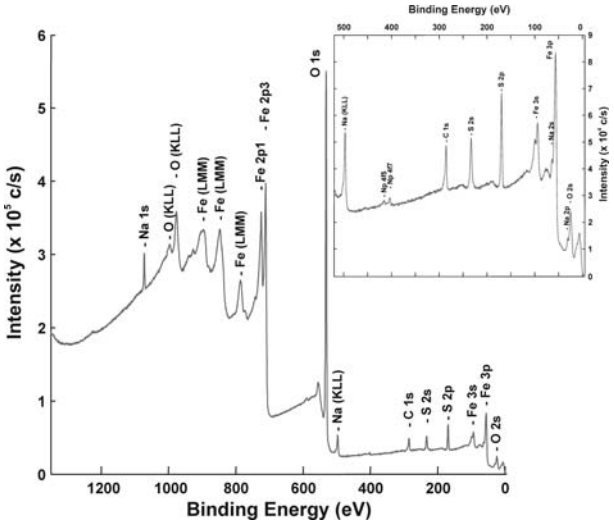

Figure 7. X-ray photoelectron spectroscopy (XPS) survey scan of 2 ml $GR_{Na,SO4}$ reacted with 20µl Np solution. Insert is a zoom of the 0-500 eV binding energy. Initials indicate identified elements and the corresponding electron shell.

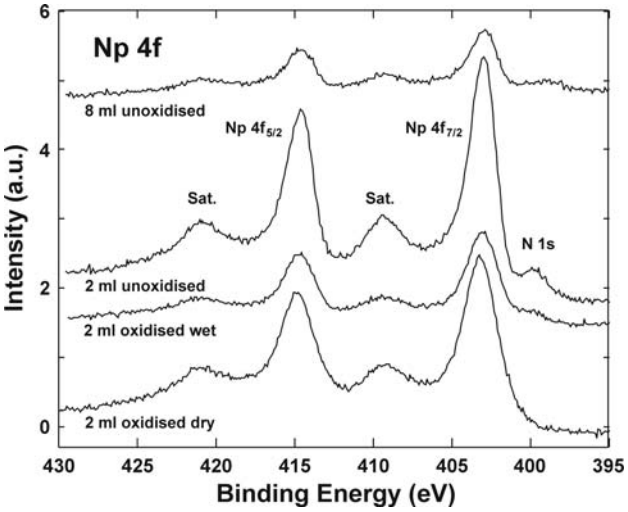

Figure 8. XPS narrow scans of Np 4f. Top line: 2 ml $GR_{Na,SO4}$ + 20 µl Np solution, 2nd from top: sample with 2 µl + 20 µl Np solution oxidised dry, 3rd line from top: 8 ml of $GR_{Na,SO4}$ + 20 µl Np solution, bottom line: 2 ml of $GR_{Na,SO4}$ + 20 µl Np solution oxidised in solution.

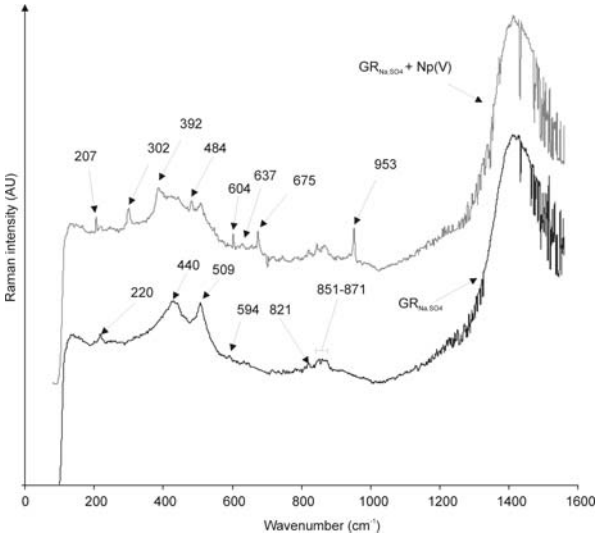

Figure 9. Raman spectroscopy of $GR_{Na,SO4}$ (bottom) and Np reacted $GR_{Na,SO4}$ (top). Numbers indicates peak positions in cm^{-1}. The broad line at the right is the vibrational area of water molecules. Identification of the peaks are summarised in Table 2.

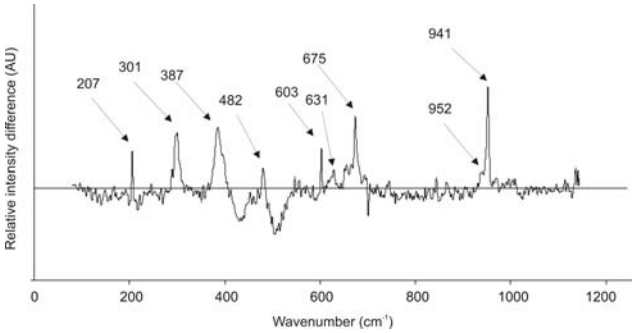

Figure 10. The difference of peaks of the Raman spectra of Figure 9. The line is a guide to the eye, above the line should be considered positive and below negative. Positive peak positions indicate peaks present in the Np reacted $GR_{Na,SO4}$ sample, and negative indicates a peak that was present in the $GR_{Na,SO4}$ sample.

scarce, but some of the peaks lie in the range of what is expected for NpO_2 compounds (~650 cm^{-1}) (ELLER et al., 1998) indicating that Np is bound in the structure of goethite in a similar way as in the neptunium oxide or as a discrete phase. To test if it was adsorbed we added 20 µl Np solution to a $GR_{Na,SO4}$ solution that had already been oxidised completely. Analysis by LSC on the supernatant showed that all neptunium was still present in the aqueous phase, meaning that there was not adsorped any Np by the oxidised solid.

Comparing the areas of the satellites with the main peaks of Np allowed us to quantify the XPS data of the samples (Fig. 8). Quantification showed that when the pentavalent neptunium came in contact with $GR_{Na,SO4}$ approximately 85% was reduced to Np(IV). When the sample is oxidised completely the final redox state depends on how it becomes oxidised. We found that when it is oxidised in dry state, all neptunium is still present in the solid, and a vast amount is still tetravalent, because of broadening of the shake-up lines it is not possible to quantify how much is still

Table 2. Raman spectroscopy.

Wavenumbers (cm^{-1})		*Band assignment*	*Ref*
$GR_{Na,SO4}$	$GR_{Na,SO4}$ + $Np(ClO_4)_5$ solution		
	207	Melanterite?	
220	220	Symmetric stretch of interlayer chloride ions in GR?	(SIMARD et al., 2001)
	250	Goethite	(DE FARIA et al., 1997)
	302	Goethite	(DE FARIA et al., 1997)
	391	Goethite	(DE FARIA et al., 1997)
432-444	430-444	Fe^{2+}-OH GR stretching band	(BESSIÉRE et al., 1999; REFAIT et al., 1998b)
	450-480	NpO_2?	(ELLER et al., 1998)
	484	Goethite	(DE FARIA et al., 1997)
510	512	Fe^{3+}-OH GR stretching band	(BESSIÉRE et al., 1999; REFAIT et al., 1998b)
594			
	604	Symmetric stretch of interlayer sulphate ions in GR?	(BESSIÉRE et al., 1999)
	634	$NaClO_4$ - NpO_2???	(BEGUN et al., 1990; GU et al., 2004)
	675	Magnetite	(THIERRY et al., 1988)
821	821	Sulfate salt?	
851-871	851-871	Sulfate salt?	
	953	ClO_4	(GU et al., 2004)

tetravalent. If the oxidation happens in solution, then about half of the neptunium is lost from the solid phase, but of the remaining part, 75% is present as tetravalent Np. In other studies, it has been found that pentavalent neptunium do not diffuse into the structure of goethite, but adsorbs to the surface (COMBES et al., 1992). Goethite is also the one with most Np(V) adsorbed compared to amorphous iron-hydroxides, magnetite and hematite (TOCHIYAMA et al., 1995). The Np(V) adsorption to goethite have been shown to be highest at pH above 6 (NAKAYAMA and SAKAMOTO, 1991). This is in agreement with the observation that no Np was adsorbed when it was allowed to react with the oxidised $GR_{Na,SO4}$. pH of an oxidised untitrated $GR_{Na,SO4}$ solution is expected to be around 4-5 (CHRISTIANSEN, 2004). Our results indicate, thus, that the final iron(oxyhydr)oxide, goethite, can incorporate some Np in its structure as tetravalent, if the reaction takes place *via* $GR_{Na,SO4}$. Our results are in agreement to what has been observed with Eu^{3+} incorporation into hydrotalcite (STUMPF et al., 2007) and Am^{3+}, Lu^{3+}, Eu^{3+} in iron(oxyhydr)oxides (DARDENNE et al., 2002; STUMPF et al., 2006), where between 2 and 5 at% could be incorporated into the structures. The amount Np immobilised by reduction to Np(IV) by $GR_{Na,SO4}$ was in our study equal to ~ $2*10^{-3}$ moles Np/mole $GR_{Na,SO4}$, and around $1*10^{-3}$ moles Np(IV)/g $GR_{Na,SO4}$ was still sorbed after oxidation under ambient conditions. We have not been able to identify where and how it is bound in the solid.

4. IMPLICATIONS

The results imply that if there is a leakage of Np from a repository, then most of the leakage might get captured by the GR present in the environment. If the Np incorporated GR is oxidised completely, then the Np can become captured in the final oxide. We did not observe formation of nanosized uranium-(oxyhydr)oxide particles but only goethite. There is however the possibility of transport by the GR, but because this will react with oxidising elements it will transform into other iron minerals, and become immobilised. Depending on the composition of the groundwater, other green rust forms, such as the chloride (water with high salinity) and carbonate (water with high bicarbonate content) would also be expected. The difference in interlayer spacing of the different GR types could influence how neptunium reacts with GR. In groundwaters surrounding the repositories, there is high concentrations of Cl^-, CO_3^{2-} and SO_4^{2-} so until results of the GR_{Cl} and GR_{CO3} systems are available, $GR_{Na,SO4}$ should be taken into account when performing risk assessments of waste repositories.

Acknowledgements

We thank Peer Jørgensen, Helene Almind, Markus Plaschke and Eva Soballa for technical support, the NanoGeoScience group for discussion and especially Knud Dideriksen and Sorin Nedel for constructive comments. This work was mostly funded by the FUNMIG integrated project, under the 6. Framework EURATOM program and the Svensk Kärnbränslehantering AB (SKB) and with some support from the Danish Natural Science Research Council (FNU).

REFERENCES

Allard, B., Kipatsi, H., and Liljenzin, J. O., 1980. Expected species of uranium, neptunium and plutonium in neutral aqueous solutions. *Journal of Inorganic and Nuclear Chemistry* **42**, 1015-1027.

Allard, B., Olofsson, U., and Torstenfelt, B., 1984. Environmental actinide chemistry. *Inorganica Chimica Acta* **94**, 205-221.

Bearcock, J. M., Perkins, W. T., Dinelli, E., and Wade, S. C., 2006. Fe(II)/Fe(III) 'green rust' developed within ochreous coal mine drainage sediment in South Wales, UK. *Mineralogical Magazine* **70**, 731-741.

Begun, G. M., Haire, R. G., Wilmarth, W. R., and Peterson, J. R., 1990. Raman spectra of some actinide dioxides and of EuF2. *Journal of the Less Common Metals* **162**, 129-133.

Bessiére, J., Perdicakis, M., and Humbert, B., 1999. Formation de la rouille verte II sulfate Fe6(OH)12SO4 par oxydation du sulfate ferreux par l'eau. *Comptes Rendus de l'Académie des Sciences* **IIC**, 101-105.

Christiansen, B. C., 2004. A transformational, structural and natural occurence study of green rust.

Christiansen, B. C., Balic-Zunic, T., Petit, P.-O., Frandsen, C., Mørup, S., Geckeis, H., Katerinopoulou, A., and Stipp, S. L. S., Submitted-a. Composition and structure of an iron-bearing, layered double hydroxide (LDH) – Green rust sodium sulphate. *Geochimica et Cosmochimica Acta*.

Christiansen, B. C., Balic-Zunic, T., and Stipp, S. L. S., Submitted-b. Natural occurrences of green rust. *Environ. Sci. Technol.*

Combes, J. M., Chisholm-Brause, C. J., Brown, G. E., Parks, G. A., Conradson, S. D., Eller, P. G., Triay, I. R., Hobart, D. E., and Miejer, A., 1992. EXAFS spectroscopic study of neptunium(V) sorption at the α-iron hydroxide

oxide (α-FeOOH)/water interface. *Environ. Sci. Technol.* **26**, 376-382.

Cui, D. and Eriksen, T. E., 1996. Reduction of Tc(VII) and Np(V) in solution by ferrous iron. *A laboratory study of homogeneous and hetereogeneous redox processes*. Svensk Kärnbränslehantering AB, Stockholm.

Dardenne, K., Schafer, T., Lindqvist-Reis, P., Denecke, M. A., Plaschke, M., Rothe, J., and Kim, J. I., 2002. Low Temperature XAFS Investigation on the Lutetium Binding Changes during the 2-Line Ferrihydrite Alteration Process. *Environ. Sci. Technol.* **36**, 5092-5099.

Davesne, E., Dideriksen, K., Christiansen, B. C., Ayala-Luis, K. B., Koch, C. B., Hansen, H. C. B., and Stipp, S. L. S., In preparation. Determination of the free energy of formation of sodium- and sulphate-containing green rust (Na-Fe(II)-Fe(III) hydroxide-sulphate). *Geochimica et Cosmochimica Acta*.

De Faria, D. L. A., Silva, S. V., and De Oliveira, M. T., 1997. Raman microspectroscopy of some iron oxides and oxyhydroxides. *Journal of Raman Spectroscopy* **28**, 873-878.

Dodge, C. J., Francis, A. J., Gillow, J. B., Halada, G. P., Eng, C., and Clayton, C. R., 2003. Association of Uranium with Iron Oxides Typically Formed on Corroding Steel Surfaces. *Environmental Science and Technology* **36**, 3504-3511.

Eller, P. G., Asprey, L. B., Kinkead, S. A., Swanson, B. I., and Kissane, R. J., 1998. Reactions of dioxygen difluoride with neptunium oxides and fluorides. *Journal of Alloys and Compounds* **269**, 63-66.

Elsner, M., Schwarzenbach, R. P., and Haderlein, S. B., 2004. Reactivity of Fe(II)-Bearing Minerals toward Reductive Transformation of Organic Contaminants. *Environmental Science and Technology* **38**, 799-807.

Gillham, R. W. and O'Hannesin, S. F., 1994. Enhanced Degradation of Halogenated Aliphatics by Zero-Valent Iron. *Ground Water* **32**, 958-967.

Gu, B., Tio, J., Wang, W., Ku, Y.-K., and Dai, S., 2004. Raman Spectroscopic Detection for Perchlorate at Low Concentrations. *Applied Spectroscopy* **58**, 741-744.

Gunnarsson, O., Sarma, D. D., Hillebrecht, F. U., and Schönhammer, K., 1988. Electronic structure of the light actinide oxides from electron spectroscopy (invited). *Journal of Applied Physics* **63**, 3676.

Jiricek, M., Sracek, O., and Janda, V., 2006. Removal of chlorinated solvents from carbonate-buffered water by zero-valent iron. *Central European Journal of Chemistry* **5**, 87-106.

Koch, C. B. and Mørup, S., 1991. Identification of green rust in an ochre sludge. *Clay Minerals* **26**, 577-582.

Krause, M. O., Haire, R. G., Keski-Rahkonen, O., and Peterson, J. R., 1988. Photoelectron spectrometry of the actinides from Ac to Es. *Journal of Electron Spectroscopy and Related Phenomena* **47**, 215-226.

Kwon, S.-K., Kimijima, K., Kanie, K., Suzuki, S., Muramatsu, A., Saito, M., Shinoda, K., and Waseda, Y., 2007. Influence of silicate ions on the formation of goethite from green rust in aqueous solution. *Corrosion Science* **49**, 2946-2961.

Lewis, D. G., 1997. Factors Influencing the Stability and Properties of Green Rusts. In: Auerswald, K., Stanjek, H., and Bigham, J. M. Eds.), *Advances in GeoEcology*. Catena Verlag, Reiskirchen, Germany.

Maithreepala, R. A. and Doong, R. A., 2004. Reductive Dechlorination of Carbon Tetrachloride in Aqueous Solutions Containing Ferrous and Copper Ions. *Environ. Sci. Technol.* **38**, 6676-6684.

Moraghan, J. T. and Buresh, R. J., 1977. Chemical Reduction of Nitrite and Nitrous Oxide by Ferrous Iron. *Soil Science Society of America, Journal* **41**, 47-50.

Naegele, J. R., Cox, L. E., and Ward, J. W., 1987. Photoelectron spectroscopy (UPS/XPS) study of Np_2O_3 formation on the surface of neptunium metal. *Inorganica Chimica Acta* **139**, 327-329.

Nakayama, S. and Sakamoto, Y., 1991. Sorption of neptunium on naturally occurring iron-containing minerals. *Radiochimica Acta* **52/53**, 153-157.

O'Loughlin, E. J., Kelly, S. D., Cook, R. E., Csencsits, R., and Kemner, K. M., 2003. Reduction of Uranium(VI) by Mixed Iron(II)/Iron(III) Hydroxide (Green Rust): Formation of UO_2 Nanoparticles. *Environmental Science & Technology* **37**, 721-727.

Pepper, S. E., Bunker, D. J., Bryan, N. D., Livens, F. R., Charnock, J. M., Pattrick, R. A. D., and Collison, D., 2003. Treatment of radioactive wastes: An X-ray absorption spectroscopy study of the reaction of technetium with green rust. *Journal of Colloid and Interface Science* **268**, 408-412.

Refait, P., Abdelmoula, M., and Génin, J.-M. R., 1998a. Mechanisms of formation and structure of green rust one in aqueous corrosion of iron in the presence of chloride ions. *Corrosion Science* **40**, 1547-1560.

Refait, P., Charton, A., and Génin, J.-M. R., 1998b. Identification, composition, thermodynamic and structural properties of a pyroaurite-like

iron(II)-iron(III) hydroxy-oxalate Green Rust. *European Journal of Solid State and Inorganic Chemistry* **35**, 655-666.

Roh, Y., Lee, S. Y., and Elless, M. P., 2000a. Characterization of corrosion products in the permeable reactive barriers. *Environmental Geology* **40**, 184-194.

Roh, Y., Lee, S. Y., Elless, M. P., and Foss, J. E., 2000b. Incorporation of radioactive contaminants into pyroaurite-like phases by electrochemical synthesis. *Clays and Clay Minerals* **48**, 266-271.

Seah, M. P., Gilmore, I. S., and Beamson, G., 1998. XPS: Binding Energy Calibration of Electron Spectrometers 5 – Re-evaluation of the Reference Energies. *Surf. Interface Anal.* **26**, 642-649.

Simard, S., Odziemkowski, M., Irish, D. E., Brossard, L., and Ménard, H., 2001. In situ micro-Raman spectroscopy to investigate pitting corrosion product of 1024 mild steel in phosphate and bicarbonate solutions containing chloride and sulfate ions. *Journal of Applied Electrochemistry* **31**, 913-920.

Skovbjerg, L. L., Christiansen, B. C., Dideriksen, K., and Stipp, S. L. S., Submitted. Reduction of tetravalent selenium by green rust sodium sulphate. *Environ. Sci. Technol.*

Skovbjerg, L. L., Stipp, S. L. S., Utsunomiya, S., and Ewing, R. C., 2006. The mechanisms of reduction of hexavalent chromium by green rust sodium sulphate: Formation of Cr-goethite. *Geochimica et Cosmochimica Acta* **70**, 3582-3592.

Stumpf, S., Stumpf, T., Dardenne, K., Hennig, C., Foerstendorf, H., Klenze, R., and Fanghänel, T., 2006. Sorption of Am(III) onto 6-Line-Ferrihydrite and Its Alteration Products: Investigations by EXAFS. *Environ. Sci. Technol.* **40**, 3522-3528.

Stumpf, T., Curtius, H., Walther, C., Dardenne, K., Ufer, K., and Fanghänel, T., 2007. Incorporation of Eu(III) into Hydrotalcite: A TRLFS and EXAFS Study. *Environ. Sci. Technol.* **41**, 3186-3191.

Teterin, Y. A. and Teterin, A. Y., 2004. The structure of X-ray photoelectron spectra of light actinide compounds. *Russ. Chem. Rev.* **73**, 541-580.

Thierry, D., Persson, D., Leygraf, C., Delichere, D., Joiret, S., Pallotta, C., and Goff, A. H.-L., 1988. In-Situ Raman Spectroscopy Combined with X-Ray Photoelectron Spectroscopy and Nuclear Microanalysis for Studies of Anodic Corrosion Film Formation on Fe-Cr Single Crystals. *Journal of The Electrochemical Society* **135**, 305-310.

Tochiyama, O., Endo, S., and Inoue, Y., 1995. Sorption of neptunium(V) on various iron oxides and hydrous iron oxides. *Radiochimica Acta* **68**, 105-111.

Veal, B. W., Lam, D. J., Diamond, H., and Hoekstra, H. R., 1977. X-ray photoelectron-spectroscopy study of oxides of the transuranium elements Np, Pu, Am, Cm, Bk, and Cf. *Physical Review B* **15**, 2929.

Warren, G. P. and Alloway, B. J., 2003. Reduction of Arsenic Uptake by Lettuce with Ferrous Sulfate Applied to Contaminated Soil. *J Environ Qual* **32**, 767-772.

Appendix 5

Reduction of tetravalent selenium by green rust sodium sulphate

L. L. Skovbjerg*, B. C. Christiansen, K. Dideriksen, S. L.S. Stipp

To be submitted to Geochimica et Cosmochimca Acta

Reduction of tetravalent selenium by green rust sodium sulphate

L. L. Skovbjerg*, B. C. Christiansen, K. Dideriksen, S. L.S. Stipp

Nano-Science Center, Department of Chemistry, University of Copenhagen, Denmark;

LoneS@nano.ku.dk; bochr@nano.ku.dk; knud@nano.ku.dk; stipp@nano.ku.dk

to be submitted to *Geochimica et Cosmochimca Acta*

Abstract
Green rust is an Fe(II),Fe(III)-bearing compound in the layered double hydroxide (LDH) family. The high surface area of its colloidal particles and its redox potential make it an interesting and reactive compound for water treatment and reactive barriers. This work investigated the ability of green rust sodium sulphate ($GR_{Na,SO4}$) to reduce selenite (SeO_3^{2-}) which is problematic when concentrations in the environment are high. The chemical processes resulting in reduction have been defined using results from potentiometry, X-ray diffraction (XRD), atomic force microscopy (AFM) and transmission electron microscopy (TEM). The green rust surface is initially saturated with selenite, which is reduced while some of the green rust is oxidised. After a lag phase, the remaining selenite is removed from solution as more green rust is dissolved and reprecipitated as goethite (α-FeOOH). Selenite is reduced to nanoparticles of elemental grey selenium, which has low solubility. There is no indication that selenite replaces sulphate in the green rust interlayer, as has been observed for other compounds.

1. INTRODUCTION

Selenium is of interest because of its role in human health (review by (BARCELOUX, 1999)). One can suffer from too little as well as too much. While deficiency is easily cured with diet supplements, high-level exposure results in poisoning. For this reason, the behaviour of selenium and its mobility from soils with high concentrations to water supplies must be understood for predictive transport modelling to be reliable. Furthermore, selenium is of concern for nuclear waste management because of the presence of the long-lived radioactive fission product, Se-79, in spent nuclear fuel. Several countries plan to build underground storage facilities for medium- and high-level radioactive waste where safety relies on maintaining a reducing environment. Although these repositories will be constructed to last for 10^5 or 10^6 years, worst-case scenarios must be considered for nuclear waste repository failure.

The mobility and bioavailability of Se is governed by its oxidation state (BARCELOUX, 1999). The oxidised, inorganic oxyanions, Se(VI) and Se(IV), are the species associated with groundwater (BARCELOUX, 1999) because they are much more soluble than Se(0) and Se(-II) under normal soil conditions. The higher solubility of the oxidised species means a higher degree of transport and bioavailability. Thus, reduction is an effective way of limiting selenium transport.

Green rust (GR) is a redox active compound that contains both ferrous and ferric iron and belongs to the family of layered double hydroxides. It consists of brucite-like sheets of Fe(II)-Fe(III) hydroxide (BERNAL et al., 1959). To compensate for the excess positive charge contributed by Fe(III), the structure is interlayered by anions, such as carbonate, sulphate or chloride, and in some cases, cations such as sodium (CHRISTIANSEN et al., Submitted-a). The compound $NaFe^{II}_6Fe^{III}_3(OH)_{18}(SO_4)_2{\cdot}nH_2O$, includes a relatively large amount of structural water. GR has been documented to occur naturally in reduced soils (TROLARD et al., 1997) and in the iron redox boundary of chalk and granitic groundwater reservoirs (CHRISTIANSEN et al., Submitted-b). It can also form directly from corrosion of metallic iron (e.g. (PHILLIPS et al., 2003; REFAIT et al., 2003; STAMPFL, 1969). Because iron and steel are present in many engineered systems such as reactive iron barriers for groundwater remediation and as reinforced concrete in radioactive waste repositories, dissolved ferrous iron concentrations and pH are high enough that the formation

* corresponding author:
Email address: LoneS@nano.ku.dk

of GR is likely to influence redox processes taking place in these environments.

Myneni et al. (1997) were the first to show that green rust (GR) can reduce hexavalent selenium, Se(VI), to the metallic form, Se(0), and possibly to selenide, Se(-II). Since then, more studies have examined the interaction of GR with hexavalent Se (JOHNSON and BULLEN, 2003; REFAIT et al., 2000). However, detailed information about the interaction between GR and tetravalent Se is lacking. In many groundwater systems and radioactive waste repositories, conditions are reducing, meaning that Se(IV) is thermodynamically more stable than Se(VI) (SEBY et al., 1998).

The purpose of this study was to define the geochemical processes that control the fate of Se(IV) during and after its reaction with green rust sodium sulphate. With this aim, laboratory experiments with Se(IV) and GR were carried out and the transforming solids and aqueous species were characterised using atomic force microscopy (AFM), transmission electron microscopy (TEM), X-ray diffraction (XRD) and classical wet chemistry techniques.

2. MATERIALS AND METHODS

2.1 Synthesis of $GR_{Na,SO4}$

Except for a few adjustments, this work used the same experimental procedure as Skovbjerg et al. (2006). Synthesis of GR, as well as experiments and sample preparation, were performed in an anaerobic glove box with $O_{2(g)}$ concentration less than 0.5 ppm. We used the sodium sulphate form of green rust ($GR_{Na,SO4}$) so the results of this investigation can be compared directly with the study of chromate interaction with the same material (SKOVBJERG et al., 2006). $GR_{Na,SO4}$ structure has been described by (CHRISTIANSEN et al., Submitted-a); it has a basal spacing of 11 Å, yielding an interlayer distance of about 9 Å, where SO_4^{2-}, H_2O and Na^+ are ordered.

The GR was synthesised using the constant pH method described in Koch and Hansen (1997) but the method was modified to fit the conditions in our laboratory. Briefly, a deoxygenated solution was prepared with 200 mL of a 0.05 M $FeSO_4 \cdot 7H_2O$ (purity > 99.5% from AppliChem). Ambient air was purged of $CO_{2(g)}$ by bubbling it through a 20% NaOH solution. To induce precipitation of green rust, the air was bubbled through the Fe(II) solution. To keep pH constant at 7.0 (+/- 0.15), 1 M NaOH (standard titration solution from Merck) was added using a pH stat (Radiometer). The reaction was halted before all Fe(II) was consumed in order to keep GR stable (LEWIS, 1997). We used Savillex PFA (perfluoroalkoxy polymer) beakers for both synthesis and experiments, rather than glassware to decrease the amount of dissolved Si, which has been shown to have significant effect on GR reactivity (HENDRIKSEN and HANSEN, 2003; KWON et al., 2007). PFA also minimises adsorption of ferrous iron and selenite to the reaction vessel surfaces. Before use, the PFA beakers were treated with 20% HCl and then 1% HNO_3 to remove iron oxides from previous experiments. All water used was deionised (MilliQ, conductivity < 0.1 µS/cm) and prior to GR synthesis it was de-oxygenated by bubbling with 99.9990% $N_{2(g)}$.

2.2 Reaction between selenite and $GR_{Na,SO4}$

Selenite reaction experiments were carried out with specific Se:GR ratios. To calculate the quantity of Se to be added, the amount of GR in solution was initially determined based on the concentration of Fe^{2+} in solution after synthesis (about 2-3 mM; (SKOVBJERG et al., 2006)). During synthesis of the sodium sulphate form of GR, the Fe(II):Fe(III) ratio is constant at 2:1 (BERNAL et al., 1959; HANSEN et al., 1994; SIMON et al., 2003) and using the following equation, the moles of Fe(II) in GR ($Fe(II)_{GR_{Na,SO4}}$) can be calculated:

$$Fe(II)_{GR_{Na,SO4}} = \frac{4}{6}(Fe^{2+}{}_{initial} - Fe^{2+}{}_{end}) \quad (1)$$

$Fe^{2+}{}_{initial}$ represents the molar concentration of added $FeSO_4 \cdot 7H_2O$, $Fe^{2+}{}_{end}$, the molar concentration of Fe^{2+} measured in solution after synthesis and the ratio 4/6, the Fe(II)/(Fe(II)+Fe(III)) ratio of sulphate GR. Knowing the amount of $Fe(II)_{GRNa,SO4}$ present, the selenium salt could be added in amounts that would oxidise a predefined portion of the Fe(II) in the GR. Based on preliminary studies, Se(IV) was assumed to be reduced to Se(0). When calculating the amount of Se salt required, the following stoichiometry was used:

$$4Fe(II)_{(GR_{Na,SO4})} + SeO_3^{2-} + 6H^+ = 4Fe^{3+} + Se(0) + 3H_2O \quad (2)$$

We accounted for the amount of Fe^{2+} present in solution that is reduced with the stoichiometry of Eq. 2. The dissolved Fe^{2+} concentration varied slightly between experiments.

In order to react 35% or 75% of the Fe(II) bound in the GR as well as all the aqueous Fe^{2+}, we added 2 mL of a 0.32 M or 0.6 M Na_2SeO_3 solution (pH ~ 10) to 200 mL of GR suspension where the total Fe(II) present in both cases was 34 mmoles. During the reaction, pH was measured continuously with a combination electrode and Eh was monitored using an Ag/Ag^+ platinum electrode. Although Eh is a mixed potential resulting from both Fe and Se, Eh monitoring served as an indicator of relative activity changes in solution.

Samples were withdrawn periodically to examine the evolution in aqueous concentration as well as the structure and morphology of the solids. In some experiments, samples were taken every two hours for 24 hours while in other experiments, the sampling interval was shorter. All samples were centrifuged to separate solids for XRD analysis and supernatant for chemical analysis. Total Fe, Se and Na were determined using a Perkin Elmer 5100 atomic absorption spectrometer (AAS). The uncertainty for Fe and Se determinations is about 10%. Because of the high concentrations of Na, the samples were diluted by a factor of 500 to 2000. The uncertainty is estimated to about 15%. Na data were not intended to be used for stoichiometry; we wanted only to see relative increasing or decreasing trends. All dissolved Fe is assumed to be Fe^{2+} because of its much higher solubility than Fe^{3+}. It was not possible to distinguish between the selenium species, but because we added soluble Se(IV) in a reducing

environment and Se(0) and Se(-II) have very low solubility, we assume that all dissolved Se in solution remains as Se(IV).

Compound identity in the solid fraction was determined using X-ray diffractometry (XRD) performed on a Bruker AXS four-circle diffractometer (molybdenum source with λ = 1.5418 Å, energy = 40 kV and a graphite filter). The consolidated and dried solid from the centrifuge tubes was crushed in an agate mortar in the glove box and the powder was sealed in capillary tubes to prevent oxidation during analysis.

Particle morphology and changes with time were observed with atomic force microscopy (AFM). We used a Digital Instruments Multimode IIIa. The entire microscope was fitted inside the anaerobic chamber so air exposure was avoided during imaging. All images were obtained in contact mode using standard Si_3N_4 tips. Samples were prepared by leaving a droplet of the suspension on a piece of freshly cleaved muscovite for about 30 seconds. Hereafter it was flushed with deionised water to remove salts and loose material. The remaining liquid was sucked away with the corner of a tissue.

TEM was performed about three months after selenite had been added to the GR suspension. The samples were prepared by depositing a droplet of suspension on a copper grid with holey carbon mesh for about 5 s and then flushing it with deionised water to avoid salt precipitation and too thick layers of particles. Standard TEM imaging was performed on a Philips CM 20. High resolution TEM (HR-TEM), as well as elemental analyses using energy dispersive X-ray spectroscopy (EDS), were obtained using a JEOL 3000F.

3. RESULTS AND DISCUSSION

3.1 Reaction

During reaction, pH and Eh were monitored, providing an indicator for the reaction stages. Figure 1 shows the evolution of a system where enough selenium was added to potentially oxidise all the Fe^{2+} in solution as well as about 75% of the Fe(II) in the GR. Four significantly different stages can be recognised.

3.1.1 Stage 1

An initial sharp increase of pH from 8 to nearly 9 follows the introduction of the selenite solution. Within the first half hour, pH drops in parallel with decreased concentration of aqueous selenium, iron and sodium. The initial pH increase is a response to the higher pH of the selenite solution (pH ~10) and probably the formation of $Fe(OH)_{2(s)}$ and its subsequent oxidation by selenite to GR. For the sake of simplicity, we write the formula for GR without water:

$$36Fe(OH)_2 + 3SeO_3^{2-} + 8SO_4^{2-} + 4Na^+ + 4n{\cdot}H_2O =$$
$$4NaFe^{II}{}_6Fe^{III}{}_3(OH)_{18}(SO_4)_2{\cdot}nH_2O + 3Se_{(s)} + 18OH^- \quad (3)$$

The decrease in both Na and Fe concentration supports the formation of green rust and a similar reaction was observed by Refait et al. (2000) when selenate was reacted with $Fe(OH_2)_{(s)}$.

The significant pH decrease which is observed shortly thereafter corresponds to a dramatic loss of $Fe^{2+}{}_{(aq)}$ by the first sampling point and a ferric phase, namely goethite, α-FeOOH, is detected with XRD. This suggests the following reaction:

$$SeO_3^{2-} + 4Fe^{2+} + 5H_2O = 4FeOOH + Se_{(s)} + 6H^+ . \quad (4)$$

The decrease in selenite is much larger than can be accounted for by the lost iron. A likely explanation is selenite adsorption on GR or goethite particles, as was reported by Su and Suarez (2000).

3.1.2 Stage 2

The Eh and pH measurements show that the second stage begins about 15 minutes after selenite addition to the suspension and lasts almost six hours. During this time, pH is stable for several hours, indicating that the reactions dominating do not release protons or hydroxyls to solution. The Se concentration from about 0.5 hours to 3-4 hours is almost stable and the situation resembles a lag phase. Eh decreases, however, indicating a change in oxidation state in the solution. Because the concentration of dissolved Fe^{2+} remains very low throughout this stage, the oxidation state of selenium is interpreted to dominate the Eh

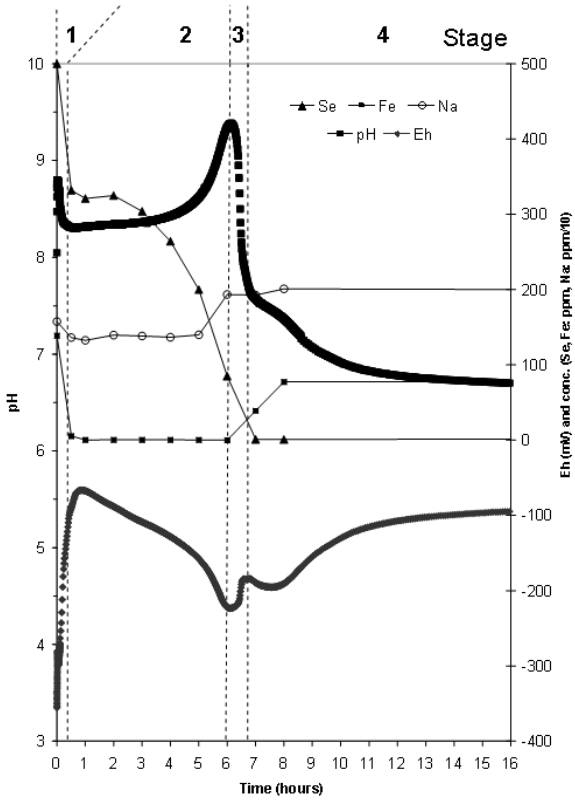

Figure 1. Eh and pH measurements and evolution of dissolved concentrations of Se, Fe and Na in solution from an experiment where selenite could oxidise 75% of the Fe(II) in the GR to elemental selenium. The reaction can be described by four major stages (separated by dashed vertical lines). GR is present in the system only in stages 1 and 2. After 8 hours, the concentration of Fe, Se and Na in solution remained constant. The final sampling at 53 hours (not shown) gave the same results as at 8 hours.

evolution of the system and we should expect to observe a reduced selenium phase. After an hour, the suspension develops a distinct metallic luster. Selenium in its native form, Se(0), does exhibit metallic luster. XRD patterns show a very weak, broad peak in the range where the main selenium peak is expected. Broadening can indicate very small particles, poor crystallinity or both. Also, when the supernatant from the centrifuged samples was not filtered prior to determination with AAS, a grey film covered the liquid surface and analysis yielded a high concentration of Se compared to the data presented in Figure 1. We interpret the grey film to be hydrophobic particles of elemental selenium that were too small to settle during centrifugation and that were atomised together with aqueous Se in the AAS flame. The presence of amorphous Se(0) was also reported by Myneni et al. (1997) when hexavalent selenium was reacted with GR.

After about 5 hours, a peak representing crystalline, metallic selenium was visible at 3 Å spacing on XRD patterns, indicating recrystallisation of the initially amorphous selenium. Toward the end of the second stage, pH rose at an increasing rate while Eh and dissolved Se, determined from filtered samples, decreased progressively faster. After 6 hours of reaction, at the end of stage 2, GR could no longer be detected. This is consistent with GR breakdown, which provides Fe^{2+} for selenite reduction, releasing both OH^- and Na^+ to solution. Thus, during stage 2, selenite initially adsorbed on GR and present in solution is reduced to elemental selenium while GR is oxidised to goethite:

$$2NaFe^{II}_6Fe^{III}_3(OH)_{18}(SO_4)_2{\cdot}nH_2O + 3SeO_3^{2-} = 18FeOOH + 3Se_{(s)} + 4SO_4^{2-} + 9{+}nH_2O + 2Na^+ \quad (5)$$

A puzzling observation, however, is that dissolved Fe^{2+} remains below detection limit. It only increases after the point where XRD indicates complete breakdown of GR. Most likely, Fe(II) adsorbs as surface complexes on selenite and on goethite (≡FeO-Fe^{2+}). Dixit and Hering (2006) among others have studied Fe(II) interaction with goethite and found a high degree of adsorption at pH 7 and above.

3.1.3 Stage 3

During the third stage, which lasts close to an hour, pH decreases abruptly and Eh increases. Dissolved Se concentration decreases to 1 ppm while the Fe^{2+} concentration increases. At this point, GR is no longer visible by XRD and the continued selenite reduction most likely results from reaction with Fe^{2+} adsorbed on the surface (≡) of the goethite nanoparticles (Figure 3). Such a reaction produces protons, explaining the rapid pH decrease:

$$4 \equiv FeO\text{-}Fe^{2+} + SeO_3^{2-} + 5H_2O = 4 \equiv FeOH + 4FeOOH + Se_{(s)} + 2H^+ \quad (6)$$

Alternatively, Fe^{2+} may stem from an XRD amorphous solid, which can reduce selenite. We note however, that such a solid would have to contain less hydroxide than GR to produce the observed pH decrease.

3.1.4 Stage 4

As pH decreases, some Fe^{2+} is released to solution, most likely as a result of competition between H^+ and Fe^{2+} for adsorption sites on the fine-grained goethite or as a result of continued dissolution of an amorphous ferrous phase. However, only about 20% of the total Fe^{2+} of the suspension is released, so much remains associated with a solid phase. After about 12 hours, pH and Eh are almost constant at about pH = 6.7 and Eh = -100 mV. The final set of measurements at 53 hours shows that dissolved concentrations remain constant, indicating that the system has reached equilibrium.

3.2 End products

The end products of the reaction were goethite and elemental, crystalline selenium (Figure 2 and Figure 3a). Three types of elemental selenium exist: red, black and gray. The gray is the most stable at ambient conditions (OLIN et al., 2005) and is the phase observed in our experiments. Grey Se(0) crystallises in the trigonal system and is easily recognised with XRD by its highest intensity peak at d = 3.00 Å (JCPDS-06-0362). The particles are nanometer-sized but have a high degree of crystallinity as observed both with XRD (Figure 2) and TEM (Figure 3b).

Our findings correspond well with those in the literature. Myneni et al. (1997) reacted the sulphate form of GR with selenate. Extended X-ray absorption fine structure (EXAFS) and X-ray absorption near edge structure (XANES) indicated production of amorphous Se(0) that formed clusters on the surface of the ferric end products, which, dependent on pH, were magnetite and/or lepidocrocite. Scheidegger et al. (2003), who studied the interaction between iron(0) and selenite, also used EXAFS to elucidate the speciation of the reduced selenium. The results pointed toward the presence of elemental selenium but there was no indication from EXAFS/XANES about crystallinity of the final phase. Bruggeman et al. (2005) reacted selenite with pyrite (FeS_2) and confirmed selenite

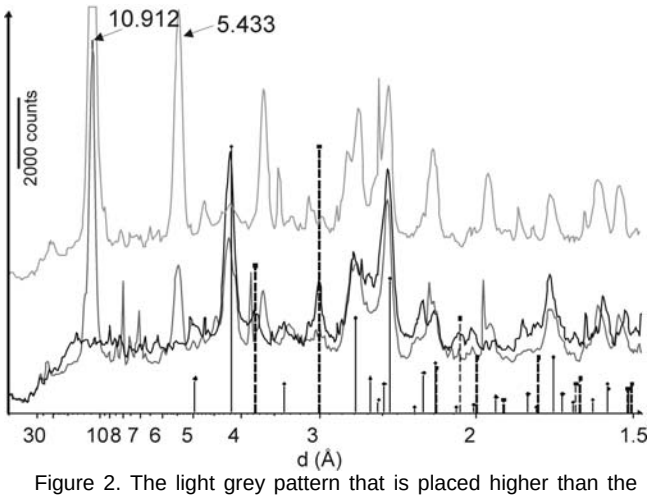

Figure 2. The light grey pattern that is placed higher than the other two traces comes from pure $GR_{Na,SO4}$ before reaction with selenite. The dark grey line is from a sample analysed 5 hours after the exposure to selenite solutions and is the last sample that still shows GR. The black trace shows the end products, goethite (solid vertical bars) and elemental gray selenium (dashed bars).

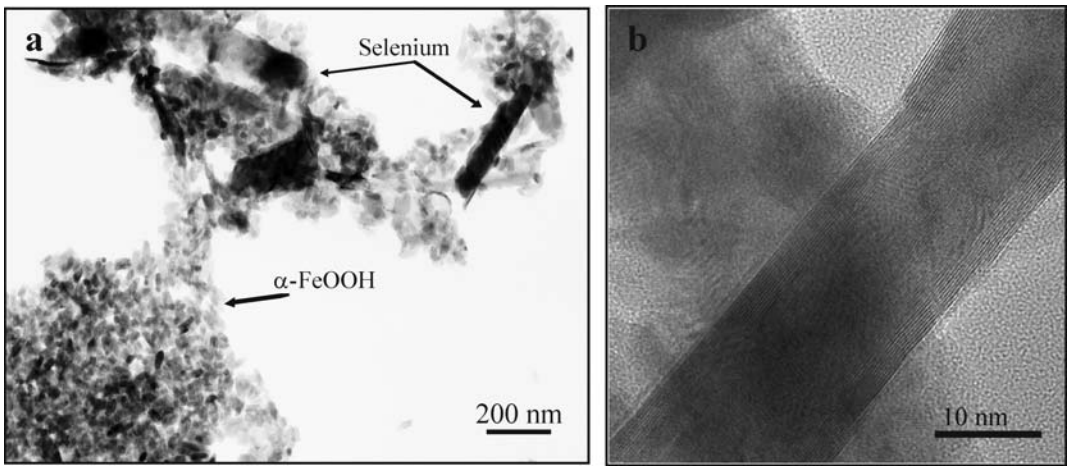

Figure 3. TEM images from suspensions that had aged for about 3 months in their equilibrium solution after addition of selenite. (a) Nanoparticles of goethite and selenium are stable but crystals are still extremely small. (b) HR-TEM of the selenium particles shows a well-ordered atomic lattice.

reduction to Se(0) with XRD. They did not state whether the end phase was amorphous or crystalline. Other studies of selenate interaction with green rust (JOHNSON and BULLEN, 2003; REFAIT et al., 2000) were focused primarily on the first stage of reduction from selenate to selenite.

In one of our experiments, where only 40% of the Fe(II) in GR could be oxidised by the added Se, pH and Eh ended in the stability field where selenide, Se(-II) is expected. However, even after three months, no selenide phase could be observed. Using EXAFS and XANES, Myneni et al. (1997) detected only trace amounts of Se(-II) after reduction of hexavalent selenium by green rust. Thus, it appears that the transformation from Se(0) to Se(-II) is kinetically hindered.

The ferric end product, goethite, formed even smaller particles than the metallic selenium. The particles express the usual elongated form expected of goethite (Figure 3a) but their average crystal length is only about 50 nm. Formation from a pure system produces crystals about 10 times larger, suggesting that the presence of Se hinders growth, promoting formation of abundant crystal nuclei. Goethite was detected with XRD already after about 30 minutes of reaction (data not shown) and the intensity of the peaks continued to increase with time. With AFM, it was possible to follow the transformation of the GR particles and in contrast to previously published results on chromate interaction with GR (SKOVBJERG et al., 2006), there were no indication that selenite interaction induces topotactic transformation of GR to goethite. Rather, the data indicate that the transformation from GR to goethite is mainly a dissolution-reprecipitation reaction. The transformation mechanism is important because it controls the behaviour of other contaminants. If green rust had incorporated other trace components, topotactic transformation would retain them in the new phase. In contrast, dissolution would release them and the capacity for subsequent uptake by the new phase would be controlled by the stability relationships of the contaminant and the solid.

3.3 Mechanism of reduction

The mechanism of Se reduction was investigated further with AFM. Detailed imaging from an experiment where 35% of the Fe(II) in GR could be oxidised by the added selenite showed the transformation of the solid phases. The pH/Eh measurements for the initial stages (not shown) were very similar to Figure 1; the first two stages could easily be recognised so we could relate samples with processes taking place at the time and compare between experiments. Samples examined with AFM showed precipitation of tiny particles at the edges of the green rust crystals during the second stage (Based on XRD and solution parameters, these are most likely amorphous selenium. The material is reminiscent of the amorphous clusters described by Myneni et al. (1997). The distribution of these particles suggests that the reaction takes place mostly at the edges of the green rust crystals. In some cases, the particles form an outline where a green rust layer is likely to have dissolved. Probably selenite adsorbs preferentially at the interlayer edges, which have saltwater-like properties (i.e. structural H_2O, Na^+ and SO_4^{2-}), thus functioning as a conductive layer for the transfer of electrons from Fe(II). Reduced selenium is insoluble, so it precipitates very close to the site where reduction occurred. Green rust becomes unstable when Fe(III) proportion increases, so it dissolves locally, where it is oxidised. Samples taken later in the second stage shows these precipitates to be more evenly distributed over the crystal. There are two possibilities. Either electrons are also transported across the interlayers directly to selenite adsorbed on the GR surface or the selenium must be transported from an edge, through solution and deposited at a site some distance away.

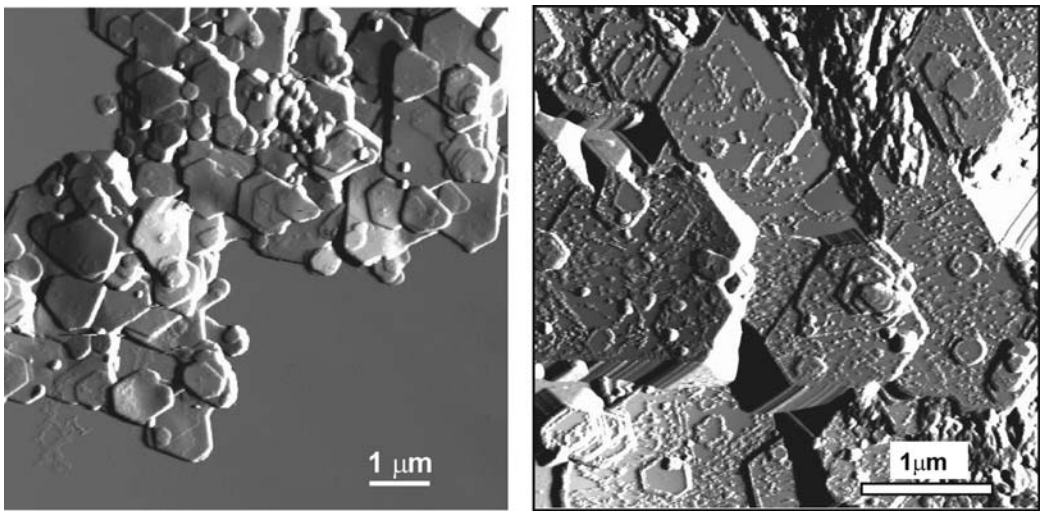

Figure 4. AFM images (deflection mode) of pure, fresh $GR_{Na,SO4}$ (left) and $GR_{Na,SO4}$ after reaction with selenite for 2 hours (right). Before reaction, $GR_{Na,SO4}$ has flat surfaces with some terraces that are one or a few molecular layers thick. During reaction, these terraces disappear but precipitates are left at the edges where the terraces were, as well as on the edges of the whole crystals. Edges apparently have high reactivity.

There are no indications of Se incorporation into the green rust structure. If selenite was incorporated, it would most probably enter the interlayers from the edges and replace SO_4. In such a case, we would expect to see some change in morphology in the edge area but this is not the case for selenite (SeO_3^{2-}) interaction. Some preliminary experiments with hexavalent selenium (SeO_4^{2-}) on the other hand, strongly indicated initial incorporation of this species into the interlayer of $GR_{Na,SO4}$. This parallels the changes in morphology observed in a previous study on green rust interaction with chromate (CrO_4^{2-}) which demonstrated that interlayer replacement induces topotactic transformation of green rust to Cr(III)-substituted goethite (SKOVBJERG et al., 2006). CrO_4^{2-} and SeO_4^{2-} are different from SeO_3^{2-} in both size and form. Chromate and selenate ions are tetrahedral, resembling the green rust interlayer anion sulphate, SO_4^{2-}. Selenite is smaller and lacks one oxygen, so its coordination is unlikely to fit the interlayer sites.

However, the reduced end products of the selenium oxyanions do not depend on the reduction mechanism. For both selenite and selenate, which react by two different reaction processes, nano-particles of low solubility elemental selenium are produced. The mobility of these in groundwater would depend on their affinity for adhering to the phases present in the porous medium.

4. ACKNOWLEDGEMENTS

We thank Vagn Moser for AAS measurements, Erik Johnson for TEM assistance and expertise, Tonci Balic-Zunic and Helene Almind for XRD expertise and Hans Christian Bruun Hansen for inspiring our work on green rust. Funding was provided by FunMig, an EC Framework 6 Integrated Project, Svensk Kärnbränslehantering (SKB) and the Danish Natural Research Council (FNU).

5. REFERENCES

Barceloux, D. G., 1999. Selenium. *Journal of Toxicology-Clinical Toxicology* **37**, 145-172.

Bernal, J. D., Dasgupta, D. R., and Mackay, A. L., 1959. The oxides and hydroxides of iron and their structural inter-relationships. *Clay mineral bulletin* **4**, 15-30.

Bruggeman, C., Maes, A., Vancluysen, J., and Vandenmussele, P., 2005. Selenite reduction in Boom clay: Effect of FeS2, clay minerals and dissolved organic matter. *Environmental Pollution* **137**, 209-221.

Christiansen, B. C., Balic-Zunic, T., Petit, P.-O., Frandsen, C., Mørup, S., Geckeis, H., Katerinopoulou, A., and Stipp, S. L. S., Submitted-a. Composition and structure of an iron-bearing, layered double hydroxide (LDH) – Green rust sodium sulphate. *Geochimica et Cosmochimica Acta*.

Christiansen, B. C., Balic-Zunic, T., and Stipp, S. L. S., Submitted-b. Natural occurrences of green rust. *Environ. Sci. Technol.*

Dixit, S. and Hering, J. G., 2006. Sorption of Fe(II) and As(III) on goethite in single- and dual-sorbate systems. *Chemical Geology* **228**, 6-15.

Hansen, H. C. B., Borggaard, O. K., and Sørensen, J., 1994. Evaluation of the free energy of formation of Fe(II)-Fe(III) hydroxide-sulphate (green rust) and its reduction of nitrite. *Geochimica et Cosmochimica Acta* **58**, 2599-2608.

Hendriksen, P. T. and Hansen, H. C. B., 2003. The effect of orthosilicate on the reactivity of iron(II)iron(III)hydroxide chloride (green rust)*Internat. workshop Biogeochemical processes involving iron minerals in natural waters*, Monte Verita, Switzerland.

Johnson, T. M. and Bullen, T. D., 2003. Selenium isotope fractionation during reduction by Fe(II)-Fe(III) hydroxide-sulfate (green rust). *Geochimica et Cosmochimica Acta* **67**, 413-419.

Koch, C. B. and Hansen, H. C. B., 1997. Reduction of Nitrate to Ammonium by Sulphated Green Rust. *Advances in GeoEcology* **30**, 373-393.

Kwon, S.-K., Kimijima, K., Kanie, K., Suzuki, S., Muramatsu, A., Saito, M., Shinoda, K., and

Waseda, Y., 2007. Influence of silicate ions on the formation of goethite from green rust in aqueous solution. *Corrosion Science* **49**, 2946-2961.

Lewis, D. G., 1997. Factors Influencing the Stability and Properties of Green Rusts. In: Auerswald, K., Stanjek, H., and Bigham, J. M. Eds.), *Advances in GeoEcology*. Catena Verlag, Reiskirchen, Germany.

Myneni, S. C. B., Tokunaga, T. K., and Brown Jr., G. E., 1997. Abiotic selenium redox transformations in the presence of Fe(II,III) oxides. *Science* **278**, 1106-1109.

Olin, Å., Noläng, B., Osadchii, E. G., Öhman, L.-O., and Rosén, E., 2005. *Chemical thermodynamics of selenium* Elsevier, Amsterdam, London.

Phillips, D. H., Watson, D. B., Roh, Y., and Gu, B., 2003. Mineralogical characteristics and transformations during long-term operation of a zerovalent iron reactive barrier. *Journal of Environmental Quality* **32**, 2033-2045.

Refait, P., Memet, J. B., Bon, C., Sabot, R., and Genin, J. M. R., 2003. Formation of the Fe(II)-Fe(III) hydroxysulphate green rust during marine corrosion of steel. *Corrosion Science* **45**, 833-845.

Refait, P., Simon, L., and Génin, J.-M. R., 2000. Reduction of SeO_4^{2-} Anions and Anoxic Formation of Iron(II)-Iron(III) Hydroxy-Selenate Green Rust. *Environmental Science and Technology* **34**, 819-825.

Scheidegger, A. M., Grolimund, D., Cui, D., Devoy, J., Spahiu, K., Wersin, P., Bonhoure, I., and Janousch, M., 2003. Reduction of selenite on iron surfaces: A micro-spectroscopic study. *Journal De Physique Iv* **104**, 417-420.

Seby, F., Potin-Gautier, M., Giffaut, E., and Donard, O. F. X., 1998. Assessing the speciation and the biogeochemical processes affecting the mobility of selenium from a geological repository of radioactive wastes to the biosphere. *Analusis* **26**, 193-198.

Simon, L., François, M., Refait, P., Renaudin, G., Lelaurain, M., and Génin, J.-M. R., 2003. Structure of the Fe(II-III) layered double hydroxysulphate green rust two from Rietveld analysis. *Solid State Sciences* **5**, 327-334.

Skovbjerg, L. L., Stipp, S. L. S., Utsunomiya, S., and Ewing, R. C., 2006. The mechanisms of reduction of hexavalent chromium by green rust sodium sulphate: Formation of Cr-goethite. *Geochimica et Cosmochimica Acta* **70**, 3582-3592.

Stampfl, P. P., 1969. Ein Basisches Eisen-II-III-Karbonat in Rost. *Corrosion Science* **9**, 185-187.

Su, C. M. and Suarez, D. L., 2000. Selenate and selenite sorption on iron oxides: An infrared and electrophoretic study. *Soil Science Society of America Journal* **64**, 101-111.

Trolard, F., Génin, J.-M. R., Abdelmoula, M., Bourrié, G., Humbert, B., and Herbillon, A., 1997. Identification of a green rust mineral in a reductomorphic soil by Mössbauer and Raman spectroscopies. *Geochimica et Cosmochimica Acta* **61**, 1107-1111.